UNIVERSIDADE ESTADUAL DE CAMPINAS
INSTITUTO DE FÍSICA “GLEB WATAGHIN”

LEONARDO OPARACZ KUTELAK

HIGH PRESSURES MAGNETISM OF EuB$_6$ PROBED WITH X-RAY SPECTROSCOPY TECHNIQUES

MAGNETISMO DO EuB$_6$ SOB ALTAS PRESSÕES SONDADO POR ESPECTROSCOPIA DE RAIOS-X

Campinas

2020

LEONARDO OPARACZ KUTELAK

HIGH PRESSURES MAGNETISM OF EuB_6 PROBED WITH X-RAY SPECTROSCOPY TECHNIQUES

MAGNETISMO DO EuB_6 SOB ALTAS PRESSÕES SONDADO POR ESPECTROSCOPIA DE RAIOS-X

Dissertation presented to the Institute of Physics Gleb Wataghin of the University of Campinas in partial fulfillment of the requirements for the degree of Master in Physics, in the area of Applied Physics.

Dissertação apresentada ao Instituto de Física Gleb Wataghin da Universidade Estadual de Campinas como parte dos requisitos exigidos para a obtenção do título de Mestre em Física, na Área de Física Aplicada.

Supervisor/Orientador: Dr. Ricardo Donizeth dos Reis

Co-supervisor/Coorientador: Prof. Dr. Flávio César Guimarães Gandra

ESTE EXEMPLAR CORRESPONDE À VERSÃO FINAL DA DISSERTAÇÃO DEFENDIDA PELO ALUNO LEONARDO OPARACZ KUTELAK, ORIENTADO PELO PROF. DR. RICARDO DONIZETH DOS REIS.

Campinas

2020

Ficha catalográfica
Universidade Estadual de Campinas
Biblioteca do Instituto de Física Gleb Wataghin
Lucimeire de Oliveira Silva da Rocha - CRB 8/9174

K969h
Kutelak, Leonardo Oparacz, 1994-
High pressure magnetism of EuB6 probed with X-ray spectroscopy techniques / Leonardo Oparacz Kutelak. – Campinas, SP : [s.n.], 2020.

Orientador: Ricardo Donizeth dos Reis.
Coorientador: Flávio César Guimarães Gandra.
Dissertação (mestrado) – Universidade Estadual de Campinas, Instituto de Física Gleb Wataghin.

1. Magnetismo. 2. Luz síncrotron. 3. Experimentos de altas pressões. I. Reis, Ricardo Donizeth dos, 1987-. II. Gandra, Flávio César Guimarães, 1954-. III. Universidade Estadual de Campinas. Instituto de Física Gleb Wataghin. IV. Título.

Informações para Biblioteca Digital

Título em outro idioma: Magnetismo do EuB6 sob altas pressões sondado por espectroscopia de raios-X
Palavras-chave em inglês:
Magnetism
Synchrotron light
High pressure experiments
Área de concentração: Física Aplicada
Titulação: Mestre em Física
Banca examinadora:
Ricardo Donizeth dos Reis [Orientador]
Eduardo Matzenbacher Bittar
Abner de Siervo
Data de defesa: 02-10-2020
Programa de Pós-Graduação: Física

Identificação e informações acadêmicas do(a) aluno(a)
- ORCID do autor: https://orcid.org/0000-0002-2539-6684
- Currículo Lattes do autor: http://lattes.cnpq.br/5356140172679121

MEMBROS DA COMISSÃO JULGADORA DA DISSERTAÇÃO DE MESTRADO DE **LEONARDO OPARACZ KUTELAK – RA 228217** APRESENTADA E APROVADA AO INSTITUTO DE FÍSICA "GLEB WATAGHIN", DA UNIVERSIDADE ESTADUAL DE CAMPINAS, EM 02 / 10 / 2020.

COMISSÃO JULGADORA:

- Prof. Dr. Ricardo Donizeth dos Reis – Orientador – CNPEM
- Prof. Dr. Eduardo Matzenbacher Bittar – CBPF
- Prof. Dr. Abner de Siervo – DFA/IFGW/UNICAMP

OBS.: Ata da defesa com as respectivas assinaturas dos membros encontra-se no SIGA/Sistema de Fluxo de Dissertação/Tese e na Secretaria do Programa da Unidade.

CAMPINAS
2020

Agradecimentos

Gostaria de agradecer todos aqueles que me apoiaram durante a jornada academica desde o inicio da graduação até o presente momento. Em especial agradeço meu orientador Ricardo Donizeth dos Reis por me propiciar oportunidades de valor inestimavel, meu corientador Flavio Guimarães Gandra por seus preciosos conselhos e Michael Nicklas pelo acolhimento propiciado no instituto Max Planck. Agradeço ao grupo EMA e o laboratório de Altas Pressões do SIRIUS-LNLS por todo suporte experimental disponibilzado. Agradeço imensamente a imprescindivel ajuda de Eduardo Poldi, Gustavo Lombardi e Marcos Eleoterio fornecida nos experimentos desse trabalho, assim como Mário Piva pela ajuda especial no periodo no exterior. Extendo agradecimentos para Jairo Fonseca pela sua paciencia em me auxiliar no laboratorio, Lucas Francisco pelo apoio computacional, teórico e discussões valiosas. Aos integrantes do grupo EMA, Alvaro, Bárbara, Danusa, Judá, Kelin, Ulisses e Rodrigo pela participação ativa para meu amadurecimento academico. Destaco que, sem as ideias ambiciosas e estrutura laboratorial instaurada por Narcizo Marques de Souza Neto esse trabalho não seria possível.

Aproveito para agradecer o fundamental apoio de Priscila Rosa ao fornecer as amostras para esse trabalho, também Gilberto Fabbris e Daniel Haskel pelo apoio na linha 4-ID-D do APS nos experimentos de XAS, Ercan Esen Alp e Jiyong Zhao pelo apoio nos experimentos de Mössbauer na linha 3-ID-D.

Por fim gradeço aos meus amigos Alan, Bruna, Leonardo Marcon, Marina e Rafael que não só me ajudaram com suas conversas e ideias mas também tornaram esse periodo de mestrado em algo muito especial que será lembrado com muito carinho para o resto de minha vida.

O presente trabalho foi realizado com apoio da Coordenação de Aperfeiçoamento de Pessoal de Nível Superior Brasil (CAPES) - Código de Financiamento 001. Também agradeço o apoio financeiro das agencias de fomento CNPq (135947/2018-9) e FAPESP, a partir do projeto 2018/19015-1 e do projeto JP 2018/00823-0.

Resumo

A familia dos hexaboretos de terras raras apresenta uma rica variedade em fenômenos de transporte, indo de supercondutores a isolantes de Kondo. Recentemente compostos como SmB_6 e YbB_6 foram revisitados a partir de propostas de topologia não trivial correlacionados a estados de valencia mista em seus diagramas de fase. Isso abre perspectivas de estados exóticos em demais compostos da família, principalmente ao utilizar parametros de ajuste como pressão hidrostatica, explorando possiveis conexões entre esses compostos contendo ions com eletrons bem localizados na camada 4f.

Nesse trabalho exploramos o EuB_6, único da familia que apresenta ferromagnetismo bem definido em pressões de até cerca de 17 GPa. Além disso o composto apresenta duas transições envolvendo formação de polarons magnéticos e deslocalização de portadores de cargas, com discussões em aberto sobre seu caráter semimetálico ou semicondutor. Nesse trabalho observamos, através de técnicas de espectroscopia de absorção de raios x (XAS) e Mössbauer de síncrotron (SMS), que ao aplicar pressões jamais atingidas para esse hexaboreto: acima de 20 GPa utilizando células de bigorna de diamante (DACs), o ordenemento ferromagnético abaixo de 12 K é suprimido e substituido por uma nova fase paramagnetica com coexistencia de ions Eu^{2+} e Eu^{3+}.

Isso abre prospectos para estudos teóricos e experimentais sobre a física por tras dessa nova fase observada em ambientes de condições extremas. Com isso, correlacões entre a estrutura dos hexaboretos de terras raras, suas propriedades magnéticas e eletrônicas podem ser entendidas com mais profundidade, abrindo novas possibilidades para potencialmente encontrar e elucidar estados com topologia não trivial propostos para essa família.

Palavras-chave: Magnetismo, Altas Pressões, Luz Síncrotron.

Abstract

Rare earth hexaboride family present a rich variety of transport phenomena, ranging from superconductors up to Kondo insulators. Recently compounds such as SmB_6 and YbB_6 were revisited from proposals of non-trivial topology correlated to mixed-valence state in its phase diagram. This opens perspectives for exotic states on remaining family's compounds, mainly when using adjustment parameters like hydrostatic pressure, exploring possible connections between these well localized 4f shell electron containing ions.

In this work we explore EuB_6, the only compound of the family that presents well defined ferromagnetic ordering up to pressures of 17 GPa. Furthermore it also presents two transitions involving magnetic polarons formation and charge de-localization, with open discussion about it semimetallic or semiconductor behavior. At this work we observe, using X-Ray absorption spectroscopy (XAS) and synchrotron Mössbauer spectroscopy, that by applying pressures above 20 GPa using diamond anvil cells (DACs) the ferromagnetic ordering below 12 K is suppressed and substituted by a new paramagnetic phase where Eu^{2+} and Eu^{3+} coexist.

This opens prospects for theoretical and experimental studies about physics behind the new phase observed in ambient of extreme conditions. With this, correlations between rare earth hexaborides structure, magnetic and electronic properties may be better understood with the opening of new possibilities to find and elucidate proposed non-trivial topology states for this family.

Keywords: Magnetism, high pressure, synchrotron radiation.

Contents

Chapter 1

Introduction

Electronic and magnetic properties of materials are subject of interest for its application in technology and fundamental scientific knowledge. In this category, rare earth metals, specially from element in the Lanthanum series, have an unique electronic configuration with well localized 4f shell protected by external 5d and 6s electrons, which gives rise to local momentum magnetic properties, that are extensively explored in high-tech industry. Therefore, understanding their fundamental behaviors in different compounds and conditions are not only of scientific interest but also of strategic and commercial relevance. Taking this into consideration rare earth hexaborides (REH) are subject of study for many decades and thanks to their simple cubic structure they pose as an excellent candidate for simplified models and analysis. In the other hand, this family hosts several interesting and not completely understood transport properties, which most recently are being revisited within the scope of topologically non-trivial materials.

A notoriously famous rare earth hexaboride, SmB_6 is known by its low temperature resistivity plateau and other puzzling properties [1] [2]. A similar compound, YbB_6 hosts interesting transport phenomena as well, and suchlike SmB_6 it may be correlated to a mixed valence state between 2+ and 3+ ions. Another vastly used REH is LaB_6 which, because its low work function [3] allows efficient use in electron microscopes and it is also a common X-ray diffraction pattern due to its aforementioned cubic structure. CeB_6 on it's turn, presents a dense Kondo lattice of localized momenta with characteristic resistivity behaviour [4] and potential for topologically non-trivial changes under applied pressure [5]. Many of this family's compounds order in a anti-ferromagnetic manner at low temperature regimes (below 30 K) such as NdB_6 [6], GdB_6 and DyB_6 [7] [8], while other such as ErB_6 and HoB_6 are too unstable or difficult to prepare [9]. Finally, EuB_6 is the only REH reported to order in a ferromagnetic manner by hosting Eu^{2+} ions, and will be the compound of study for this work.

EuB_6 is studied as early as 1950's and since then has struck researchers with non-usual magnetic and transport phenomena. It was observed that doping this REH with carbon substituting boron not only decreases significantly the Curie temperature from its initial value of around 13 K but also provides an anti-ferromagnetic behavior for 15% Carbon concentration [10]. It was also observed that low impurity containing crystals have two subsequent transitions, one at ≈15 K and other at ≈13 K which are linked to magnetic behavior, being claimed to be magnetic ordering at one crystallographic direction at T_{c1} and reordered to other at T_{c2} [11]. Although, a more likely picture as proposed by Matthias as early as 1968 [12] is the formation of magnetic polarons involving charge carriers. These entities are magnetic puddles, occurring above T_c in a paramagnetic background and robust visual evidence in EuB_6 samples were recently obtained via magneto optical [13] and STM experiments [14]. In the other hand, ARPES experiments [15] [16] and early claims based on transport measurements suggest that there is a semiconductor gap at the X symmetry point [17] [18] of the Brillouin zone, but there are also claims for semi-metallic behavior [19], where the gap is closed with conduction and valence band overlapping. More recently it was proposed that for certain magnetization directions there is the possibility for topologically non-trivial structures to arise where valence and conduction band touch [20].

As briefly mentioned above doping changes EuB_6 magnetic properties, similarly high pressures achieve such effect, as showed by Cooley et al.[21] in their resistivity measurements where both T_c increases in temperature. They also suggest that underlying magnetic mechanism between 4f momenta occurs via indirect Ruderman-Kittel-Kasuya-Yosida (RKKY) interaction where conduction electrons spins intermediate exchange which has an oscillatory nature. Moreover, this provides additional support that adjust parameters, such as external pressure and doping, can create connections between this families members by modifying magnetic behavior when changing atomic distances and/or electronic density. In another light this might provide a probable path for Kondo lattice behavior, where local magnetic momenta where local magnetic moments interfere in transport properties via their spin interaction with charge carriers. As explained by Doniach in his famous diagram [22], RKKY magnetic interaction and Kondo behavior may compete in system with well localized magnetic momenta, although this is most commonly associated to (the unlikely for our case) heavy Fermi behavior. This competition is driven by the magnetic ordering temperature T$_M$ (or energy, and can be either FM or AFM) and the Kondo temperature T$_K$, both of which are dependent on the exchange parameter between localized momenta and carriers spin J . In a simplified manner it can be said that when T$_M$ $>$ T$_K$ we have magnetic order and when T$_M$ $<$ T$_K$ there is Kondo behavior. Furthermore in the case of T$_M$ $=$ T$_K$ it is proposed that a quantum critical point (QCP) may occur [22] at 0 K generating interesting exotic physical behavior at temperatures near absolute zero, which might include non trivial topology.

Topology may be refereed as a mathematics branch interested in describing geometrical properties of materials that remain constant while they go through continuously smooth deformation [23]. In the context of physical properties we are interested in certain band structures that remain constant when some symmetries are conserved [24] [25], namely topological structures protected by a symmetry. For example, topological insulators (TIs) have a non-trivial structures called Dirac-cones which are protected by time reversal symmetry, occurring when two bands of opposite parity (+ and -) cross each other near Fermi's surface [26]. This lead to interestingly robust transport phenomena such as materials with insulator bulks and conducting surfaces [27] where spin-locked current are protected against scattering. Furthermore, there exist other topologically non-trivial structures such as Weyl points, which are usually related to semi-metallic behavior and can be protected by mirror symmetry, inversion symmetry, spin-rotation, time reversal among others [28]. Touching between valence and conduction bands when spin-orbit coupling is strong and non-trivial topological states are present can lead to the so called Weyl fermions (WF), which in the context of condensed matter form Weyl points, (Weyl fermions concentration in 2D momentum space) working as sources or sinks for Berry curvature, which is a geometrical parameter that provides information about topological entanglement of valence and conduction bands [29]. Additionally, in between two Weyl points there will exist structures known as Fermi arcs connecting them, which has a non-zero Berry phase due to chirality flip in the WP pair, giving rise to a Chern number equal to unity, which is a important Topological invariant, whereas if the Chern number is equal to zero the topology is deemed trivial. Experimentally Fermi arcs may be resolved using techniques such as angle resolved photo emission spectroscopy (ARPES) but energy resolution is the technique's bottleneck in many cases. Regardless, transport phenomena such as, large or negative magneto resistance together with anomalous or quantized hall effect and high carrier mobility were observed in Weyl semimetals such as TaP [30] and NbP [31] and may be related to their topology. Lastly, it is important to remark that Weyl aemi metals and their cousin Dirac semi metals (which are WSM with broken time reversal symmetry) are transitioning states in between topological insulators and normal insulators as noted by Yan and Felser [29].

Regarding EuB_6, theoretical work supports formation of different topological structures depending on the magnetic field direction in the crystal. When the field is aligned with [100] crystallographic direction, nodal lines appear near high symmetry points of the Brillouin zone. Such structures are similar to Weyl Points, but now touching between valence and conduction bands occur in a closed curve inside the BZ. When field direction is changed to [111], claimed as the easy axis below 12.5 K, nodal lines turn into 3 Weyl point pairs, one at each Z point. Furthermore, when magnetic field is aligned with the [110] direction there is a coexistence between one nodal line and two pairs of Weyl points. This happens because each field direction generates different protecting symmetries for the topological structures, meaning that when one symmetry breaks another one replaces it. Finally, calculations also support that due to these exotic topological behaviors anomalous and quantized Hall effect may occur in the EuB$_6$. A more detailed discussion regarding these predicted topological states in EuB$_6$ can be found in [20].

To further investigate if states that permit such structures to arise in EuB$_6$ and have a better grasp of eventual connection between REH physical properties we propose experiments combining an external adjust parameter with X-ray spectroscopy techniques, aiming to observe phenomena potentiality correlated to exotic behavior, such as electronic and magnetic phase transitions. In our case we choose hydrostatic pressure applied with diamond anvil cells (DACs), which can alter lattice parameter in a clean manner allowing for a study in REH, without adding analytical complexity due to eventual changes in electronic configuration or band structure when substituting ions or atoms. Furthermore, these cells match perfectly with synchrotron X-ray sources by providing a direct optical path into the sample space. Employing well established X-ray absorption near edge (XANES) technique concomitantly with X-ray circular magnetic dichroism we are able to simultaneously probe valence, electronic and magnetic EuB$_6$ properties under high pressures and at low temperature < 15 K, well inside the know ferromagnetic ordering regime reported for ambient pressures. Although few limitations are encountered in this techniques the most critical one is that we are only able to probe net sample magnetization, making antiferromagnetic and paramagnetic states unresolved. For this reason we also employ synchrotron Mössbauer spectroscopy (SMS), allowing to probe nuclear states in the same pressure and temperature range to complement information about the compound's magnetic state obtained through XANES and XMCD. Finally, our SMS measurement agrees with our XAS results, indicating a new phase above 20 GPa and below 13 K, that from our preliminary analysis seems to present paramagnetic nature with mixed valence state.

In regard to text structure, this dissertation will provide a scientific background in the second chapter, reviewing physical concepts relevant to the work while presenting previous results for EuB_6 found in the literature. This will include information on crystal growth and structure, followed by magnetic interactions and relevant phenomena reported for our compound. The Chapter 3 is devoted for theory in X-ray spectroscopy techniques (XAS and SMS), which compose the bulk experimental work performed during the project. Chapter 4 describes experimental methods utilized in this work, including a section in high pressure experiments with some theoretical background for manometer techniques and historical development. Finally, in Chapter 5 we present the obtained results accompanied by some discussion with Chapter 6 hosting our concluding remarks.

Chapter 2

Scientific Background

This chapter is devoted for basic scientific background related to EuB_6 physics. The intention is to provide the theory behind each physical concept and proceed to discuss the specifics for EuB_6. In this way the reader is guided through the text in a manner that the general context for what is well established in the literature paves way to better understand the intricacies of our system. Some subjects and equations are more developed due to direct links to our work, while others are discussed more briefly to maintain context. The ultimate goal for the text is to provide a general guide in many experimental and theoretical concepts relevant to the work for eventual newcomers without being boring to expert readers.

2.1 Crystal growth and structure

In this section we review EuB_6 (and other hexaborides) crystal growth methods and structure, putting emphasis in aluminum flux grown samples since it was the synthesis technique utilized for crystals provided by Dr. Priscilla Rosa from Los Alamos Laboratory as a collaboration for this work.

Rare earth hexaborides have sensible transport properties dependent on their growth conditions where Al-flux is the best procedure to obtain high quality single crystalline samples, and there exists an intense debate on literature about the effects of sample grow techniques on some physical transport, as is thoroughly discussed in the work of Phelan *et al.* [32]. As aforementioned, samples for this work were grown using Al flux method, which despite possible Aluminum inclusions, crystals created through this technique seem to preserve main transport properties for this family of compounds.

Flux crystal growth usually occur as follows: adequate proportion of elements for the desired compound are inserted together with a solvent in a crucible made of a chemically inert material in relation to the growth reaction. Most commonly, the mixture is inserted inside a quartz ampule sealed in vacuum. The recipient is then taken to furnace and temperature is risen gradually in a way that the solvent flux melts first, followed by the melting of material's elements at higher temperatures. After adequate time, mixture temperature is lowered to a value where growth crystals are solidified while flux is still in liquid form, this way it is possible to employ a centrifugal motion to separate formed single crystal from the flux. Although this is the desired way to get crystals easily, this is not always possible, so flux may be etched chemically or samples may be mechanically separated once the mixture is at room temperature. This method is advantageous because it has potential to produce low impurity crystals in relatively simple manner, at a cost of generally producing small single crystal with possible flux inclusion or non-desired phases in it. More details on flux growth can be found in [33].

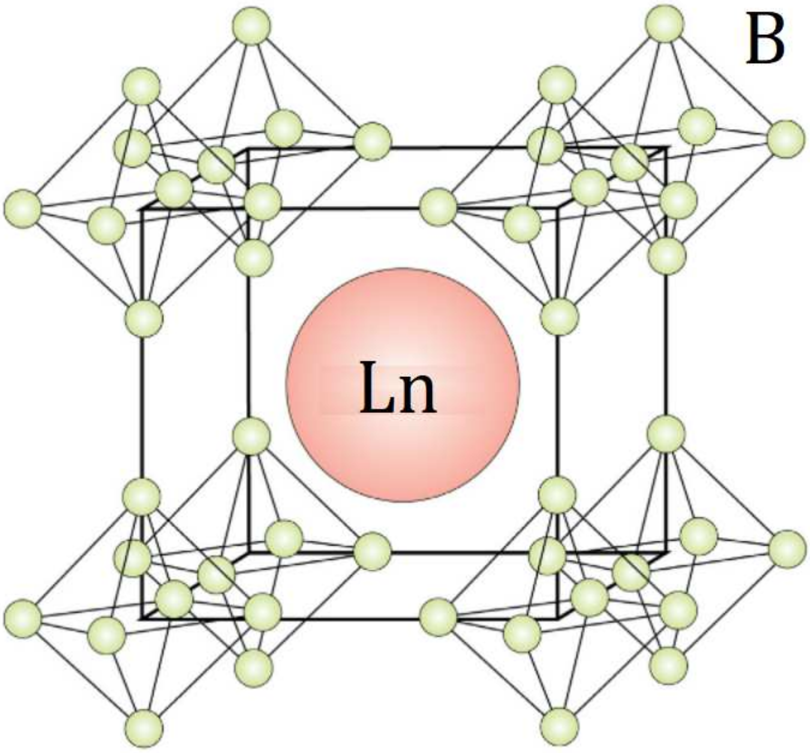

Figure 2.1: *Structure of a rare earth hexaboride (LnB*$_6$*) crystal. We see a cubic structure of boron octahedra enclosing an Ln ion. Figure adapted from [34]*

Rare earth hexaborides structure is quite simple, exhibiting a cubic arrangement of boron Lanthanum series (Ln) atoms with a cage of boron formed octahedron enclosing it, as can be seen in Figure 2.1. This family of crystals belong to the space group 221, Pm3m, with lattice parameters varying around $a \approx 4.1$

Å to a $\approx$ 4.2 Å. Further experiments suggests that such structure is sturdy, with CeB_6 crystals supporting up to 122 GPa of applied pressure without going through a structural phase transition [5], suggesting that observed changes in the material are entirely due to electronic properties. In the specific case for EuB_6 a detailed X-ray diffraction study [11] report a lattice parameter of $a = 4.185$ Å with no visible structural transition down to 8 K, with many reported values in the literature near this parameter.

2.2 Magnetic Interactions in Solids

In this section we explore the basics for magnetic interactions and link it to the context of rare earth hexaborides focusing on the exotic EuB_6 features. Among REH compounds many order in a antiferromagnetic manner with EuB_6 being the only one with ferromagnetic ordering where early reports [35] measured a Curie Temperature at 13.7 K. Later many studies reported two subsequent phase transitions at $\approx$ 15 K and other at $\approx$ 13. One of these studies claimed this phases transitions where a ferromagnetic ordering followed by magnetic moment re-orientation in another crystallographic direction [11], while others claimed it was actually a material metallization mediated by entities called magnetic polarons followed by the proper ferromagnetic transition [18]. To better grasp these concepts and understand this historical development throughout four decades we backtrack to basic magnetism concepts, coming back to EuB_6 when convenient along the way.

Magnetism is a quantum mechanical phenomena in its essence, but early theoretical and experimental developments started under the light of classical concepts. Many famous scientists such as Oersted, Ampère, Biot, Savart worked on the links between electrical currents and generated magnetic fields, being able to describe them on the macroscopic scale with great success, leading a path that culminated into the renowned Maxwell's equations [36]. In the other hand, microscopical origins for observed phenomena could only be better understood with discoveries regarding charge quantization, electronic orbitals and particles intrinsic spin moments. It is now well established that a material's magnetic moments have their origins in the sum of particles quantized angular momenta and intrinsic spin magnetic moment as:

$$\langle m_{tot}^{z} \rangle = -\mu_o \frac{\mu_B}{\hbar} \left(g_s \langle s_z \rangle + g_l \langle l_z \rangle \right) \tag{2.1}$$

where $\langle m_{tot}^{z} \rangle$ is the expected magnetic moment in the (arbitrarily defined) z direction, $\langle s_z \rangle$ is the expected spin value and can assume values of $\pm\frac{\hbar}{2}$ for up and down spins, $\langle l_z \rangle$ the expected value for angular momentum and have quantized values of integer multiples of $\hbar$, μ_o the vacuum permeability, g_s is the spin's g-factor and is approximately 2 for electrons, g_l is the angular momentum g factor which we assume as 1, and finally

$$\mu_b = \frac{e\hbar}{2m_e} = 0.927 \times 10^{-23}\text{A m}^2 \tag{2.2}$$

is the Bohr magneton. It is important to mention that nucleons also have spin magnetic moments coming from half-spin particles even though they g-factor may vary depending on nuclear size, and their magnitude are 1836 times lower than electronic spin moment due to ratio between electron's and proton's masses [37].

For a better understanding on magnetic moments presented by electrons in atoms it is necessary to consider their atomic configuration. The total magnetic moment for a atom will arise from the sum of magnetic spin and angular moments of every electron occupying their orbitals. Completely filled electronic shells have zero angular and spin moment, therefore magnetism of an atom can be described by the configuration of their outermost unfilled shell. As an example, Lanthanum series ions will have heir magnetism dictated by the 4f shell configuration. These shells will be filled in a way to minimize ground state energy while respecting Pauli's exclusion principle and are explained by the empirical Hund's rules [38]. As general for rare earth elements, magnetism for europium can be well explained by treating them as isolated ions in the context of Curie's law for solids. Taking into account the total angular momentum operator

$$J = L + S \tag{2.3}$$

and the consequently derived Landé g-factor (assuming $g_s = 2$ and $g_l = 1$)

$$g(JLS) = \frac{3}{2} + \frac{1}{2}\left[\frac{S(S+1) - L(L+1)}{J(J+1)}\right] \tag{2.4}$$

it is possible to calculate the effective magnetic momentum per atom

$$\mu_{eff} = g(JLS)\,[J(J+1)]^{1/2}\,\mu_b \tag{2.5}$$

and allows us to write Curie's Law for magnetic susceptibility in the form:

$$\chi = \frac{1}{3}\frac{N}{V}\frac{\mu_{eff}^2}{k_B T} \tag{2.6}$$

where N is the number of momenta per molar volume V, this way it is possible to measure a material magnetic susceptibility and get experimental results for μ_{eff}. In our specific case we are interested in the electronic configuration for two Eu ions:

$$\mathrm{Eu}^{2+} = [\mathrm{Xe}]4\mathrm{f}^7 \quad , \quad \mathrm{Eu}^{3+} = [\mathrm{Xe}]4\mathrm{f}^6 \tag{2.7}$$

where [Xe] is the electronic configuration for the noble gas xenon, with fully filled shells. This way we obtain theoretical values for magnetic moments of 7.94μ_b for Eu^{2+} and zero for Eu^{3+}, telling us that magnetism in EuB$_6$ comes from the very localized 4f shells of doubly ionized europium atoms.

For materials with magnetic order there will be a temperature for which spontaneous alignment of magnetic moments will occur and prevail below it. Roughly speaking, if all spin align in a parallel manner below the Curie temperature T$_c$ (in this case) we say the material is ferromagnetic. In the other hand if spin align in a nonparallel way below the so called Neel temperature T$_N$ we have an antiferromagnet. In the context of solid state physics there are many theories to explain how aligned spins interact with each other, although this phenomena may not be well understood, specially in complex systems. To circumvent difficulties one popular tool usually used is the Mean Field Theory approximations, which basically assumes that individual electrons relevant to the system feel an averaged effect from all the other moments present in system. From this approximation it is possible to drawn that magnetic susceptibility in function of temperature follows the Curie-Weiss law, [38] given by

$$\chi = \frac{\chi_o}{T - T_c} \tag{2.8}$$

where $\chi_o = N\mu_{eff}^2/3Vk_B$ as in 2.6. This equation fails to describe susceptibility near T$_c$, but it is a good approximation for temperatures well above it. As an example, measurements made by Sullow et al [11] with a small (0.1 T) magnetic field applied separately along 3 different crystallographic directions of a EuB$_6$ single crystal have their results presented in Figure 2.2 where the $1/\chi$ curves were ploted for convenience. By linear fits in data at T >50 K they were able to obtain $\mu_{eff} \approx 8$, very close to the theoretical Eu^{2+} moment of $7.94\mu_{eff}$, in average and extrapolate a value of T$_C$ in between 14 K and 15 K. The value for effective magnetic moment is close to the theoretical one presented in the preceding paragraph, and T$_C$ has a close value for the first phase transition present in the material. Nevertheless as mentioned previously EuB$_6$ has two subsequent phase transitions related to its magnetism, therefore a complete picture for these behavior still need complements.

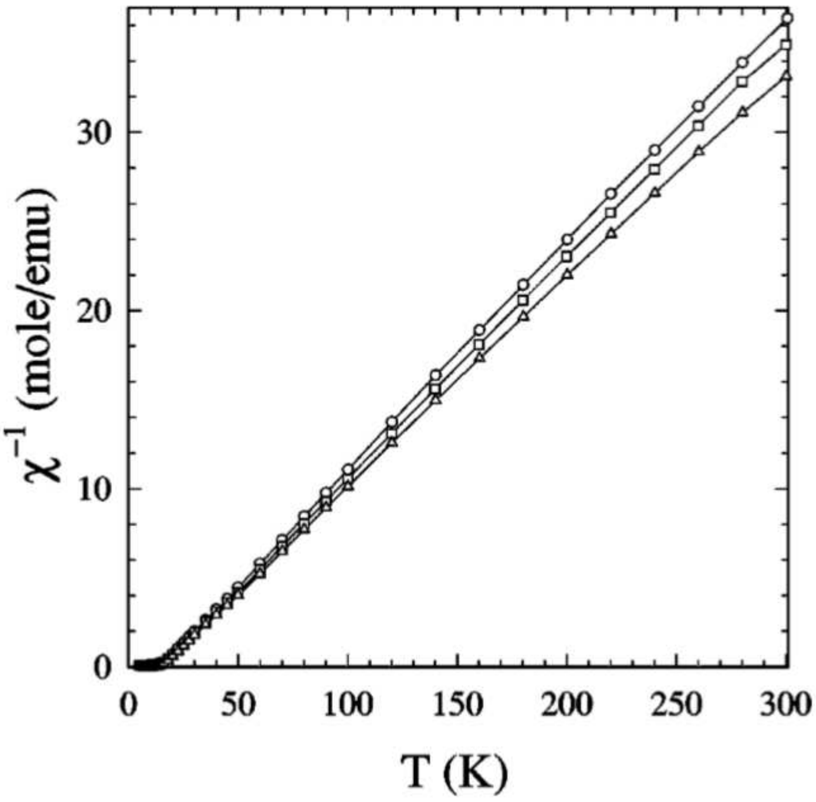

Figure 2.2: *Inverse of magnetic susceptibility in function of temperature for a single crystal of EuB$_6$. The circles represent measured points for B applied along [100] and yielded μ_{eff} = 7.9μ_B and T$_c$ = 14 K, squares are for [110] yielding μ_{eff} = 8.0μ_B and T$_c$ = 15 K, finally triangles are for [111] for which μ_{eff} = 8.2μ_B and T$_c$ = 14 K Figure reproduced from [11].*

Below T$_c$ a ferromagnetic material will present some features for magnetization in function of applied magnetic field which are useful for characterization. A typical curve for magnetization in function of applied field for a ferromagnetic material is shown in Figure 2.3. At first momentum will follow the blue line where moments will start to align along the direction of applied magnetic field until magnetization hits the saturation value S. After that magnetization follows the red line when applying a field in the opposite direction. Now magnetization will not return to 0 when field is back to zero, but there will be a remanent magnetization R, which only decays to zero after a field $H_c = C$ is applied, which is the coercetive field. Then after S' the same process occur for the field being applied in the 'positive' direction again, closing the called Hysteresis loop. The area inside a hysteresis loop is associated to the necessary energy to align moments in the direction of the applied magnetic field and roughly speaking it is possible to say that large areas are characteristic for a hard ferromagnet and small areas for a soft ferromagnet. In the case of EuB_6 it was previously measured [39] to be a very soft ferromagnet with non-discernible coercitivity and saturating at ≈ 1 T at a temperature of 4.3 K, with higher fields for higher temperatures.

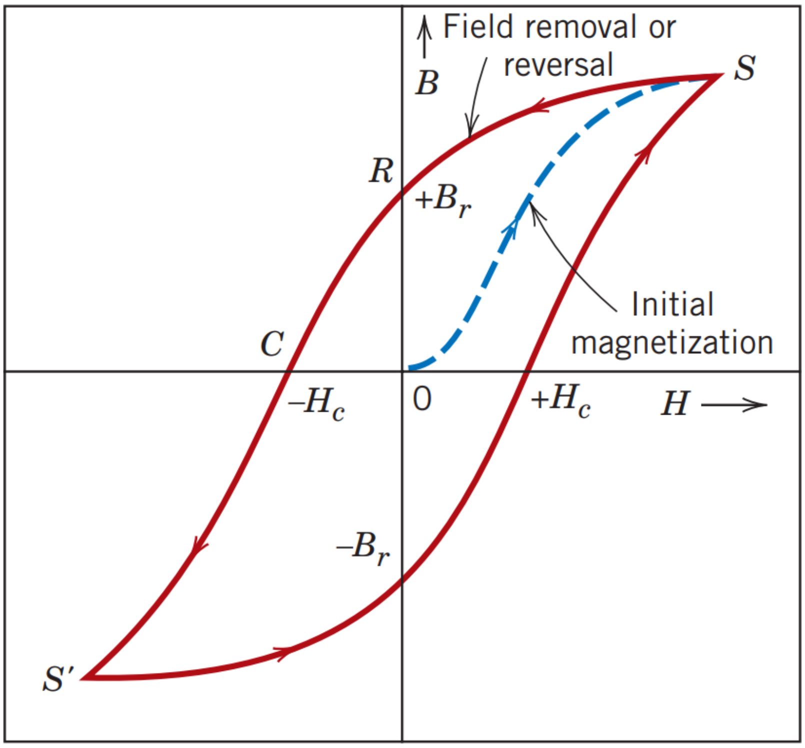

Figure 2.3: *Hysteresis loop for a typical ferromagnetic material where we can see the saturation, remanence and coercetivity as explained in the text. Figure reproduced from [40].*

2.2.1 Exchange Interactions

The next question we tackle is how these magnetic moments interact with each other in general and on the specific case of EuB_6. Within several approximations and simplifications one may use the Heisenberg Hamiltonian [38] to describe interactions between electron's spins:

$$H = -\sum J_{ij} S_i \cdot S_j \tag{2.9}$$

where S_i and S_j are the spin operators for the particles i and J in a system and J_{ij} is the exchange interaction between the electron pair, summation occur over all relevant pairs for the system. Even though S is called a spin operator it acts in the total magnetic moment that is arising from both angular and spin momenta. This Hamiltonian is vastly used to describe many complex systems in a simplistic manners, and may hold when there is a small overlap between charge distribution of the two electrons in the pair. When this is the case we have a direct exchange interaction, with J being dubbed as exchange parameter and will favor ferromagnetic (parallel spin $\uparrow\uparrow$) alignment when positive and antiferromagnetic (anti-parallel spin $\uparrow\downarrow$) alignment when negative. This parameter will often depend on subtle system details, but the low lying physics comes solely from Coulomb interactions and Pauli's exclusion principle for half-spin particles (Fermions) giving rise to singlet and triplet states.

Although direct exchange is conveniently used to describe many systems, electronic spins may also interact in a indirect manner. We attain our attention to a localized (4f shell, for example) magnetic momentum interacting via conduction electrons coupling. What happens is that this localized moment generates spin polarization waves along electrons in its surroundings with parallel or anti-parallel alignment as a function to the distance between spins. Ultimately this phenomena was explained by the combination of works from four scientists, and receives its name after them: Ruderman-Kittel-Kasuya-Yosida

(RKKY) interaction. Their work culminated in a expression that describes the oscillatory indirect interaction via a exchange parameter [37]:

$$J(R) = \frac{16A^2 m_e k_F^4}{(2\pi)^3 \hbar^2} \left[\frac{\cos(2k_F R)}{(2k_F R)^3} - \frac{\sin(2k_F R)}{(2k_F R)^4} \right] \tag{2.10}$$

where k_F is the Fermi wave vector A is a inter-atomic parameter and R is the distance between magnetic moments (spins). Again we have that when $J > 0$ or $J < 0$ there will be ferromagnetic or antiferromagnetic alignment, but now in a oscillatory manner depending on the inter-spin distance R and on electron configuration near valence bands as described by k_F. A EuB$_6$ transport study, under pressure, saw a systematically increase in the Curie temperature with applied pressure [21], which they argued to arise from a RKKY interaction enhanced by a greater electron density at pockets of electrons in a high symmetry point of the Brillouin zone near Fermi Level. Another experiment that suggest a RKKY behaviour was an early doping of EuB$_6$ with Carbon atoms substituting Boron, which decreases the lattice parameter, where anti-ferromagnetism was reported [10], nevertheless sample quality was different than today standards and doping can severely change electronic structure of a material. However, an interesting prospect is if clean isotropic lattice contraction by external force can create similar results. This opens prospects for new physics in EuB$_6$ if this case applies, as some theoretical works proposed Kondo behavior in this compound but with separated conduction and valence band exchange parameters [19].

2.2.2 Magnetic Polarons

Although this may be true, EuB_6 magnetic interaction and ordering modeled to arise from RKKY indirect exchange still does not gives a complete understanding for the system, since we still must take into account observations of magnetic polarons forming below temperatures near 40 K, which were experimentally suggested by results of two different techniques [13] [14] as showed and explained in Figure 2.4. These entities are regions (islands or puddles) of ferromagnetic regime embedded in a paramagnetic or antiferromagnetic background. Some conditions must be fulfilled for the creation of well defined magnetic polarons such as strong local magnetic exchange coupling and low carrier density in comparison to the magnetically correlated volume [41]. Furthermore, there are two kind of magnetic polarons: the free polaron which is a carrier aligning magnetic moments inside Bohr radius while moving through paramagnetic media and the bound polaron, which is a stationary entity generated around impurities due to Coulomb interactions. We attain our attention to the latter, since it was the one early observed in Eu containing compounds. The model proposed for a highly localized magnetic moment semiconductor (our case) provides that magnetic moment localization islands stabilizes around a impurity with differential free energy in relation to a paramagnetic background as [42]

$$\Delta F = \frac{E_0}{\iota} - \frac{J}{2\iota^3} - \frac{e^2}{\epsilon R} \tag{2.11}$$

where $E_0 = \pi^2 h^2/2ma^2$, $\iota = R/a$ with a coming from $4\pi a^3 = 1/N_{Eu}$, R is the distance from the impurity and N_{Eu} is the number of Eu^{2+} per unit volume. The bound polaron will not move easily with an applied electric field even below the eventual ordering temperature T$_c$, in the other hand a magnetic field will decrease disorder around the polaron, diminishing ΔF which can cause bound charges to move more easily. With decrease of temperature it is also possible that polarons start to grow larger and eventually coalesce with neighbor magnetic islands, generating a uniform ferromagnetic material. This picture suggests that transport properties will proportionate signature characteristics related to magnetic polarons such as negative magnetoresistance near ordering temperature. In fact, many experimental transport properties for EuB$_6$ were interpreted bye means of presence of magnetic polarons, and further discussion may be found in the following references, which also include theoretical works: [43] [44] [45][46][41][47][48]. In addition, applying pressure may alter Eu ion population, increasing Eu^{3+} while also diminishing number of defects in the structure, and since these are proposed to be ingredients for polaron formation in EuB$_6$ [18] this can further modify magnetic order and stimulate new phases in the material. Furthermore it may be feasible to try and obtain new phases via applied pressure by changing the exchange parameter J between magnetic momenta, possibly leading to exotic new states which might contain non-trivial topology.

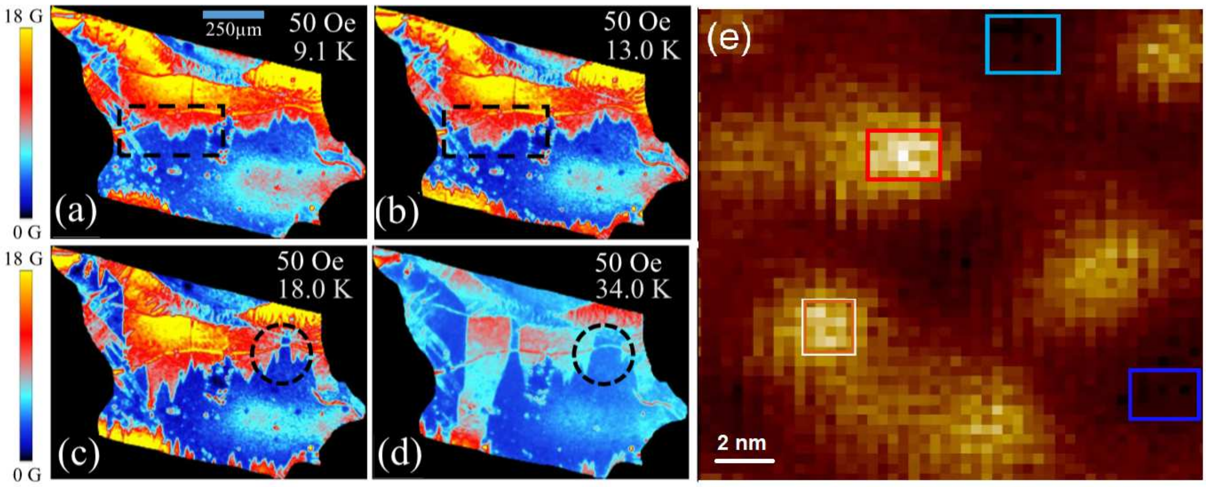

Figure 2.4: *Figures (a)-(d) show a* EuB_6 *single crystal analyzed by magneto-optical techniques [13], colors depict intern magnetic field intensities showing a slight magnetic domain growth from 9.1 K to 13 K and proceeding decrease in magnetic domains at 18 K to 34 K. Figure (e) shows an image of scanning tunneling spectroscopy for a* EuB_6 *single crystal at 20 K, with clear inhomogeneities in conduction evidenced by dark-bright contrast interpreted as regions of paramagnetic and ferromagnetic polarons respectively [14]. Details on both techniques can be found in their references. Figures adapted from [13] [14].*

Chapter 3

Synchrotron Spectroscopy Techniques

Synchrotrons are sophisticated machines in which electromagnetic radiation is created by accelerated particles stored in a closed planar orbit. This concept of particle accelerator was popularized by high energy physics experiments which focus is creation of new particles and better understanding near light speed collisions processes. Nevertheless, in nowadays physics there are several facilities which solely utilize synchrotron light coming from accelerated particles to perform experiments in several areas of knowledge. This light have potential for high photon flux with adjustable energy making them an excellent fit for spectroscopy experiments for samples encapsulated inside large devices, such as pressure cells. A more detailed explanation on synchrotron radiation is developed in Appendix I. Hence, high pressure XAS and Mössbauer Spectroscopy experiments are conveniently performed in Synchrotron facilities due to beamlines versatility. In this chapter we develop theoretical concepts on these techniques which were used to obtain the bulk experimental data for this work at the Advanced Photon Source (APS) in the Argonne National Laboratory.

3.1 XANES and XMCD

When light passes through matter it's intensity will decay exponentially following

$$I = I_o \mathrm{e}^{-\mu z} \tag{3.1}$$

where I_o and I are final and initial intensity, respectively, z is the sample length and μ is the absorption coefficient, which depends upon sample properties and is a function of the radiation energy: $\mu(E)$. Therefore, on a X-ray absorption experiment we can obtain $\mu(E)$ by measuring the light's intensity before and after it passes trough a sample, in the so called absorption geometry as depicted in Figure 3.1. For obtaining μz directly from measurements it suffices to perform $\ln(I_o/I)$. The light's absorption rate will decrease continuously as a function of energy in most spectral regions, but at certain energies there will be a sudden increase known as absorption edges. Such edges occur when the incoming photon's energy is equal to the (energy) gap between two orbitals where the absorbing electron can be encountered immediately before and after the absorption process, named initial and final states, respectively.

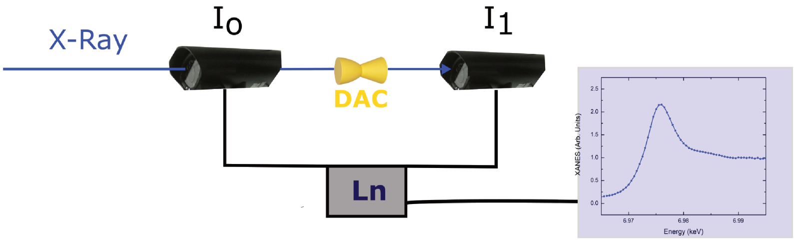

Figure 3.1: *Transmission geometry usually utilized in XANES experiments. The X-Ray intensity is measured before (I_o) and after (I_1) it passes trhough a sample. The signal from both detectors is them analyzed by performing ($ln(I_o/I_1)$) and gives us the absorption coefficient μ times the sample thickness x.*

The commonly used nomenclature for the edges follows the traditional spectroscopy notation. For instance, the K-edge is named after an absorption by the innermost electronic shell (quantum number $n = 1$). Subsequently the L-edge is the name given for absorption by the second innermost electronic shell ($n = 2$), M-edge stands for the third innermost shell ($n = 3$), and it continues alphabetically. But since for $n > 0$ we have $n + 1$ possible values for the quantum number l, (e.g $l = 0$ and $l = 1$ for $n = 1$, accompanied by the related values $m = -1, 0, 1$) the coupling between this orbital quantum numbers with the intrinsic electron's spin ($s = \frac{1}{2}, m = \pm\frac{1}{2}$) can provide us many possible total angular momentum $J = l + s$. For example the 2p ($n = 2$, $l = 1$) shell, has two possible values for J: $J = \frac{1}{2}$ and $J = \frac{3}{2}$. Therefore, we have 3 L-edges: L_I, L_{II} and L_{III}, corresponding to the 2s, 2p $J = \frac{1}{2}$ and $J = \frac{3}{2}$ absorption lines. Table 3.1 synthesizes this notation for the presented and few following cases.

n	l	Spectroscopy Notation	J	Edge Name
1	0	1s	1/2	K
2	0	2s	1/2	L_1
	1	2p	1/2	L_2
	1	2p	3/2	L_3
3	0	3s	1/2	M_3
	1	3p	1/2	M_2
	1	3p	3/2	M_3
	2	3d	3/2	M_4
	2	3d	5/2	M_5
4	0	4s	1/2	N_1
	1	4p	1/2	N_2
	1	4p	3/2	N_3
	2	4d	3/2	N_4
	2	4d	5/2	N_5
	3	4f	5/2	N_6
	3	4f	7/2	N_7

Table 3.1: *Table showing the relation between the principal and angular quantum numbers (n, l), spectroscopy notation for orbitals, coupled total Spin-Orbit momenta (J) and Absorption Edges names.*

It is important to notice that XANES is a element and orbital selective technique, since the initial state energy is dictated by electron-nuclei Coulomb interaction which is different for each atomic number Z. Furthermore, ionized atoms will have their absorption edges shifted by a few electron-volts, since with the loss of charge the energy necessary to promote a core electron increases slightly. Regardless of that, using XANES we can probe properties of a single element of interest inside a compound due to this initial state selectivity. On the other hand, the final state, which is related to the density of states near the Fermi energy, will be sensitive to the atoms‘ surroundings and chemical bounds. In practice this can change the absorption edge’s shape, what can be useful to obtain information on the compound's chemistry in some cases. Commonly the absorption edge shapes are those as depicted in Figure 3.2, which follow a Lorentzian shape with half height related to the core hole half-life, that due to Heisenberg's uncertainty principle creates a distribution in the absorption energy.

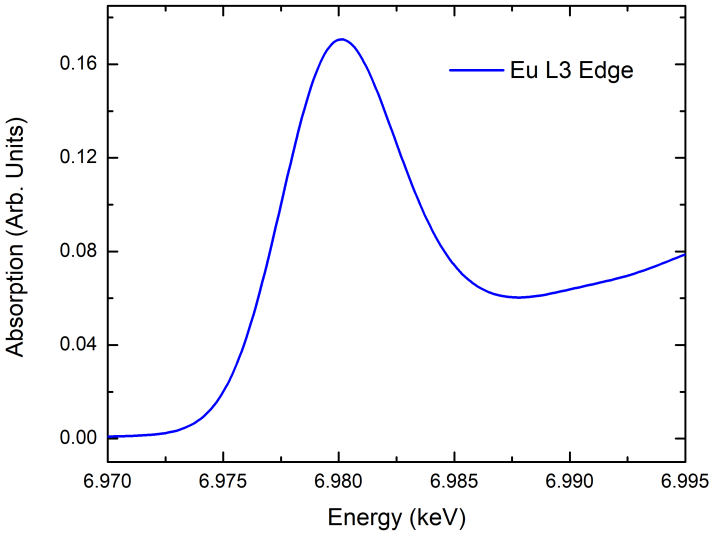

Figure 3.2: *Theoretical curves of absorption in function of photon Energy in the XANES region for an Eu atom. The curve's shape follow that of a Lorentzian with the core hole lifetime and final states energy broadness dictating its width.*

To better explain the absorption process in the quantum mechanical picture we use a few simplifications such as the *one electron approximation* where we neglect electron-electron interactions inside the atoms. We also use the *dipole approximation*, in which quadrupole interaction and above are neglected (acceptable for X-ray with less than 10 keV). Therefore, when a photon interacts with an atom, the probability per unit time T_{if} of an electron to go from one shell to another, is given by

$$T_{if} = \frac{2\pi}{\hbar} |\langle \Psi_f | H_{int} | \Psi_i \rangle|^2 \delta\left(\epsilon_i - \epsilon_f\right) \rho(\epsilon_f) \tag{3.2}$$

where Ψ_i and Ψ_f are the wave-functions for the initial and final states, ϵ_i and ϵ_f are the initial and final energies, $\rho(\epsilon_f)$ is the density of final states and H_{int} is interaction Hamiltonian that can be given by;

$$H_{int} = \frac{e}{m_e} \mathbf{p} \cdot \mathbf{A} \tag{3.3}$$

where $\mathbf{p}$ is the momentum quantum mechanical operator and $\mathbf{A}$ is the vector potential. Therefore, states and energies in Eq. 3.2 are a combination from the ones of the electron and photon involved in the transition. Within our approximations and using quantization of electromagnetic field, it is possible to separate matrix elements of 3.2 into photon and electronic parts, and then rewrite it in the cross section form in terms of electronics transitions from initial to final electronic states $|\psi_i\rangle \rightarrow |\psi_f\rangle$ as:

$$\sigma = 4\pi^2 \frac{e^2}{4\pi\epsilon_o \hbar c} \hbar\omega |\langle \psi_f | \epsilon \cdot \mathbf{r} | \psi_i \rangle|^2 \delta\left[\hbar\omega - (E_f - E_i)\right] \rho(E_f) \tag{3.4}$$

where $\omega = \omega_f - \omega_i$ is the frequency associated to the state transition, ϵ is the wave polarization vector and $\mathbf{r}$ the electron length operator obtained via Heisenberg equation $[\mathbf{r}, H] = (i\hbar/m)\, \mathbf{p}$, E_f and E_i are the energies for final and initial states respectively. This equation is sometimes referred as the Fermi Golden rule, since it dictates the possible transitions where $\langle \psi_f | \epsilon \cdot \mathbf{r} | \psi_i \rangle$ will only be non-zero when the dipole selection rules, listed below, are satisfied:

$$\begin{aligned} \Delta s &= 0 \\ \Delta m_s &= 0 \\ \Delta l &= \pm\hbar \\ \Delta m_l &= q\hbar = 0, \pm\hbar \\ \Delta J &= \pm\hbar \end{aligned}$$

Here q is a constant dependent on light's polarity (0 for linear and ± 1 for circular polarization) and will be of utter importance for the following paragraphs. In addition, the squared matrix part in Equation 3.2 can be considered a constant, since it only changes slightly with energy, the delta function is equal to unity at edge's energies, meaning that the Intensity of absorption can be written as

$$I = \mathcal{K} \rho(\epsilon_f) \tag{3.5}$$

a constant $\mathcal{K}$ times the density of final empty states. Therefore XANES can directly probe the density of states above Fermi level of a certain element inside a compound, which can provide useful information on the compound's electronic configuration. A more complete explanation on the models portrayed here can be found in [49] [37].

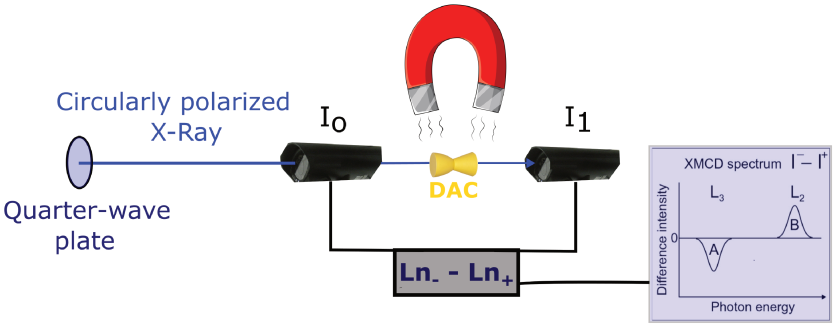

Figure 3.3: *Schematics for a XMCD setup as described in the text. The dichroic signal is a subtraction between the XANES signals coming from positive helicity photons and negative helicity photons.*

Another spectroscopy technique that stems from XANES is the *X-ray magnetic circular dichroism* (XMCD) which uses the same transmission experimental setup as showed before but with a few differences: now the incident X-ray is circularly polarized and the sample may be placed inside a uniform magnetic field created by a electromagnet, as depicted in Figure 3.3. Circularly polarized X-ray may be obtained by using synchrotron radiation out of the electron's plane of orbit or by passing the linearly polarized beams through a quarter wave plate, which details can be found in [50]. What happens now is when the light passes trough a magnetized sample there will be different absorption rates for opposite X-ray helicity's. Therefore we can re-write Equation 3.2 as

$$T_{if}^{\pm} = \frac{2\pi}{\hbar} \left| \langle \Psi_f | H_{int}^{\pm} \rangle | \Psi_i \rangle \right|^2 \delta\left(\epsilon_i - \epsilon_f\right) \rho_{\pm}(\epsilon_f) \tag{3.6}$$

where $T_{if}^{\pm}$ represents the transition probability for positive and negative helicity, $H_{int}^{\pm}$, the Hamiltonian interaction for positive and negative helicity and $\rho_{\pm}(\epsilon_f)$

the empty density of states for majority and minority electrons' spin as will be explained below. The difference in absorption intensity, which is proportional to the difference in transition probabilities

$$\Delta I \propto T_{if}^{-} - T_{if}^{+} \propto \sigma^{+} - \sigma^{-} \tag{3.7}$$

is named the magnetic dichroic signal and is represented in Figure 3.4, and is related to the unbalance of spins near the Fermi level in the element being probed.

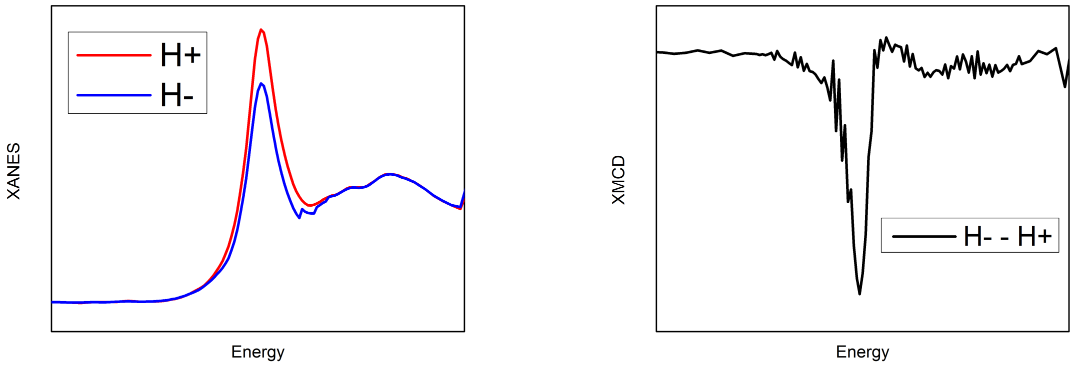

(a)

(b)

Figure 3.4: *In **(a)** we see two theoretical XANES spectra, one for positive photon helicity (H+), in red and other for negative photon helicity (H-)in blue, we clearly see in this exagerated example that we have a difference in absorption for each helicity. In **(b)** we see the subtraction between the H- and H+ signal, which is the XMCD signal.*

To understand how the XMCD effect arises we stick to our approximations utilized previously for XANES and picture the two step model. In the first step we account the interaction between incoming photons and core electrons. Since now the photons are circularly polarized they will have a total angular momentum different than zero, more precisely $l = \hbar$ for right-handed helicity and $l = -\hbar$ for left-handed helicity. We also assume that there is a magnetic field in the same direction of X-ray propagation (which can either be externally applied or internal to the material), which we convention to be the $\vec{z}$ direction, splitting atomic levels due to Zeeman effect. This implies that the photon now interacts directly with the core electron's total angular momentum J, meaning that the electrons being promoted from the core levels will be spin-polarized, carrying the photon angular momentum as a combination of orbital and spin momentum (l+s=J). Therefore there will be different probabilities to excite spin up and down electrons from core shells using positive and negative photons helicity.

In the second step these spin-polarized electrons will occupy an empty level in the first non-occupied outermost electronic shell. However, the applied magnetic field will create (in magnetized materials) majority and minority spins channels near Fermi level, which we define to be spin down and up, respectively. Since core electron promotions must follow the dipole rules listed above spin flip is forbidden ($\Delta m_s = 0$). Thus spin up electrons must be promoted to spin up channels, and spin down electrons must be promoted to spin down channels. Consequently XMCD can probe the magnetism of specific element inside a compound by sensing the unbalance of spins near Fermi level utilizing polarized core holes. In addition, the orbital angular momentum projection must also be conserved ($\Delta m_l = q\hbar = 0, \pm\hbar$), and since q is dependent on the photon's helicity few transitions are further restricted, for example $m_l = 3/2$ electrons can only be promoted to $m_l = 5/2$ channels if $q = \hbar$, and to $m_l = 1/2$ if $q = -\hbar$.

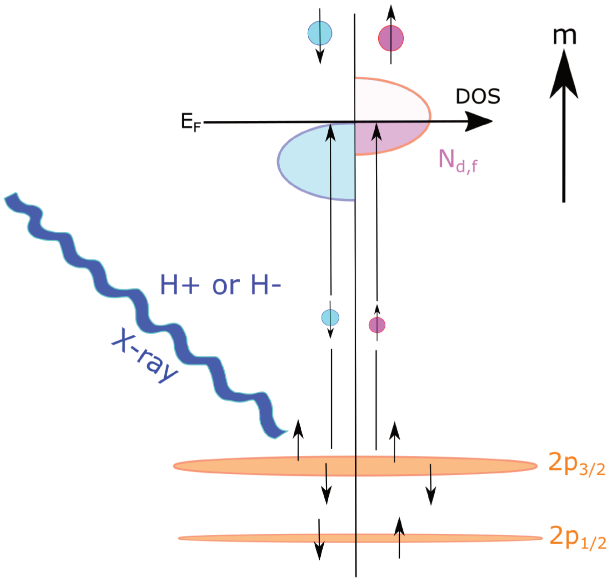

Figure 3.5: *Image representing the XMCD Two Step model for a L3 absorption Edge. The electronic levels are Zeeman split by the applied m magnetic field along the x ray propagation direction. The positive Helicity H+ photons have 62.5% chance to excite spin up electrons, meanwhile the negative helicity H- photons have a 32.5% chance to excite spin up electrons. Since spin up electrons are the minority there only spin up channels available to be filled above Fermi level in this specific example, therefore this difference in probabilities gives rise to the dichroic signal.*

As an example we take a closer look at electron's promotion coming from the core $2p_{3/2}$ shell (L_3 edge) as showed in Figure 3.5. First, X-rays of opposite helicities interact with up and down electrons from the core shell, promoting them with different probabilities: H+ photons (q=$\hbar$) have a 62.5% chance to promote a spin up electrons, and a 37.5% chance to promote a spin down electron. Whereas for H- (q=$-\hbar$) photons the probabilities are flipped, having a 37.5% chance to promote spin up electrons and 62.5% chance to promote spin down electrons. As mentioned before,with the presence of a magnetic field there will be a split between majority and minority spin channels near Fermi level. But we notice that the majority spin channel, spin down, is fully occupied in our example, this way only electrons with spin up will be promoted. Hence, q=$\hbar$ photons promote more spin up electrons than q=$-\hbar$ photons, giving rise to a dichroic signal. More details on XMCD and calculations of core electron promotion probabilities can be found in [37] [51]. Otherwise, if there is no ferromagnetic order present the number of empty levels in both channel would be even and no XMCD signal would appear, making it hard to distinguish between eventual AFM or paramagnetic phases arising. For this reason complementary techniques such as SMS is essential as will be shown next.

3.2 Synchrotron Mössbauer Spectroscopy

In this section we provide a background for general aspects on Synchrotron Mössbauer Spectroscopy (SMS) with providing special attention to Europium isotopes Mössbauer measurements. Traditional Mössbauer technique concepts are presented in Appendix II and, albeit few differences, SMS arises with very similar physics.

3.2.1 Europium containing compounds Mössbauer

There are two natural occurring Eu isotopes that can be used for Mössbauer measurements: Eu-151 and Eu-153. We focus on the most popular one, (and used in this work) Eu-151 which has its decay scheme depicted in Figure 3.6. The transition of interest is the one from 7/2+ excited spin state to the 5/2+ ground state, with a energy of 21.53 keV and a line width of 9.552459×10^{-8} eV [52]. The nuclear radius difference between these two spin states are one of the greatest available for Mossbauer spectroscopy [53], with $\Delta R = 1.28 \times 10^{-17}$m, this makes the isomer shift to produce big displacements in the velocity spectra among many compounds, making it easy to differentiate Eu^{2+} from Eu^{3+} since they can have isomer shifts as big as 5 times the line width. The reason for this is that the 's' shell electronic density is higher at the nucleus for Eu^{3+} than in Eu^{2+} atoms.

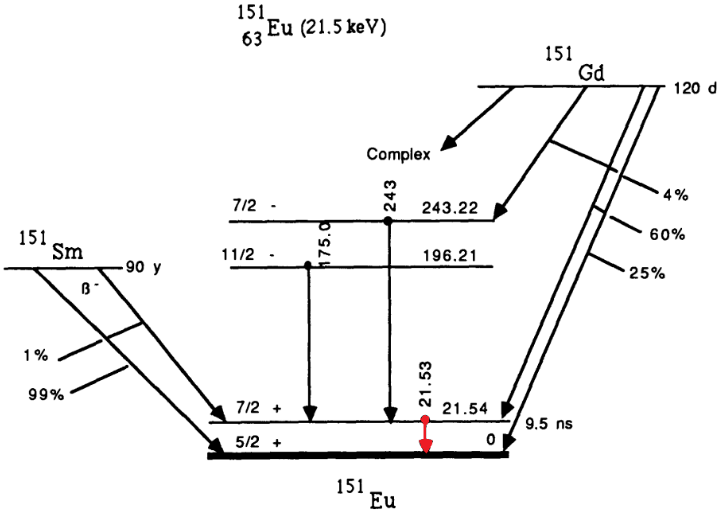

Figure 3.6: *Eu-151 isotope decay scheme. There are two ways to populate the desired 7/2+ excited state in the conventional technique, by either using Sm-151 or Gd-151 radioactive decay pathway with probabilities given in the figure. The transition of interest, from the 7/2+ excited state to the 5/2+ ground state is given by the red line and has an energy of 21.53 keV. Image modified from [52].*

When it comes to quadrupolar splitting excited 7/2+ and ground 5/2+ spin levels of Eu-151 will have lift degeneracy with $m_{I_e} = \frac{1}{2}, \frac{3}{2}, \frac{5}{2}, \frac{7}{2}$ and $m_{I_g} = \frac{1}{2}, \frac{3}{2}, \frac{5}{2}$ as depicted in Figure 3.7. We can also see that there are eight possible transitions allow by dipole selection rules $\Delta m = 0, \pm 1$ (this is the case for $\eta \approx 0$), we can use Equation 6.38 to calculate the energies for each individual level [52]:

$$E = eQ_g V_{zz} \left(1 + \frac{\eta^2}{3}\right)^{1/2} \left\{ \frac{1.34[3m_{I_e}^2 - I_e(I_e + 1)]}{4I_e(2I_e - 1)} - \frac{[3m_{I_g}^2 - I_g(I_g + 1)]}{4I_g(2I_g - 1)} \right\} \tag{3.8}$$

and then make

$$\Delta E = E_{mI_e} - E_{mI_g} \tag{3.9}$$

to calculate each individual energy transition in the presence of quadrupolar splitting. Intensities will be determined by the square of the Clebsch-Gordon coefficients for the spin coupling between excited and ground states and can be found in tables presented in reference [54].

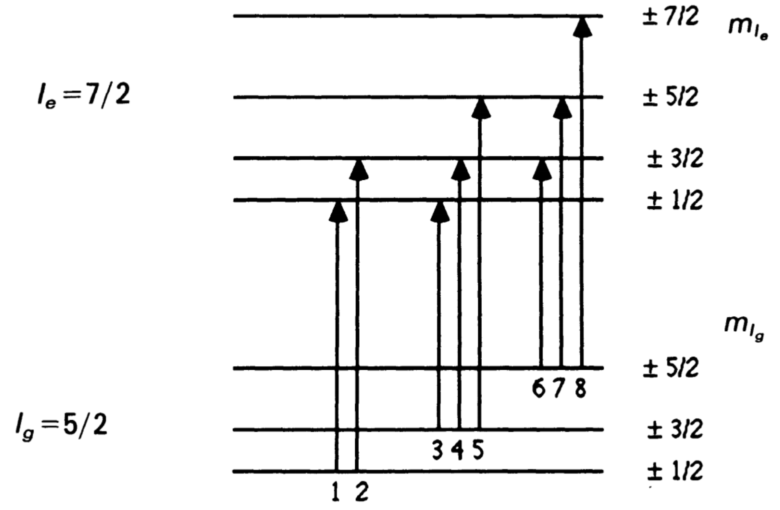

Figure 3.7: *Eu-151 isotope quadrupole split levels for excited and ground state scheme. There are eight possible transitions by emitting photon with energies varying from 21.53 keV by values given in Eq 3.8. Image reproduced from [52].*

When magnetic field is present along Eu-151 nuclei Zeeman split levels will give rise to hyperfine structure with eighteen possible transition between the degenerated 7/2 and 5/2 spin states allowed by dipole selection rules as depicted in Figure 3.8. Although this is the case, only eight transitions can be resolved experimentally since there are coincident difference in energies between some levels. As before, the transition intensities will be given by squaring the appropriate Clebsch-Gordon coefficients [52]. Other aspect that influences on the resolution of each peak is their width as exemplified in Figure 3.9, which show theoretical perfect peaks at the top, with increasing line width along the way to the bottom, passing through ideal cases and arriving to much larger peaks than the usual experimental value of 2.3 mm/s.

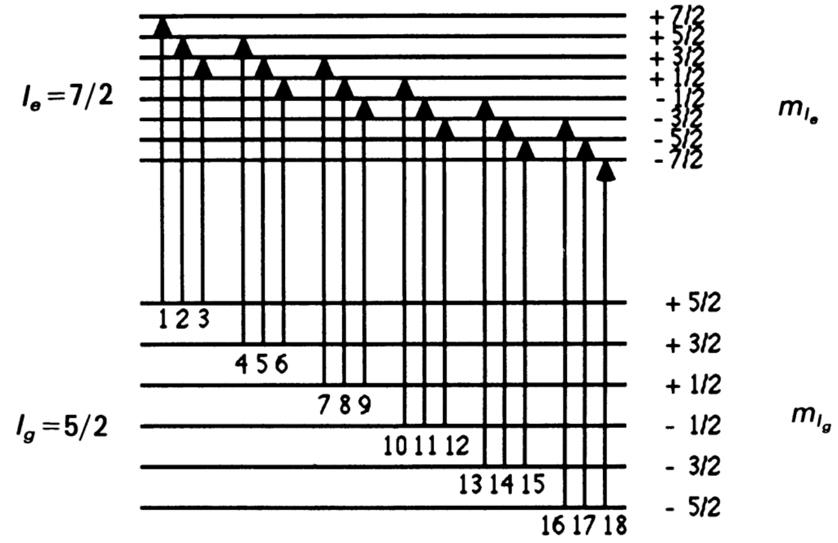

Figure 3.8: *Eu-151 isotope Zeeman split levels for excited and ground state scheme. There are eighteen probable transition paths, but since some transitions energy coincide with each other only 8 can be experimentally resolvable. It is worth to mention that energies may vary with magnetic field magnitude. Image reproduced from [52].*

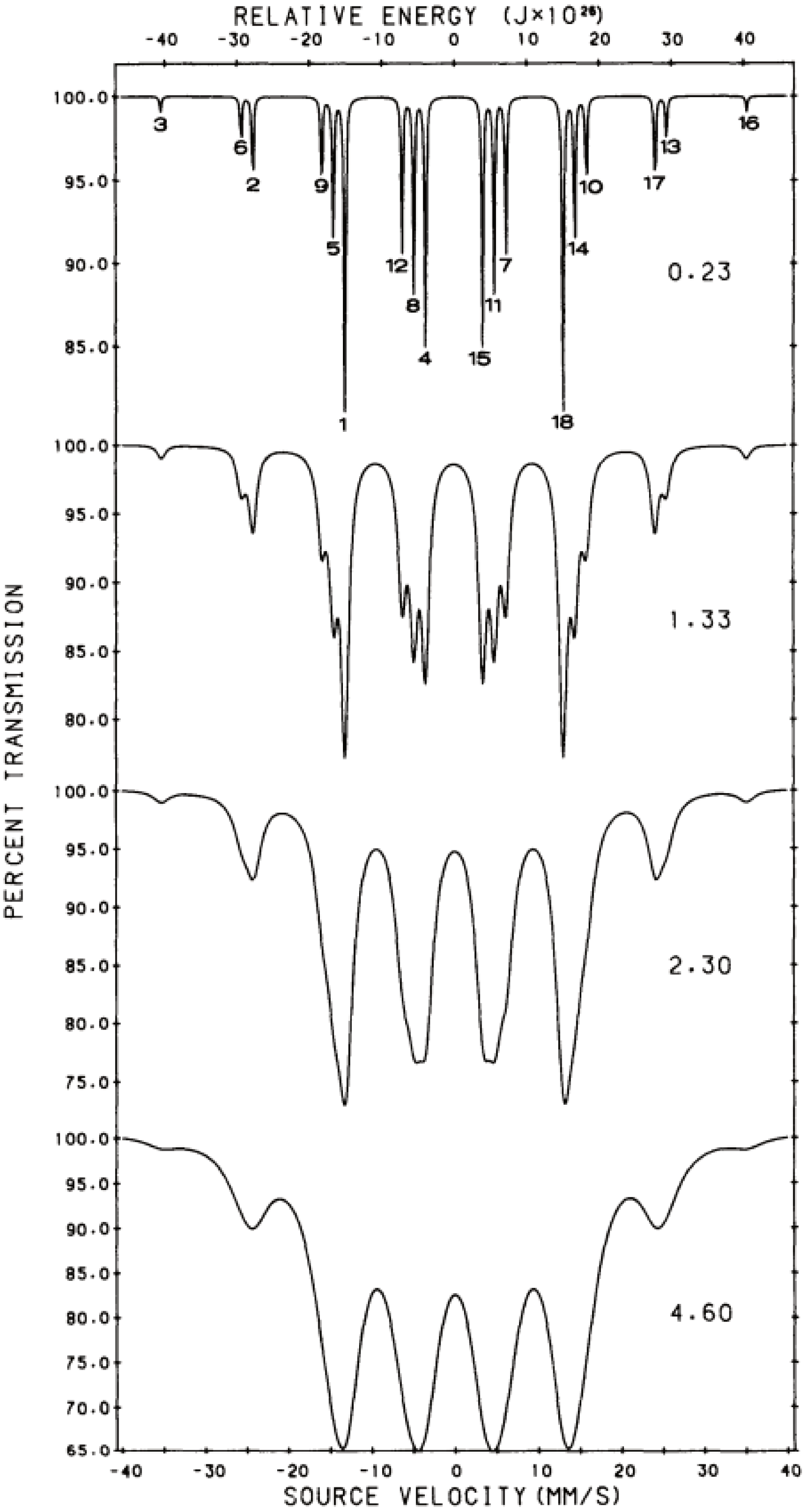

Figure 3.9: *Theoretical Eu-151 isotope Zeeman split levels absorption lines with increasing widths from top to bottom. The line width is present due to transition lifetime and experimental resolution. With good conditions, only eight absorption peaks may be resolvable. [52].*

Early reports for Mössbauer spectroscopy at EuB_6 by Kunii et al. [55] show an Isomer Shift of -13.9 mm/s (relative to a Sm^{151}) at 77 K, in Figure 3.10 and 4.2 K, in Figure 3.11, for two kind of samples: Powder labeled as # 1 and Single Crystal labeled # 2. For the lower temperatures both samples presented hyperfine splitting from the ferromagnetic ordering with Lorentzian peaks fit of a Hamiltonian model providing internal magnetic fields of 261 kOe in sample # 1 and 301 kOe in # 2. It is argued that the difference in H_{int} is due to more vacancies being present in sample #2. But the main point is the stark difference between Mössbauer spectra for when the sample is in the paramagnetic state to when it is ferromagnetically ordered, proving that it is easy to spot the difference between these phases in EuB_6 by utilizing Mössbauer Spectroscopy.

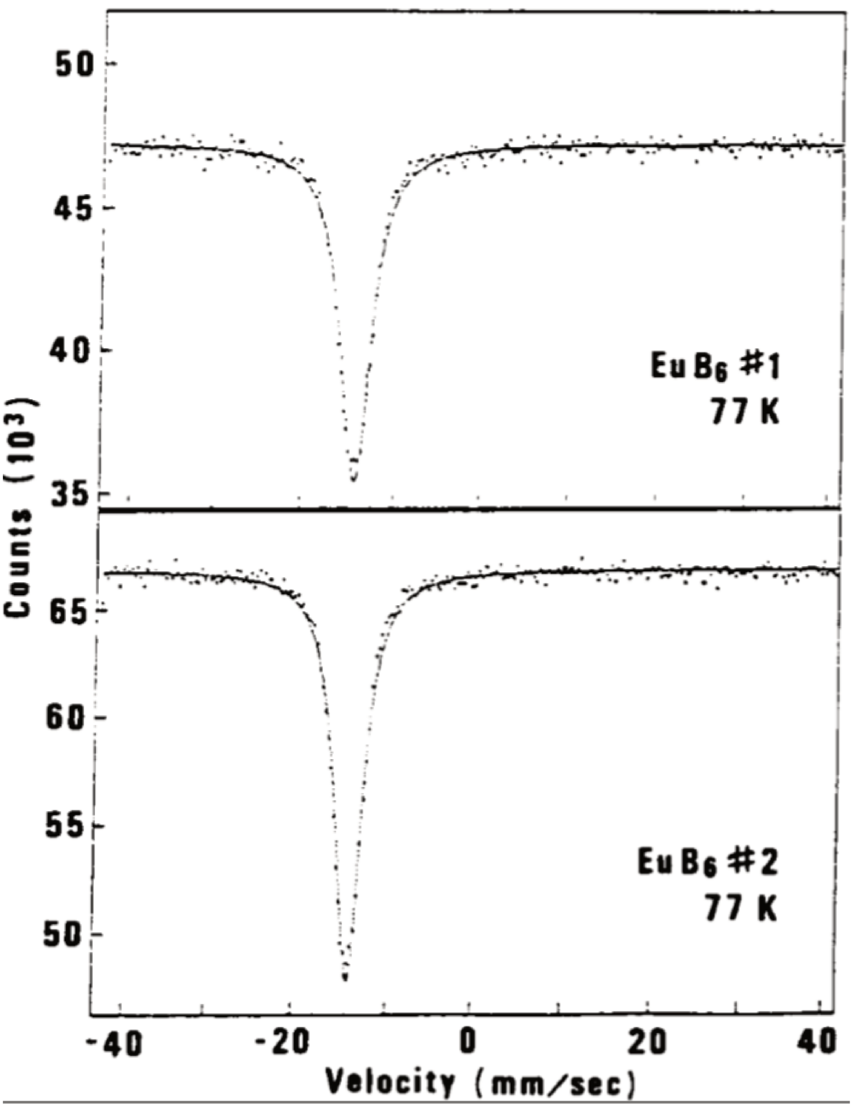

Figure 3.10: *Experimental Mössbauer spectroscopy absorption lines for two* EuB_6 *samples with characteristics discussed in the text. At this temperature the samples present paramagnetic behavior, therefore only the unique absorption line due to the excited to ground state transition is measured. [55].*

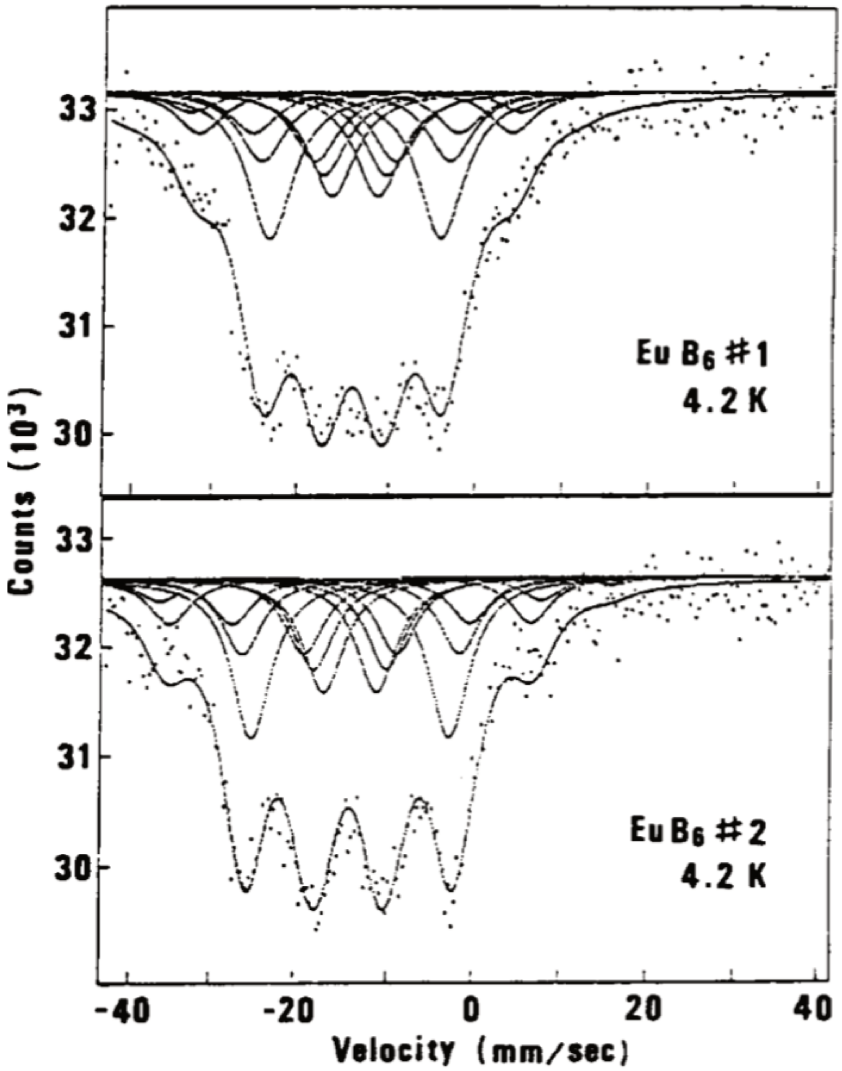

Figure 3.11: *Experimental Mössbauer spectroscopy absorption lines for the same* EuB_6 *samples from Figure 3.10. Now the samples are in the temperature range where there is a ferromagnetic order, causing the single absorption line to be split by the Zeeman effect presenting several distinguishable maxima for absorption. Image reproduced from [55].*

3.2.2 Synchrotron Mössbauer Spectroscopy

The main differences from the conventional Mössbauer technique and Synchrotron Mössbauer Spectroscopy (SMS) are the light source and detecting of photons after resonant re-emission, which consequently provides a different manner to analyze data. A scheme for a beam line prepared for Mossbauer experiments is showed in Figure 3.12. The first important detail starts in the operation of Synchrotron storage ring. As mentioned in the Appendix I there are many ways to arrange electron bunches inside a ring, for a SMS experiments one must use single bunch (or other special/hybrid) operational method. This way there will be pulses of radiation being emitted uniformly separated in time with periods in the order of 100 ns [56]. The beam-line monochromators are specially prepared to select photons precisely, with energy distribution ranging 5 meV or less [57] around the desired value. Since time scale relevant for the experiment are related to excited state half-lifes which are in the nanosecond scale, detectors must have a time resolution in such range. Details for these instrumentation and early developments can be found in [58].

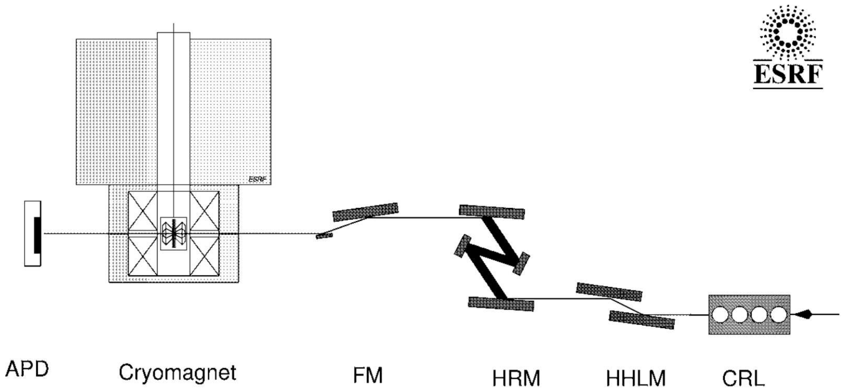

Figure 3.12: *Synchrotron Mössbauer Spectroscopy experiment beam-line setup at the European Source Radiation Facility (ESRF), which is similar for the one utilized in this work. APD stands for Avalanche Photo Diode, the cryomagnet is used as sample space, where high pressure cells can be employed, FM is for Focusing Monochromator, HRM is the High-Resolution Monochromator, NHLM is a High Heat Load Monochromator and CRL is for Compound Refractive Lens. Details for components and instrumentation for this specific setup can be found at the reference from where this image was reproduced [59].*

To exemplify how a SMS experiment works we start depicting the simplest possible case. Suppose one has a non-magnetic and with constant electric field along nuclei sample containing an isotope suitable for Mössbauer experiments (eg: EuB_6 at room temperature). This sample is placed into the cryomagnet of Figure 3.12. The colimated nano-second highly energy resolved pulse of X-Rays (21.54 keV of energy with distribution in the order of 5 meV around it) hits the sample and have a chance to be absorbed by the radioactive isotopes, which are then promoted to the excited state. Some radiation from the pulse can also suffer other absorption processes and/or be transmitted, being detected at the APD as a large peak, represented at 0 ns times in Figure 3.13. After a few nanoseconds, the excited isotopes will start to decay generating a exponentially decreasing intensity gamma-ray signal in the detector as also showed in Figure 3.13. This figure is a pictorial approximation and is exaggerated for didactic purposes. This decay is proportional to the excited state half-life λ, and can be used to gather this information. Since the radiation comes in a broadband and not from a sharp gamma ray emitting atom, the isomershift is not available to be obtained in this specific case, a way to resolve this will be discussed below. It is worth to mention that several hours may be necessary to obtain enough light pulses for a spectra resembling the one in our representation.

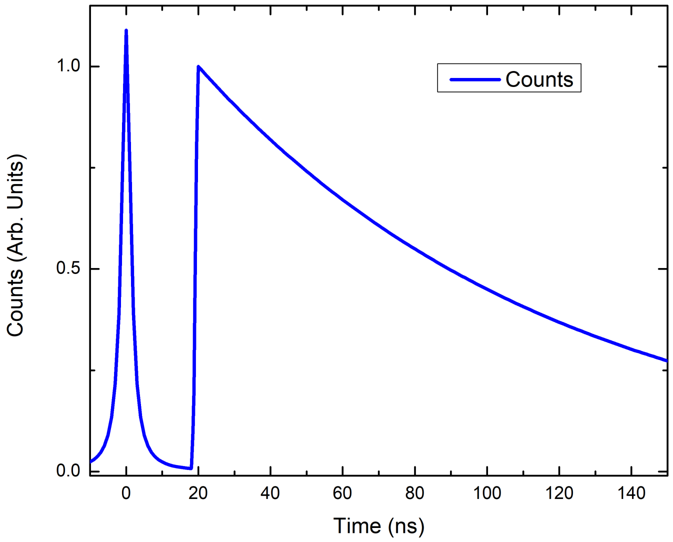

Figure 3.13: *Representative spectra for a Synchrotron Mössbauer Spectroscopy measurement for radioactive isotopes without (hyperfine or quadrupolar) splitting or reference. The peak centered at 0 ms is the synchrotron radiation coming from the single electron bunch rotating in the storage ring, the following exponential decay is the due to gamma ray re-emission from the isotope.*

We now explore a synchrotron Mössbauer spectra for when there a degeneracy lift in energy levels of a single sample. Since we are now exciting the nucleus with a broad synchrotron radiation pulse instead of a sharp gamma-ray all of the possible transitions will occur simultaneously in a isotope. After a period of time this populated excited states will decay, emitting photons coherently with energy separation given by equations 6.38 and 6.40. This photon with similar energy will interfere with each other giving rise to a sinusoidal pattern called quantum beats. A schematic example of a spectra containing quantum beats is showed in Figure 3.14, it presents the same exponential decay dictated by the excited state half-life, but now the interference pattern is also present added to the curve. Furthermore, a mathematical expression describing these quantum beats intensity in function of time is given by [60]:

$$I(t) \propto e^{-\tau} \frac{\chi}{\tau} J_1^2(\sqrt{4\chi\tau}) \left\{ 1 + \sum_{i,j} a_{ij} \cos((\omega_i - \omega_j)t) \right\} \tag{3.10}$$

where χ is the thickness τ is the time given in units of nuclear excited lifetime, a_{ij} is an amplitude parameter depending on radiation polarization and transition probabilities, ω_{ij} are frequencies for each transition between i and j split levels.

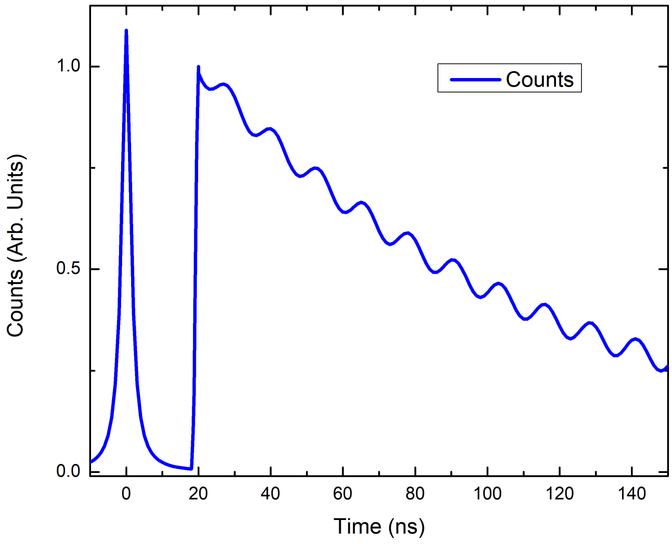

Figure 3.14: *Synchrotron Mössbauer Spectra for a isotope with magnetic hyper-fine (or quadrupolar) splitting. The shape of curve is the same as of Figure 3.13 , but now the interference from remitted coherent light coming from energy split levels generate a sinusoidal signal added to the exponential decay.*

From the discussion above we see that regular and SMS provide equivalent information utilizing different light sources, which is exemplified in Figure

3.15. In the topmost panel we see an example for a transition between degenerate levels with a resulting single absorption peak in conventional technique (energy domain) equivalent to a exponential decay in SMS (time domain). The middle panel shows the equivalency between absorption peaks and exponential decay with quantum beats when a quadrupolar split is in place, a similar pattern may arise when two samples are measured in parallel, with one being used as a reference to obtain information on the isomer shift, which is commonly obtained in conventional tecnique as explained in Appendix II. At the bottom most panel we see a comparison between absorption peaks and quantum beat decaying signal when a magnetic field is present along the isotopes nuclei. Similarly to the velocity spectra absorption peaks, time spectra quantum beats and exponential decays can be fitted by utilizing appropriate simulations that calculate individual contributions for interference patterns. This also make possible to produce equivalent velocity spectra plots from SMS experimental time spectra. Advantages for the synchrotron technique are the beam intensity and tunable Energy without the need of multiple radioactive gamma ray emitters. Finally we conclude by stating that, due to the aforementioned reason SMS has a great potential to be combined with high pressure sample ambient, which is the topic for our following section.

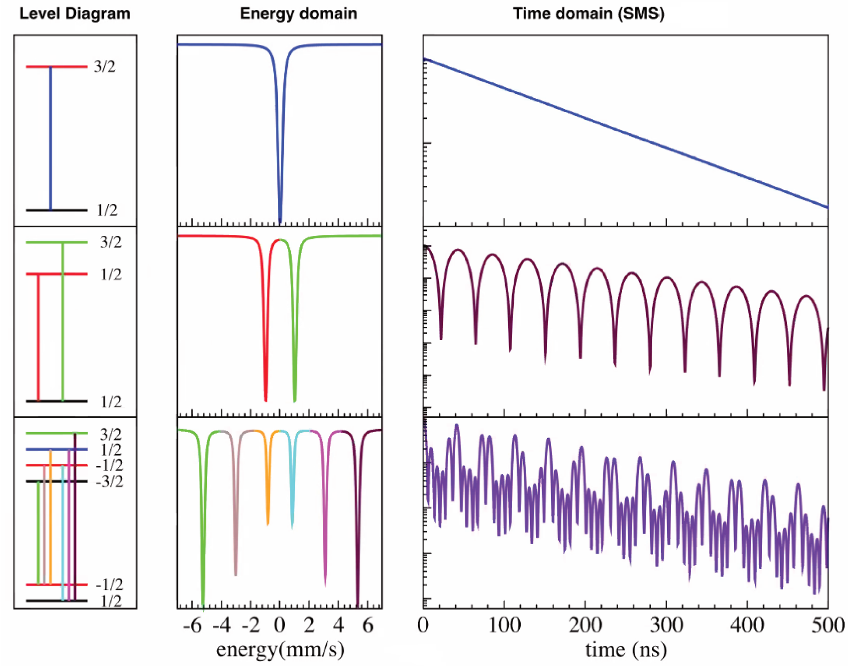

Figure 3.15: *Scheme depicting the equivalence between spectra obtained via the conventional Mossbauer technique (energy domain) and Synchrotron Mössbauer Tecnique (time domain). Note that the vertical axis for the time domain graphics are in the logarithmic scale. Figure courtesy of Ercan Alp.*

Chapter 4

Experimental Methods

This chapter is devoted in explaining relevant experimental details for the used techniques. We start by reviewing high pressure experiments performed in diamond anvil cells detailing how ruby fluorescence provides us information on applied pressure.

4.1 Experiments under high pressures

High pressure physics inside vessels was pioneered by Percy W. Bridgman who was awarded the 1946 physics Nobel prize for his work in the area [61]. The basic concept behind pressure cells is to apply mechanical force into a small area, since

$$P = \frac{F}{A} \tag{4.1}$$

where P is the pressure obtained for an applied force F in an area A. Bridgman did most of his work using cells which trapped small volumes of sample in between metallic pistons and cylinders, which squeezed the material of study by means of screw torque or other mechanical displacement pieces. Early measurements in this kind of cells could achieve up to 10 GPa and were extensively used to determine compressibilities and polymorphic transitions of materials under high pressures [62]

In the next few decades many new pressure cell designs were developed, in pursue to study structural and transport properties of materials in even higher pressures. In this context, the first diamond anvil cell (DAC) was developed by Charles Weir in 1958 [63], where, at first, samples were directly squeezed by micro-metric diamond flat surfaces. Diamonds provide great advantages to high pressure physics since they are hardest occurring material in nature, with great mechanical properties such as low compressability. In the other hand diamonds are fragile and brittle, suffering catastrophic failure when their mechanical limits are surpassed, which usually occur due to crystalline defects propagation in high stress application areas [64]. To avoid cracks, failures and other problems such as sample extrusion through diamond sides and non-uniform pressure along the diamond's face one major development was made in the following years: the gasket, a metal piece containing a hole where the sample is placed together with liquid or gas. This way the sample is trapped inside a chamber in between two diamonds with the fluid serving as a pressure propagating media, ensuring uniform or hydrostatic regime when force is applied by the anvil's diamond tip. One schematic for a Diamond Anvil Cell can be seen in Figure 4.1. The system basically consists in two mono-crystalline diamonds facing each other attached to a piston and a cylinder from where external source of forces can be applied. Since diamonds are transparent to most of the visible part of the electromagnetic spectrum they offer optical advantages if compared to other cells since it is possible to shine visible light, coherent LASER or X-rays into the sample chamber, making spectroscopy measurements feasible and practical as will be discussed next.

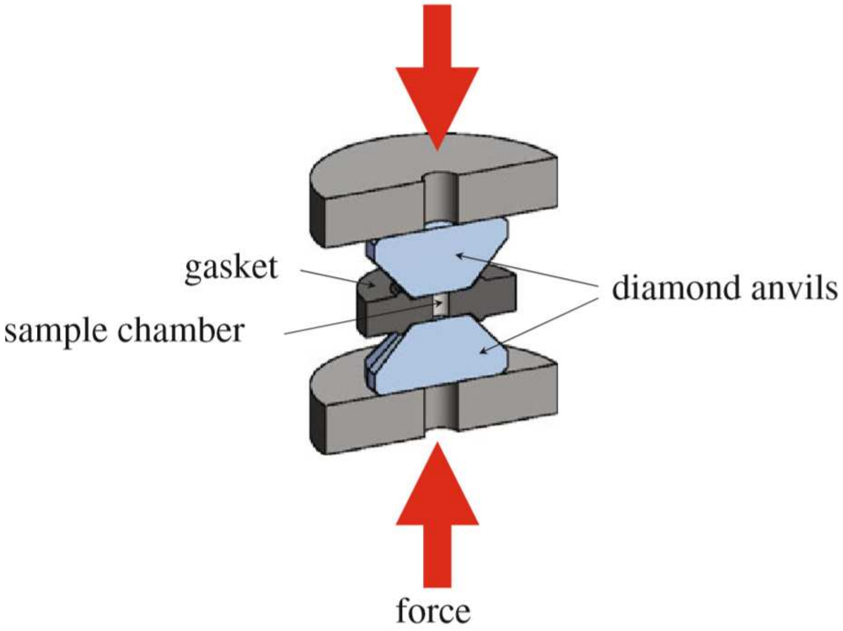

Figure 4.1: *Schematic representing a diamond anvil cell. Two diamond face each other separated by a metallic gasket containing a hole as sample chamber where pressure propagating media, such as a gas or a liquid is also placed together with a ruby crystal, used as manometer as described in the text. Image reproduced from [65].*

The most common way of measuring pressure inside a DAC is by using the ruby (Cr doped Al_2O_3) fluorescence technique, accomplished by shining a laser in a ruby stone placed inside the sample's chamber and capturing the fluorescent light with a spectrometer. The usual spectra obtained is depicted in the graphs of Figure 4.2 where we see two fluorescence peaks, R1 and R2, corresponding to optical decays from excited Cr atoms. The wavelength of those peaks are strongly dependent on the ruby's temperature following [66]:

$$\nu(T) = \nu_o - \alpha_\nu N\left(\frac{T}{\Theta_\nu}\right) \tag{4.2}$$

with ν_o and α_ν being empirically fitted constants and

$$N\left(\frac{T}{\Theta_\nu}\right) = \frac{1}{\exp\left(\Theta/T\right) - 1} \tag{4.3}$$

as a Bose-Einstein phonon occupation probability with Θ being the experimentally fitted Eistein's temperature. The widths of R1 and R2 peaks are given by

$$\Gamma(T) = \Gamma_o - \alpha_\Gamma N\left(\frac{T}{\Theta_\Gamma}\right) \tag{4.4}$$

where Γ_o, α_Γ and Θ_Γ are also experimentally fitted parameters. Both equations are good approximations for temperatures below 300 K. Meanwhile for pressures below 20 GPa the absolute shift in frequency for Cr fluorescence peaks may be given by the linear relation

$$\Delta\nu(P) = \alpha_p P \tag{4.5}$$

where values of -7.61 cm^{-1} and -7.59 cm^{-1} are given for R1 and R2 respectively, as for higher pressures several re-calibration curves have been proposed and account for the non-linear shift of the ruby lines above 20 GPa, [66], including the one used in this work given by [67]:

$$P = \frac{A}{B}\left[\left(\frac{\lambda}{\lambda_o}\right)^B - 1\right] \tag{4.6}$$

with $A = 1976 \pm 6.7$ GPa and $B = 10.71 \pm 0.14$ being the experimentally determined parameters, with $\lambda_o = 694.24$ nm as the wavelength for P=0. Besides that, shape and separation between R1 and R2 lines are a good indicator for how hydrostatic is the pressure inside the cell, since those characteristics are sensible to uniaxial stress.

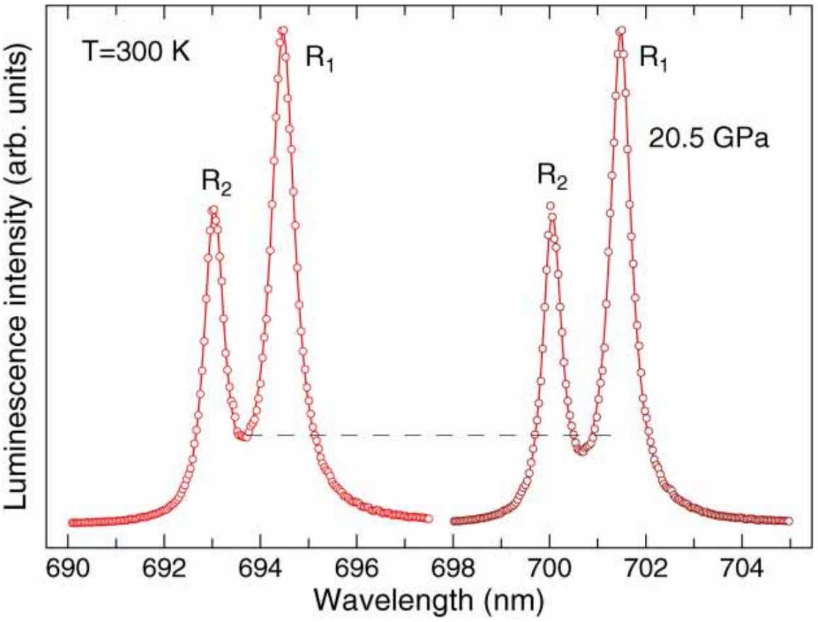

Figure 4.2: *Figure with ruby fluorescence peaks at ambient pressure (lower wavelength) and at 20 GPa (upper wavelength). The shift in photon energy for both fluorescence peaks are due to the change in hydrostatic pressure applied into the ruby. Image reproduced from [66].*

Another advantage brought by the use of DACs is the feasibility of X-ray measurements under extreme conditions of pressure and temperature. Since most diamonds used in cells are single crystals one can avoid most X-ray attenuation if Bragg diffraction conditions are not geometrically favored. This is useful because it is possible to obtain diffraction patterns of the sample only and in absorption geometry the intensity loss will also be mostly due to the sample, making X-ray spectroscopy at synchrotron facilities convenient. As for the temperature DACs fit inside many commercial cryostats, making temperatures in the 10 K range relatively easy to achieve. In addition a gas membrane system, which uses compressed Helium to apply force into de DAC piston, therefore increasing the pressure in a controlled manner, are reliably used at temperature above those of the super-fluid Helium transition.

4.2 X-ray Absorption Spectroscopy Measurements

In this section we provide the experimental details on both XANES and XMCD high pressure measurements and briefly describe the 4-ID-D Advance Photon Source (APS) beamline where they were performed.

The 4-ID branch of the APS has two undulators working in parallel, one which provide low energy X-rays (0.5 keV up to 3 keV) feeding the 4-ID-C soft rays branch and other that provides high energy (3 - 100 keV), feeding the 4-ID-D branch. Details on each one of these undulators can be found in [68] and [69]. We focus on the high energy branch (4-ID-D) where we performed our XAS experiments. At first, light coming out the storage ring is linearly polarized (as mentioned in previous sections), the photons then go trough the optical hutch elements depicted in Figure 4.3. The monochromator mirrors select the photon energy by using a combination of movements from both Si crystals, which allows for adjusts or Energy scans during experiments with a resolution of $\Delta E/E = 1.4 \times 10^{-4}$. The next optical elements are phase retarders which circularly polarize the incident radiation, being the X-ray correspondent of what quarter wave plates are for visible light, although the functioning principle behind the phase shifts are of different nature. Finally, the beam hits two mirrors used for focusing and collimation before proceeding to the experimental hutch.

More details on the information provided on this paragraph can be found in [70].

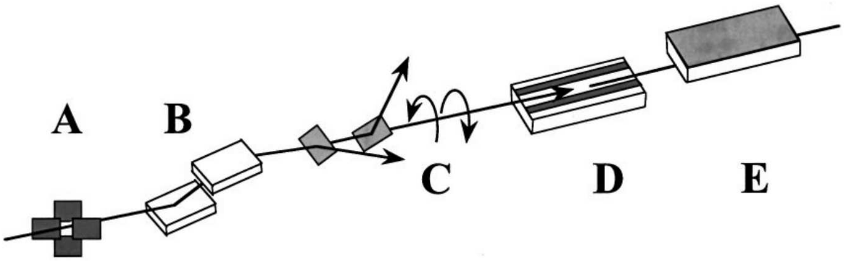

Figure 4.3: *Optical elements of the 4-ID-D beamline at the APS. A - Slits for flux control. B - Monochromator Si adjustable mirrors. C - Phase retarders for circular polarization D - Concave mirror for focusing. E - Flat mirror for collimation. Figure adapted from [70]*

In the experimental hutch an optical table is present, therefore a vast range of setups may be adjusted depending on technique. In our case we employed two Si photo-detectors, one before the sample space and other after, being name I0 and I1 as in the usual optical transmission geometry. In regards to the sample space a mini-DAC was placed in helium-flow cryostat, which on its turn was positioned inside a superconductor electromagnet capable of producing 4 T fields.

As for the sample, EuB_6 single crystals were crushed into a fine powder and placed in between two diamonds (350 μm). To do so a rhenium gasket was pre-indented and laser drilled [70], so there would be an empty space for EuB_6 and a ruby stone with 15 μm of diameter to be encapsulated. In order to obtain hidrostatic pressure silicon oil was employed, embedding both sample and ruby inside the gasket's sample chamber.

At first a remaining amount of sample was placed in between Kapton tapes, which are ideal for vacuum and low temperature environments, and inserted inside the cryostat for preliminary adjusts regarding photon energy and circular polarization. In order to obtain an optimized XMCD signal a lock-in system, which shifts the phase retarders from left to right helicity obtaining postions in a quickly manner (in the order of 10 Hz) was used. This improves the signal by getting rid of eventual spurious noises by performing several XMCD signal measurements in a short period of time, instead of a single signal after many minutes of exposure for one helicity and then for the other.

Measurements at ambient pressure and at the base temperature for the cryostat (6K) were then performed. Photon flux attenuation was needed since radiation power was heating the sample. Maximum absorption was observed at 6.977 keV, and it was adopted as the center reference energy during the experiment's entirety. XANES and XMCD signal were measured simultaneously using fields of 1 T and -1 T at the photon flux direction, while lock-in phase retarder system changed photon helicity continuously at a rate of 13 Hz. Energy scans were performed by changing monochromator feedback motors, starting at 6.927 keV up to 7.025 keV. Steps of 2 eV were taken in pre (6.927 keV - 6.957 keV) and post-edge (7.02 keV - 7.025 keV) regions while close to the absorption edge (6.957 keV - 7.02 keV) 0.5 eV steps were performed for better resolution. Hysteresis measurements were also performed from -2 T to 2 T at 0.05 T steps. The temperatures selected for these and following measurement were of 6 K, 13 K and 25 K, with few points of higher temperature eventually. Results will be discussed in the next chapter.

Similar procedures and parameters were used for the high pressure measurements, but now extra care was taken to eliminate glitches in the spectra due to diamond Bragg peaks. For this experiment a miniature version of a DAC was used in order to fit the space inside the cryostat. To apply pressure it was needed to heat the DAC up to room temperature and apply torque to the cell screws. Because of that, some variation in the pressure was expected, since compression due to thermal dilatation may squeeze the sample while cooling down or heating up. For this reason pressure before and after a battery of spectroscopy measurements was recorded, and are presented in Figure 4.4. The solid points represent the averaged pressure taken between final and initial ones, while the bars represent the variation. Usually pressure before measurements was lower than at the end. As showed in the same picture, eight pressure points were measured and the resulting XAS spectra collected for each one are shown and discussed in the next Chapter.

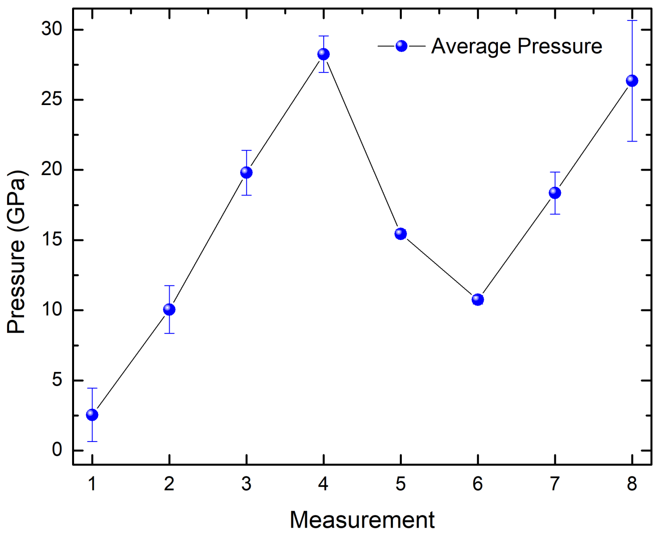

Figure 4.4: *Applied pressure path for XANES and XMCD experiments. The blue points represent an averaged pressure from the values obtained before and after the measurements, which are represented by the tips of the vertical blue bars.*

4.3 Synchrotron Mössbauer Spectroscopy

High pressure Synchrotron Mössbauer Experiments (SMS) were performed at the 3-ID-C beamline of the Advanced Photon Source (APS). During this experiment storage ring was operating in a 24 electron bunches mode with 153 ns separation in time between them [71]. This beamline is equipped with a high resolution monochromator (HRM) and Avalanche Photon Detectors with nanosecond time resolution, both designed for nuclear forward scattering experiments such as SMS, more details for this line's components can be found in [72], [72] and [73]. The energy selected for the experiments was of 21.54 keV correspondent to the $\frac{7}{2} \rightarrow \frac{5}{2}$ Eu-151 radioactive decay. HRM was set for this energy and provided resolution of few meV around it. Within such range of precision, thermal variation on optics components (such as in Si crystals) can cause a drift on photon energy and collimation, requiring constant adjustment via tweaks in the feedback piezoelectric motors.

EuB_6 fine powder was obtained by crushing single crystal from the same batch used for XAS experiments, and placed inside a rhenium gasket pre-indented by the 300 um diamond cullets which were attached to the mini-panoramic DAC portrayed in Figure 4.5. As previously mentioned in the preceding section, sample space was created in the gasket by perforating a centralized hole using laser drilling techniques [70], a ruby crystal sphere with approximately 15 μm diameter was placed in the sample chamber as well and helium gas (which provide a better hidrostatic pressure than silicon oil) was used as pressure media, being inserted via a gas loading system which evolves the cell into an atmosphere of compressed gas and allows the DAC to be closed remotely, trapping such gas inside the gasket's hole [74]. This loading process has advantages over other pressure medias since this gas allows higher ranges of hidrostacity [75].

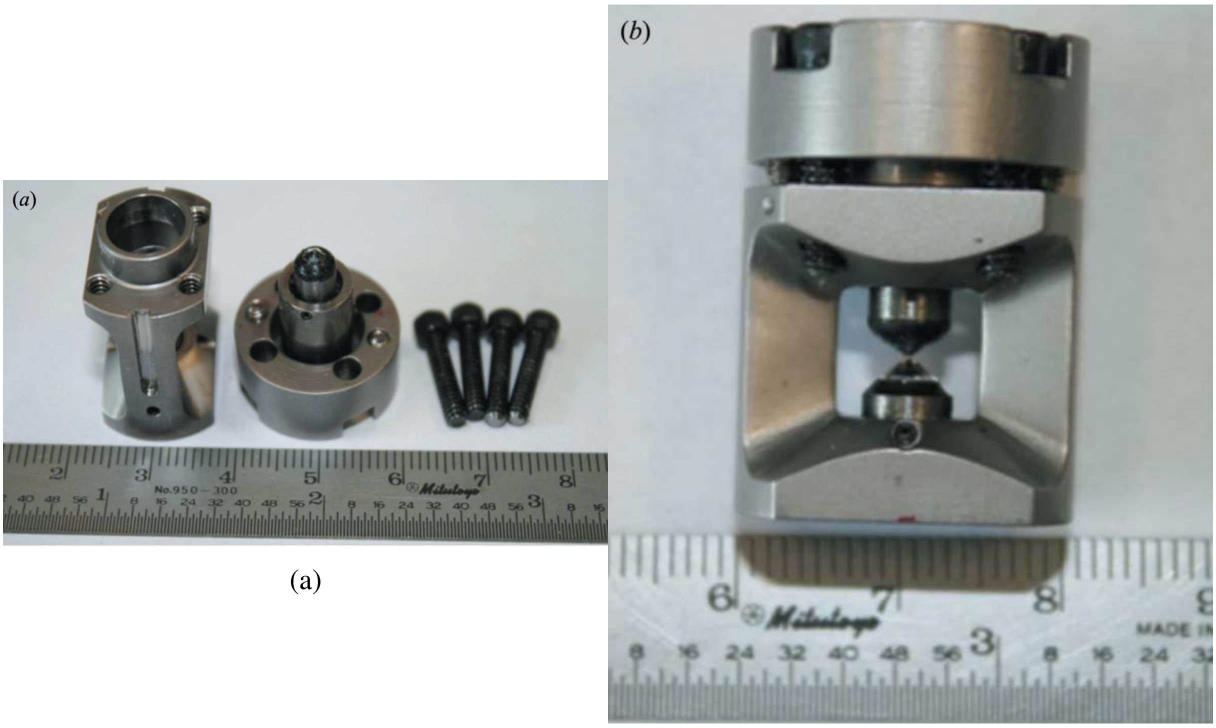

(a)

(b)

Figure 4.5: *Picture of the mini-panoramic diamond anvil cells (DACs) utilized for the synchrotron Mössbauer spectroscopy measurements. At figure (a) we see the open cell with cylinder in the left side, piston in the middle and screws at the right. Figure (b) shows the closed cell with diamond facing each other at the middle, in this case there is no gasket which would be in between them. Figure reproduced from [71].*

Inside the 3-ID-C beamline experimental hutch a system with a cryostat and pressure propagating helium membrane was assembled. The cryostat base temperature was of 9 K and used liquid helium flow for cooling. The membrane system used pressurized helium gas pipes to apply force into the DAC piston. Gas flow was adjusted by a Diacell GM Controller A75013, allowing to rise the pressure in a quasi-linear behavior, or small steps to avoid diamond cracks. Pressure was measured in-situ using ruby fluorescence system parallel to the X-ray path providing higher precision pressure measurements within the ruby scale experimental error.

Data was acquired for several pressures and temperatures and with the different referencing materials, EuS and Eu_2O_3 as summarized in Table 4.1. For the measurements with references a thin slab of each material with variable thickness were glued to a moving stage and placed in the X-ray path right in front of the sample. In order to have an equally distributed signal intensity from either sample (EuB_6) and reference (EuS and Eu_2O_3) the moving stage was adjusted so the APD counts would be double the of amount in comparing to No-Reference measurements. This is done to easily identify eventual beats arising from isomer shifts. Each spectra would take in between one to three hours to offer good signal to noise ratio as observed during the process. Results will be shown and discussed in the following chapter.

Pressure (GPa)	No Reference	EuS Reference	Eu_2O_3 Reference
0	297 K	n/a	n/a
1.2	297 K	297 K	n/a
1.9	297 K	n/a	297 K
5	9 K, 20 K	9 K, 20 K, 40 K	n/a
10	9 K, 20 K	9 K, 20 K	n/a
14.5	9 K, 20 K	9 K, 20 K	9 K, 20 K
18	9 K, 20 K	n/a	9 K
21	9 K	9 K	9 K
24	9 K, 20 K	n/a	9 K, 20 K
29.5	9 K, 20 K	9 K, 20 K	9 K, 20 K

Table 4.1: *List of experimental data points taken for the synchrotron Mössbauer spectroscopy measurements. Each line is for the measured pressure and each column for the used Reference, the temperature for each measurement, when available is given in the box. 0 (zero) GPa means ambient pressure.*

Chapter 5

Results and Discussion

5.1 Ambient pressure Sample characterization

In this section results from ambient pressure physical properties measurements systems at Laboratório de Metais e Ligas (LML), Grupo de Propriedades Ópticas e Magnéticas de Sólidos (GPOMS) and Max Planck Institute (MPI) are presented.

5.1.1 Specific Heat

Specific heat measurements are shown in Figure 5.1 together with results found in the literature [76] [11] for comparison. In our data (blue line) it is evident a broad peak with maximum near 11 K as observed in the work of Sullow et al (red line). This broad feature is due to magnetic ordering of the 4f Eu momenta in long order ferromagnetic transition. In the other hand c$_p$ from Fujita et al sample (black line) has a similar feature in a lower temperature, showing that this peak shifts in temperature depending on sample quality, since Fujita's sample's deliberately had carbon impurities. Another observed feature in our measurement is a bump near 15 K, related to T_{c1} and the coalescence of magnetic polarons, and is only observed in higher purity samples. Still, Sullow's sample has a much more prominent feature in the same temperature range, which can be accounted due to measurement resolution and higher sample quality.

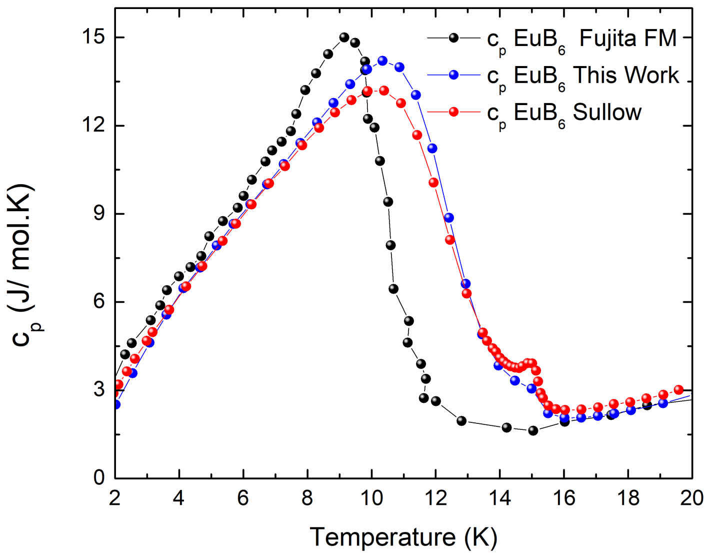

Figure 5.1: *Specific Heat measurements (in blue) compared to one performed in a sample with carbon impurities from Fujita et al [76] and other with a high purity sample from the work of Sullow et al [11], illustrating that the amount of impurities has considerable effect on lower temperature* T_{C1} *structure and high temperature* T_{C2} *feature.*

In Figure 5.2 we present a graph of c_p/T of our measurements where we see a broad feature from 11 K and below and a bump at 15 K. The Debye temperature of 181 K was found by fitting data in the interval between 17 K and 27 K and the obtained theoretical function is plotted as an orange line in the graphic. After subtracting the phonon contribution obtained by the Debye model [38], data was integrated in order to obtain the system's entropy with result presented in the inset. Theoretically expected value for magnetic entropy saturation at T$_c$ for an Eu^{2+} with the J=$7/2$ configuration is of $R\ln(8)$, our sample reaches 91% of that value at 15 K and still presents an increasing entropy even above the upper EuB$_6$ Curie's temperature. This could indicate a further magnetic entropy at higher temperatures due to a magnetic polaron contribution. Still, such claim requires further investigation which is outside the scopes of this work.

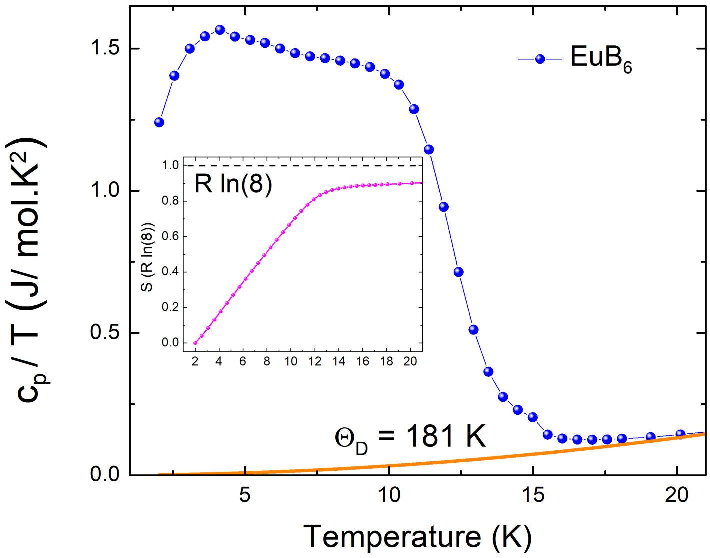

Figure 5.2: *Graphic of c_p/T for our EuB$_6$ single crystal with no applied magnetic field. The orange line represents the fitted Debye model curve with a $\Theta_D = 181$ K accounting for the lattice contribution on specific heat. The inset shows the entropy obtained of the system which at 15 K reaches a value of $0.91R\ln(8)$ J/mol K^2.*

5.1.2 Magnetization

We present sample magnetization measurements in Figure 5.3 where we compare two normalized curves, one for EuB_6 single crystal and other for a crushed single crystal powder. The powder sample magnetization was taken under an applied field of 200 Oe while single crystal had an applied field of 500 Oe. The curves shape near transition temperature are fairly equal, with a slightly different behavior between 20 K and 30 K with may be attributed to the field difference and anysotropy. It is reported that EuB_6 has some anysotropy in the magnetism [11], and since powder sample has randomly oriented crystallite there will be averaged contribution from each principal axis being measured simultaneously. Despite this fact, presented results suggests that magnetization properties are fairly similar in both kind of samples as evidenced by the same transition temperature of 15 K obtained by first order derivative in function of temperature depicted in Figure 5.3 inset.

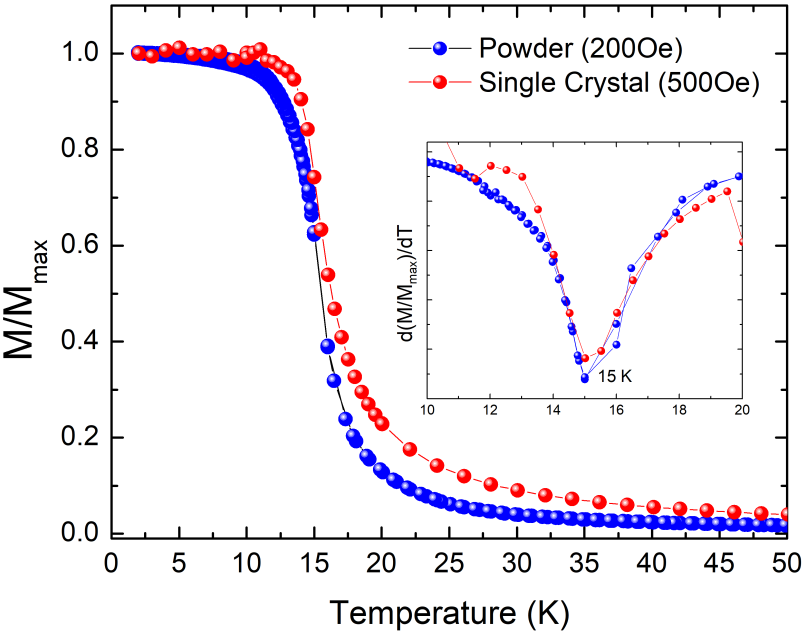

Figure 5.3: *Normalized magnetization for powder (crushed single crystal), in Blue, and a single Crystal, in Red. Inset shows first derivative for each measurement with matching colors.*

In order to characterize the type of magnetic ordering of the material, field dependence magnetization curves are essential. Figure 5.4 presents results for powder EuB_6 magnetic moment in function of applied magnetic field for several temperatures. We see that 2 K and 6 K we have soft ferromagnetic behavior with saturation occurring at 1 T of applied field at 2 K and a slight difference for 6 K. As for 10 K and 13 K, just below and above the ferromagnetic ordering temperature T_{c2}, respectively, we also see a ferromagnetic behavior but with saturation values not being attained up to the maximum employed applied field of 4 T. At any of these measurements there were not a visible hysteresis which if exists occurs with values of field below resolution of the experimental equipment. As for 25 K there is a more linearly dependent behavior as expected for paramagnetic regimes but with a visible distortion for field between -1 T and 1 T which is usually observed in ferromagnetic sample when close to their critical temperature.

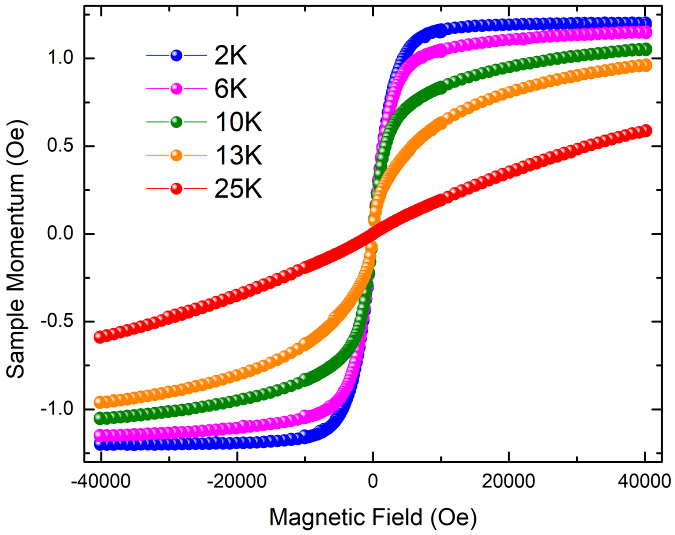

Figure 5.4: *Sample magnetic momentum in function of applied field from -4 T to 4 T in a crushed single crystal EuB*$_6$ *sample inside a SQUID magnetometer for temperatures as showed in the graph.*

In Figure 5.5 we show the inverse magnetic susceptibility obtained through magnetization measurement for a EuB$_6$ single crystal which was also used for transport measurements. Our analysis using the Curie-Weiss model for a fit above 100 K provided us a Curie Temperature of 12.62 K, which is in close agreement to the value found for T$_{c2}$ in our sample, but differs significantly from values found in the literature which are usually closer to T$_{c1}$ $\approx$ 15 K. As for the obtained magnetic effective moment of 8.165 μ_B it is close to the theoretical value obtained for Eu^{2+} atoms of 7.94μ_B and is in agreement with previously reported results mentioned in Chapter 2.

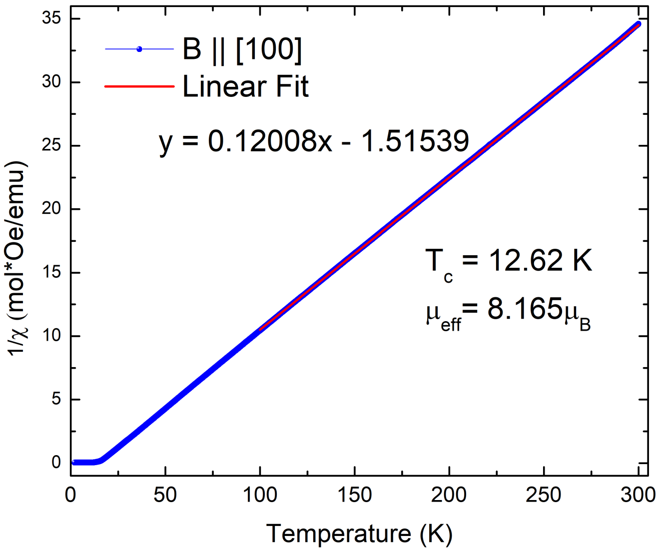

Figure 5.5: *Inverse of the magnetic susceptibility obtained in a singe crystal EuB*$_6$ *sample. The applied field was of 500 Oe along the [100] crystallographic direction. Red line shows the linear fit between 100 K and 300 K with obtained equation presented together with the values obtained from the Curie-Weiss for* T_c *and effective moment* μ_{eff}.

5.1.3 Resistivity

Transport measurements can provide us valuable information on magnetic properties while also offering means to attest sample quality. The results for 0 field resistivity can be seen in Figure 5.6 where both cooling and heating curves are in top of each other. The calculated residual resistivity ration (RRR) coefficient ($\rho(300K)/\rho(2K)$), which is commonly used to determine residual resistance due to defects was found to be 48.9, demonstrating the sample's good quality. We can clearly see a transition happening at $\approx$15 K with a sudden drop for the resistivity at lower temperatures, more careful inspection utilizing a first derivative in function of temperature (inset of Figure 5.6) show us two subsequent transitions, one at Tc_1 = 14.7 K and other at Tc_2= 12.2 K, which agrees with previously mentioned literature results for these temperatures [21].

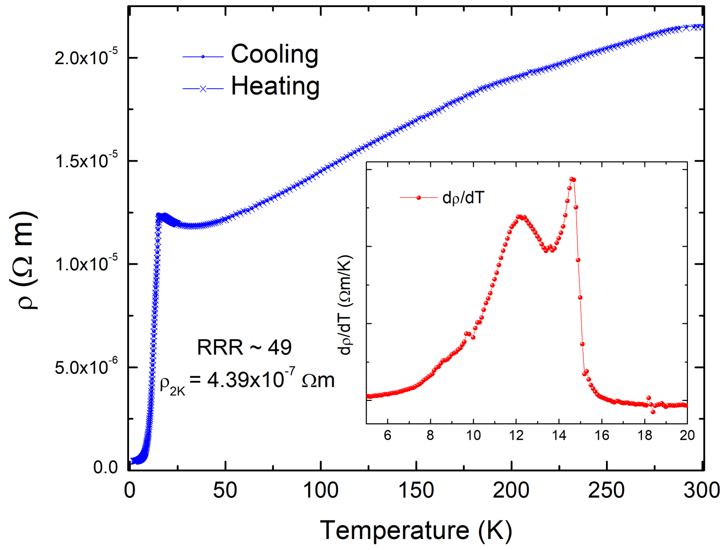

Figure 5.6: *Zero field resistivity for a* EuB_6 *single crystal. The cooling and heating curves are on top of each other showing no difference within the equipment's precision. The RRR value and resistivity at 2 K are shown in the graph. The inset shows a first derivative of the resistivity in function of temperature with maxima at* Tc_1 *= 14.7 K and* Tc_2*= 12.2 K.*

5.1.4 XANES and XMCD

We now present results for X-ray near edge spectroscopy (XANES) and X-ray circular Mmagnetic dichroism (XMCD) for ambient pressure in a jointly manner as for the concomitant nature of the measurements. These results are used to further characterize the sample with synchrotron techniques. Crushed single crystal powder evolved by kapton tape at ambient pressure provided results shown in Figure 5.7. Temperatures depicted in the graphic are nominal ones given by the cryostat sensor which later were found not to be the same at sample, which was estimated to be few Kelvin higher due to X-ray heating. XANES and XMCD data are normalized by the absorption jump between pre-edge and post-Edge regions. Energy for the L_3 absorption edge peak was found at 6.976 keV while peaks XMCD signal is centralized around 6.974 keV, which are in close agreement to the theoretical value. We clearly see the XMCD signal drop with increasing temperature, showing that the difference from a ferromagnetic state to a paramagnetic state is discernible even with the applied magnetic field of 1 T.

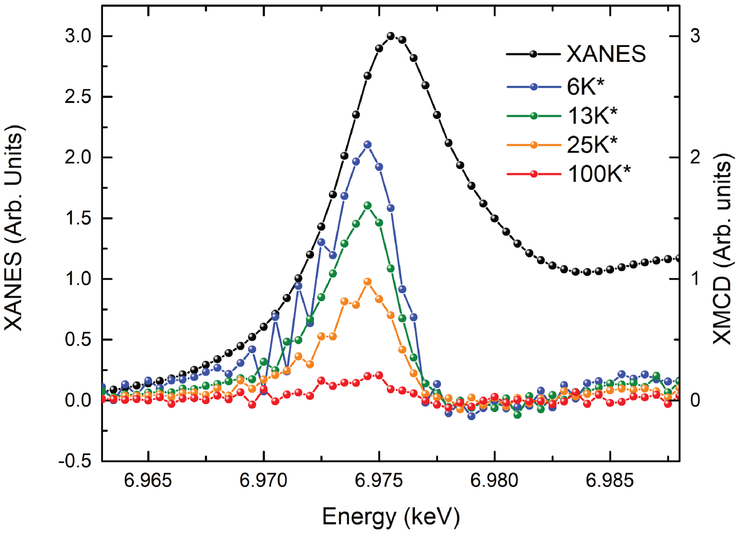

Figure 5.7: *Measurements for XANES (in black left side scale) and XMCD in a* EuB_6 *powder sample evolved in kapton tape at ambient pressure. Temperatures are marked with an asterisk since due to photon absorption they were found to be significantly higher at the sample than nominal temperature at cryostat sensor.*

Figure 5.8 shows results for XMCD signal in function of applied field from -2 T to 2 T for nominal temperatures of 6 K, 13 K and 25 K. We clearly see a ferromagnetic behavior for the two lower temperature measurements with a linear field dependence for the higher temperature showing a paramagnetic behavior. This magnetization curves are qualitatively comparable to the curves obtained in the SQUID-PPMS presented in the previous subsection, further confirming a divalent and ferromagnetic behavior for EuB_6 at low temperatures as already extensively reported in the literature. In the following section we show how these characteristics evolve with lattice contraction by applying hidrostatic pressure.

*

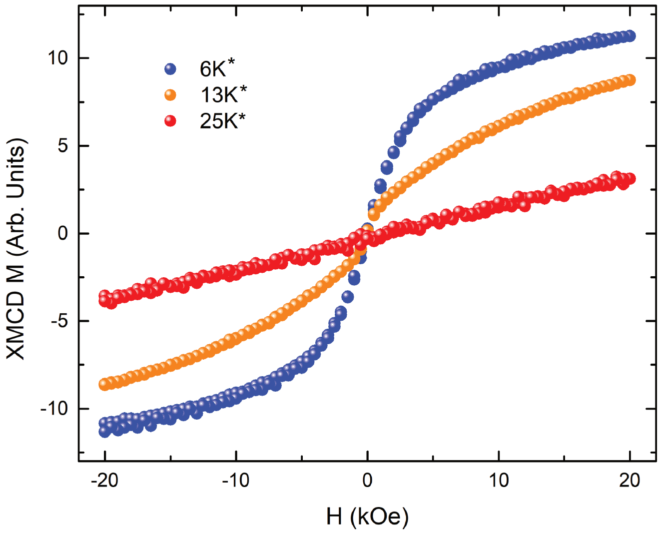

Figure 5.8: *Measurements for XMCD in function of applied field in a* EuB_6 *powder sample evolved in kapton tape at ambient pressure. Temperatures are marked with an asterisk since due to photon absorption they were found to be significantly higher at the sample than nominal temperature at cryostat sensor.*

5.2 High Pressure Measurements

In this section we present high pressures XAS and SMS results with which we can explore magnetic and electronic properties as a function of lattice contraction at pressure values never before achieved for this compound, allowing us to expand our understanding for the EuB_6 behavior under extreme conditions beyond the 17 GPa threshold previously achieved by resistivity measurements [21].

5.2.1 XANES and XMCD

High Pressure XMCD spectra are shown in Figure 5.9, where they were separated into ascending (a) and descending (b) applied pressures. The entire data set was obtained at a temperature of 6 K and applied field of 4 T, except for 2.5 GPa and 10 GPa where we have a temperature of 6 K but fields of 1 T. In (a) we see the evolution of the XMCD signal with increasing applied pressure, where it is clear that for 2.5 GPa and 10 GPa we have a intense dichroic signal in agreement with the previously reported ferromagnetic behavior [21] at this pressure range. In the other hand, at 19.8 GPa we see a significant XMCD signal drop indicating an EuB_6 magnetic behavior change. In response to the signal drop we decided to increase applied field up to 4 T assuring that even a dim dichroic signal would be perceived. This should not have much influence in comparisons since at 1 T EuB_6 magnetization is near saturation as showed previously. Furthermore, at 28.5 GPa we see that the signal completely vanishes. The lack of dichroic signal show us that at this pressure EuB_6 no longer orders in a ferromagnetic manner.

In figure 5.9 (b) we see XMCD signal evolution for a descending pressure (pressure path has maxima and minima as shown in Figure 4.4), showing that by releasing the pressure cell down to 18.4 GPa makes the dichroic signal reappear. This not only further confirms a strong change in magnetic order for the compound, as once more evident by the stark difference between 26.3 GPa and remaining peak amplitudes, but also indicates that the magnetic phase transformation process has a reversible character. It may be argued that the signal difference between 2.5 GPa, 10 GPa 15.3 GPa and 18.4 GPa can be attributed to signal noise and pressure uncertainty, but the difference between these signals and those for 19.8 GPa, 26.3 GPa and 28.5 GPa is large enough to indubitably represent a change in magnetic ordering, as evidenced in Figure 5.10. This way argue that above $\approx$ 20 GPa there is a change from the previously reported ferromagnetic character for EuB_6 coming from Eu^{2+} ions up to 17 GPa. From XMCD alone we can neither resolve between an antiferromagnetic and paramagnetic behavior nor obtain information on electronic character such as mean valence of the material. Since decreasing lattice parameter may rise the population of non-magnetic Eu^{3+} ions (since they are smaller than Eu^{2+} ones) we investigate this possibility by analyzing XANES spectra obtained concomitantly with the presented XMCD spectra.

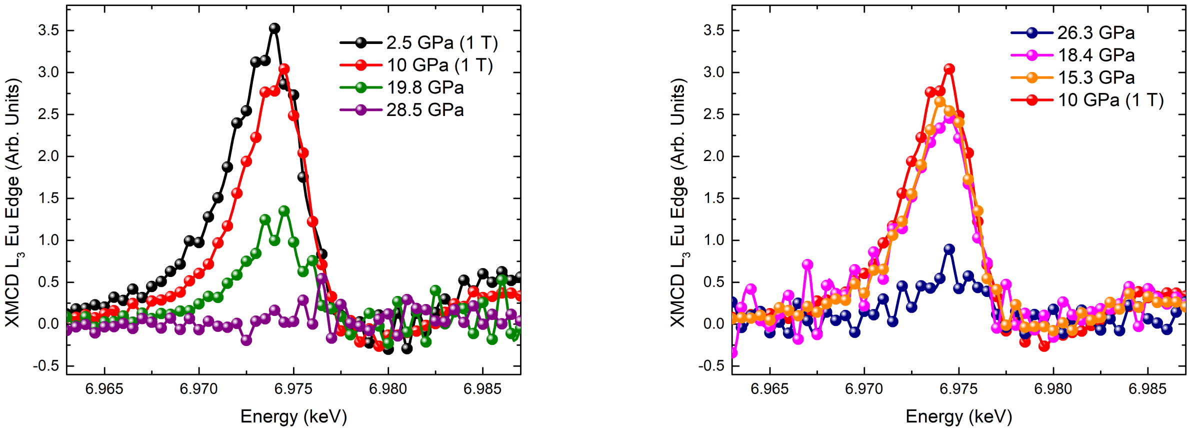

(a) (b)

Figure 5.9: *Graphics with ascending (a) and descending (b) high pressure XMCD as indicated in the graphs. Measurement order is depicted in Figure 4.4. We clearly see that for pressures of 28.5 GPa and 26.3 GPa the XMCD signal is much lower than for pressures of 15 GPa and below.*

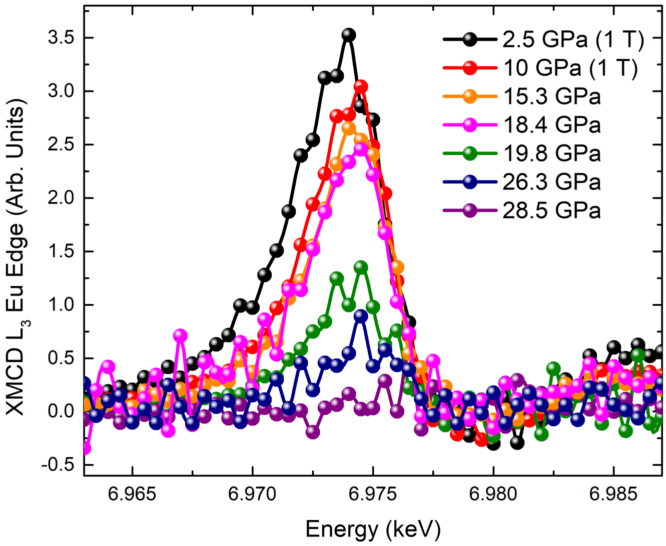

Figure 5.10: *High pressure XMCD measurements performed at 6 K and 4 T of applied magnetic field with exceptions for the 2.5 GPa and 10 GPa which were performed with 1 T of applied field. We can clearly see a diminishing signal for 18.4 GPa and above indicating that the ferromagnetic regime is modified.*

In Figure 5.11 we see the spectra for high pressure XANES at 6 K. The peak we see centered at 6.976 keV is in the same energy as the kapton tape measurements and corresponding to a regular Eu^{2+} absorption edge. Nonetheless for pressures in the range between 15.3 GPa and 28.5 GPa there is a small peak that starts to arise approximately 8 eV above the main absorption peak. This may occur for different reasons such as structural changes and electronic mixed valence states. For example a similar feature were observed in many compounds containing Eu at high pressures [77] [78] [79]. In their case, it was showed that Eu has a mixed valence state between $\text{Eu}^{2+}$and Eu^{3+} and that Eu^{3+} was responsible for the peak $\approx$ 8 eV above the Eu L_3 absorption edge. Therefore, considering the fact that structure of LnB_6 is sturdy, we infer that the peak in our data is coming from non-magnetic Eu^{3+} population growth. To further support our claim we performed simulations which are presented below.

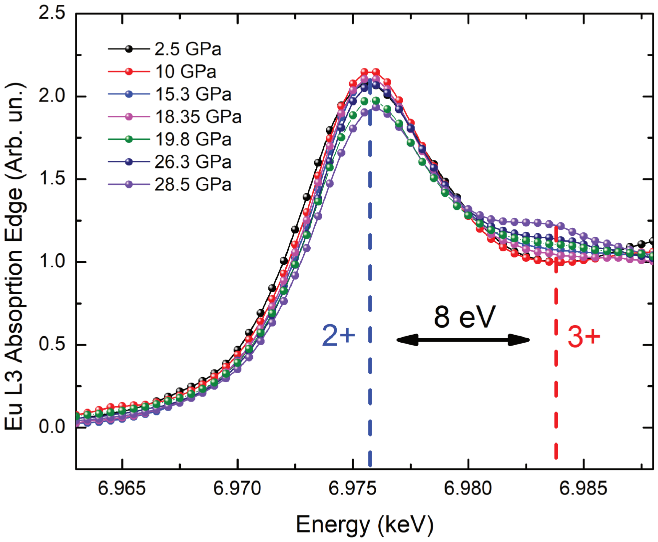

Figure 5.11: *High pressure XANES measurements for Eu* L_3 *absorption edge at 6 K temperatures. For all pressures there is a broad peak centered at 6.976 keV correspondent to* Eu^{2+} *absorption energy and for pressures from 15.3 GPa and above we start to see an peak approximately 8 eV above the main absorption peak corresponding to* Eu^{3+}.

For a quantitative analysis in the obtained XANES spectra we utilized the Finite Difference Method Near Edge Structure (FDMNES) software [80] to perform simulations and compare it to experimental data. Experimental data and simulated spectra are all plotted in Figure 5.12, where the top left graphic shows the above mentioned fit for 2.5 GPa spectra where a Eu^{2+} atom configuration was used in the EuB_6 crystal. The top right graphic shows experimental data for 10 GPa together with its respective simulated spectra, here agreement is not as good as previous but still acceptable considering it is an ab-inito calculation where the only change was contracting the lattice parameter. In the middle-left graphic we observe experimental data for 15 GPa, where the smaller peak $\approx$8 eV above the main absorption peak starts to be visible. In order to get better agreement between simulated and experimental data from this pressure and above, spectra using Eu^{3+} atoms were also simulated and added to the Eu^{2+} spectra, with a weight constant being adjusted to fit the peak height. Ab-initio calculated 3+ peaks were dislocated 8 eV above the usual Eu^{2+} absorption peak, for better fitting with experimental points. The weight constants for 2+ and 3+ spectra are indicated in the graphs and may be interpreted as an approximated value for divalent and trivalent Eu atoms population inside EuB_6. Therefore we see an increasing 3+ valence with applied pressure, this is notable for the middle-right graph were we see a 4% 3+ for 19.8 GPa, and even more evident in the bottom two graphs with 5% 3+ valence at 26.3 GPa and 9% for 28.5 GPa. Ultimately these values are approximations, since several experimental and analytical factors (e.g normalization) affect XANES strucuture's height it is difficult to estimate an precise error bar for obtained percentage values. What can be said is Eu^{3+} atoms quantity is increasing with applied pressure but at $\approx$ 30 GPa Eu^{2+} ion population is still dominant, this way there is still a possibility for antiferromagnetic ordering of the 4f momenta from the latter, making further experiments, such as SMS, necessary to resolve magnetic phases above 20

GPa.

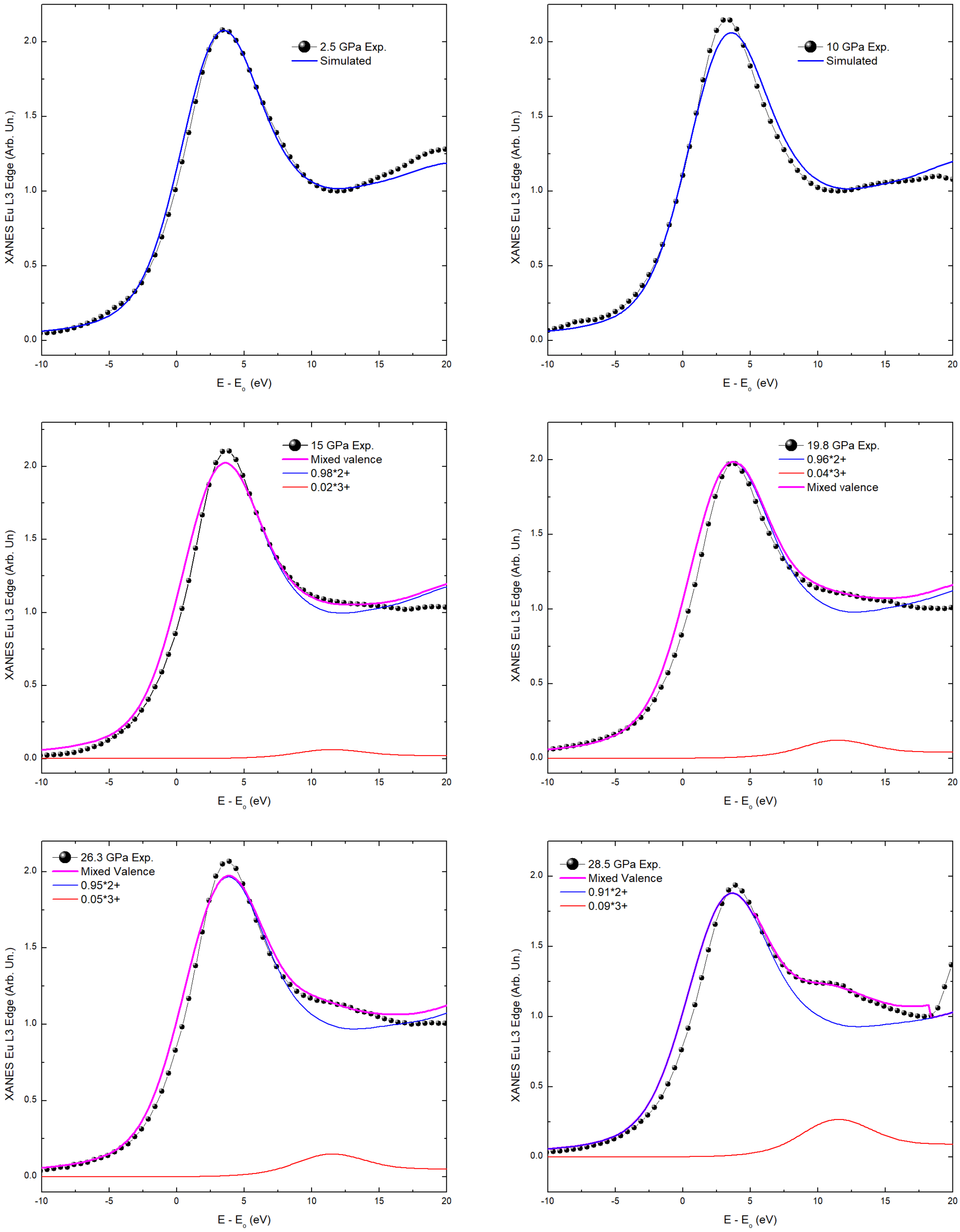

Figure 5.12: *Experimental XANES data together with their respective simulation for each pressure point on the experiment from top left to bottom right. From 15 GPa and above simulations on both 2+ and 3+ Eu were performed and showed in the graphs. Weighted addition give us the mixed valence curves and provide us approximated values for populations of each ion, where the 3+ valence atoms number increases with pressure, from 2% at 15 GPa to 9% at 28.5 GPa.*

5.2.2 Synchrotron Mössbauer Spectroscopy

Mössbauer spectroscopy probes nuclear isotopes absorption and remission of photon in order to obtain information on electronic and magnetic character of its surrounding, as more thorouglhy explained in Appendix II. In this subsection we present the results obtained for SMS measurements performed in order to resolve the magnetic state for EuB_6 above 20 GPa and further investigate mixed valence states. In Figure 5.13 we see spectra for EuB_6 powder (crushed single crystals) at 9 K temperature, here no external magnetic field is applied. We clearly observe quantum beats patterns in the curves, which are coming entirely from Eu-151 isotopes from EuB_6 since no references were used for this data set. More precisely, from 5 GPa to 18 GPa we observe a defined interference pattern due to quantum beats coming from magnetically split nuclei Zeeman levels $\frac{7}{2} \Rightarrow \frac{5}{2}$. As pressure goes up we see a slightly quantum beat frequency increase, suggesting that internal magnetic field along Eu nucleus is increasing in magnitude, which is in accord to the increase in T_c previously observed in [21] and also with the FM behavior observed in our XMCD data.

At 21 GPa a significant different SMS spectra is seen, where there is almost no quantum beating due to magnetic splitting of nuclear levels. This leads to the conclusion that at this pressure there is no magnetic field acting upon Eu isotopes nuclei. Therefore, by combining this result with our XMCD data we propose a paramagnetic phase for the compound above 21 GPa and below 9 K.

In the other hand at 24 GPa and 30 GPa we see the rise of quantum beats on the spectra, but they present a seemingly different pattern from those at lower pressures. Together with our XANES data we propose that these newly emerging quantum beats come from interference between light being remitted from a majority of Eu^{2+} and minority of Eu^{3+} ions. To further investigate such scenario we also perform measurements with reference compounds together with EuB_6 in order to better determine origins from the quantum beats at this high pressure range.

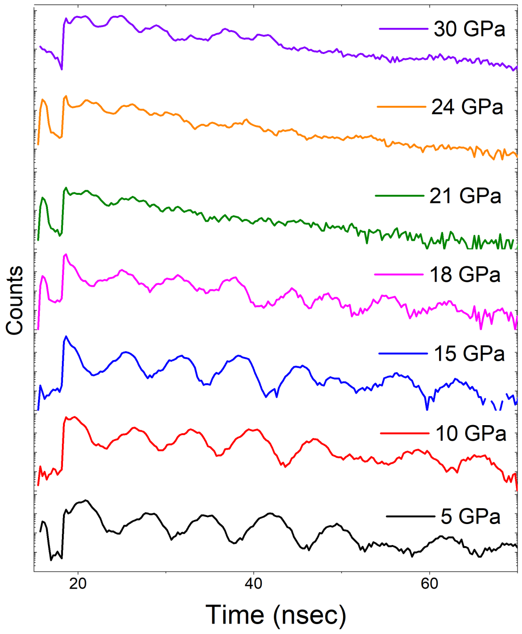

Figure 5.13: *EuB_6 synchrotron Mösssbauer spectroscopy (SMS) with no reference at 9 K for pressures indicated in the graph. We observe quantum beats interference due to magnetic splitting up to 18 GPa. At 21 GPa we do not see such interference pattern, showing a vanishing magnetic ordering. At 24 GPa and 30 GPa we see a quantum beating pattern which will be further investigate with references measurements, and may indicate with a divalent-trivalent Eu remitting quantum beat pattern.*

In Figure 5.14 we see SMS spectra for measurements with divalent EuS as reference compound placed in between our sample and the detector. From the raw data it is more difficult to draw immediate conclusion as previously since the beatings patterns we see in both graphs are a sum of contributions from reference-sample and magnetic splitting. What we can say is that we have magnetic quantum beats contribution for spectra below 20 GPa added to a exponential decay for EuS remitted light. Furthermore we see a clear difference for 30 GPa and 21 GPa spectra in, with no beating at 21 GPa and a few shy peaks between 20 nsec to 40 nsec at 30 GPa, meaning that the vast majority of Eu isotopes are divalent at this pressure range, indicating a mean valence close to 2+ when the proposed new phase is formed with increasing valence as pressure goes up. These SMS data are being analyzed with collaboration of Ercan Alp group from APS by using appropriate models which may provide us equivalent energy domain spectra and subsequently isomer shift, magnetic splitting and quadrupole splitting from our high pressure, low temperature EuB_6 experiments. These will allow us to fit intern magnetic field intensity and eventual amounts of trivalent Eu in our sample, which may corroborate even further with the proposed scenario drawn from XAS measurements results.

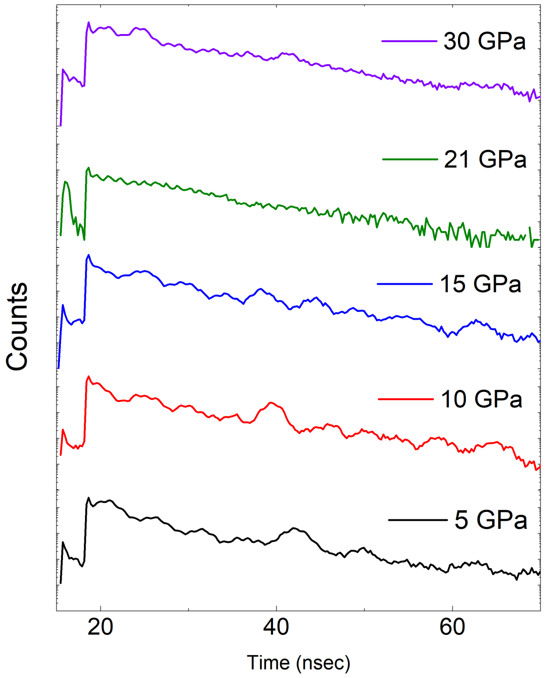

Figure 5.14: *EuB_6 SMS at 9 K with divalent EuS as reference. For 15 GPa and below we see a sum of magnetic splitting and reference intensity for the decay spectra. For 21 GPa and 30 GPa we see only a small trivalent-divalent interference with changing pattern as pressure goes up.*

Chapter 6

Conclusions

EuB_6 as the only ferromagnetic ordering rare earth hexaboride presents complex and interesting magnetic and transport phenomena, with evidence for formation of magnetic polarons and debates about its semi-metallic or semiconductor state. Recently it was proposed that topologically non-trivial structures may arise along band structure depending on the direction of alignment for the magnetic momenta, and it may be connected to a mixed valence state as also proposed for other family's compounds, such as SmB_6 and YbB_6.

By the means of our XAS measurements we clearly saw the formation of new phase for the EuB_6 compound above 20 GPa and below 9 K, which is well inside the temperature range of magnetic ordering at ambient pressure. This phase is evident by a significant drop in the XMCD signal and comes accompanied with the emergence and subsequent rise of a Eu^{3+} population as observed by XANES spectra. With the SMS spectra we were able to determine that this new phase is of a paramagnetic nature as indicated by the lack of quantum beats in the spectra for 21 GPa of applied pressure. Therefore by the combined data from our High Pressure X-Ray Spectroscopy measurements we propose a phase diagram for our compound as depicted in Figure 6.1. For the frontier between PM_1 (Paramagnetic 1) and SM (Semi-Metallic) phases below 17 GPa we used data from the Ref. [21] where they obtained Tc_1 and Tc_2 values by evaluating the maxima of $d\rho/dT$. For 20 GPa and above we see a new Paramagnetic phase with mixed valence (Eu^{2+} and Eu^{3+}) with an 2.09 average valence for 28.5 GPa. This provide us grounds for new interesting physical behavior to arise.

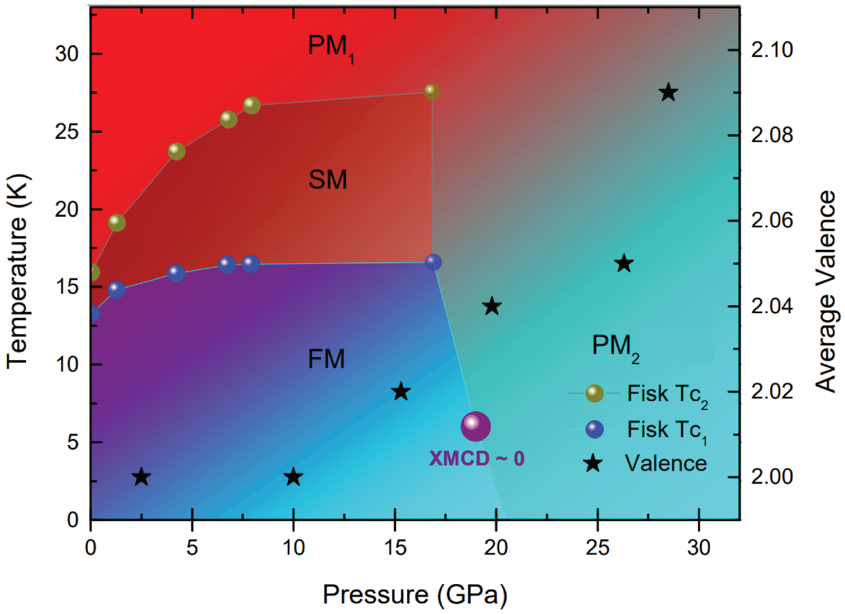

Figure 6.1: *Magnetic phase diagram for the EuB_6 built from our high pressure and SMS experiments combined with the previous transport data from [21]. PM_1 is for the paramagnetic phase observed at ambient pressure, SM is for the semi-metallic state between Tc_2 and Tc_1 and FM stands for the Ferromagnetic state below Tc_2. Above pressures of 20 GPa a new paramagnetic PM_1 phase arises.*

The point obtained for ≈ 17 GPa in [21] lacks graphs for the measurement, and lower pressure graphics show dρ/dT curves broadening. This way, the 17 GPa point may not be accurate. In the other hand our XAS and SMS pressure points have precision limited by the Ruby fluorescence scale and the averaging done for XANES and XMCD pressure data. Although this prevents us to pinpoint precisely frontiers between phases it is certain that a transition to a paramagnetic state occurs above 20 GPa for temperatures lower than 13 K, while for higher temperature frontiers also still need determination.

With the prospect of a RKKY dominant magnetic interaction proposed in [21], and the spin-split bands theorized in [19] associated with possible topologically non trivial band structures [20] a new EuB_6 phase comes with many probable scenarios to arise. As for, polaron formation is an interesting prospect for investigation under high pressures. One possible scenario is that high pressure suppresses polarons, theorized to form around charge carriers trapped near impurities aligning Eu^{2+} magnetic momenta [18]. Since our experiments show a decrease in Eu^{2+} population and high pressures can diminish impurity concentration along the crystal, these two ingredients necessary for polarons may suffer a lack under extreme conditions. To confirm if that is the case, transport experiments such as Hall and magneto-resistance can be performed in order to look for signature behaviors associated with magnetic polarons formation and existence [41] [45], while further expanding our understanding on charge carrier behavior for the compound.

As band structure is still unclear even for ambient pressure conditions and transport mechanisms still a matter of debate for the compound, physics underlying paramagnetic transition at high pressures using spectroscopy data is hard to define. In the other hand, our results point a definitive direction where new physics can be encountered and put under scrutiny either experimentally or theoretically, which can further clarify our understanding for the hexaborides family.

Bibliography

[1] Neupane, M. *et al.* Surface electronic structure of the topological kondo-insulator candidate correlated electron system $\mathrm{SmB_6}$. *Nature communications* **4**, 1–7 (2013).

[2] Thomas, S. M. *et al.* Quantum oscillations in flux-grown $\mathrm{SmB_6}$ with embedded aluminum. *Physical review letters* **122**, 166401 (2019).

[3] Gesley, M. & Swanson, L. A determination of the low work function planes of $\mathrm{LaB_6}$. *Surface science* **146**, 583–599 (1984).

[4] Yoshimori, A. & Kasai, H. Theory of dense kondo system. *Journal of magnetism and magnetic materials* **31**, 475–476 (1983).

[5] Foroozani, N. *et al.* Suppression of dense kondo state in $\mathrm{CeB_6}$ under pressure. *Physica B: Condensed Matter* **457**, 12–16 (2015).

[6] McCarthy, C. & Tompson, C. Magnetic structure of $\mathrm{NdB_6}$. *Journal of Physics and Chemistry of Solids* **41**, 1319–1321 (1980).

[7] Ali, N. & Woods, S. Transport properties of GdB_6 and DyB_6. *Journal of low temperature physics* **56**, 575–584 (1984).

[8] Takahashi, K. *et al.* Magnetic and structural phase transition in heavy rare-earth compound DyB_6. *Physica B: Condensed Matter* **241**, 696–698 (1997).

[9] MAR, R. W. Conditions for formation of ErB_6. *Journal of the American Ceramic Society* **56**, 275–278 (1973).

[10] Kasaya, M., Tarascon, J., Etourneau, J. & Hagenmuller, P. Study of carbon-substituted EuB_6. *Materials Research Bulletin* **13**, 751–756 (1978).

[11] Süllow, S. *et al.* Structure and magnetic order of EuB_6. *Physical Review B* **57**, 5860 (1998).

[12] B.T.Matthias. Polaron ferromagnetism of EuB_6. *Physics Letters A* **27**, 511 (1968).

[13] Sivananda, D. J. *et al.* Magneto-optical imaging of stepwise magnetic domain disintegration at characteristic temperatures in EuB_6. *Physical Review Materials* **2**, 113404 (2018).

[14] Pohlit, M. *et al.* Evidence for ferromagnetic clusters in the colossal-magnetoresistance material EuB_6. *Physical review letters* **120**, 257201 (2018).

[15] Denlinger, J. *et al.* Bulk band gaps in divalent hexaborides. *Physical review letters* **89**, 157601 (2002).

[16] D. Denlinger, J. *et al.* Absence of X-point band overlap in divalent hexaborides and variability of the surface chemical potential. *Journal of the Physical Society of Japan* **71**, 1–4 (2002).

[17] Guy, C., Von Molnar, S., Etourneau, J. & Fisk, Z. Charge transport and pressure dependence of tc of single crystal, ferromagnetic EuB_6. *Solid State Communications* **33**, 1055–1058 (1980).

[18] Nyhus, P. *et al.* Spectroscopic study of bound magnetic polaron formation and the metal-semiconductor transition in EuB_6. *Physical Review B* **56**, 2717 (1997).

[19] Kuneš, J. & Pickett, W. Kondo and anti-kondo coupling to local moments in EuB_6. *Physical Review B* **69**, 165111 (2004).

[20] Nie, S. *et al.* Magnetic semimetals and quantized anomalous hall effect in EuB_6. *Physical Review Letters* **124**, 076403 (2020).

[21] Cooley, J., Aronson, M., Sarrao, J. & Fisk, Z. High pressures and ferromagnetic order in EuB_6. *Physical Review B* **56**, 14541 (1997).

[22] Kroha, J. Interplay of kondo effect and rkky interaction. *arXiv preprint arXiv:1710.00192* (2017).

[23] Weisstein, E. W. Topology. *MathWorld -A Wolfram Web Resource. http://mathworld.wolfram.com/Topology.html* (2017).

[24] Qi, X.-L. & Zhang, S.-C. Topological insulators and superconductors. *Reviews of Modern Physics* **83**, 1057 (2011).

[25] Hasan, M. Z. & Kane, C. L. Colloquium: topological insulators. *Reviews of modern physics* **82**, 3045 (2010).

[26] Dzero, M., Sun, K., Galitski, V. & Coleman, P. Topological kondo insulators. *Physical review letters* **104**, 106408 (2010).

[27] Fruchart, M. & Carpentier, D. An introduction to topological insulators. *Comptes Rendus Physique* **14**, 779–815 (2013).

[28] Fang, C., Weng, H., Dai, X. & Fang, Z. Topological nodal line semimetals. *Chinese Physics B* **25**, 117106 (2016).

[29] Yan, B. & Felser, C. Topological materials: Weyl semimetals. *Annual Review of Condensed Matter Physics* **8**, 337–354 (2017).

[30] Arnold, F. *et al.* Negative magnetoresistance without well-defined chirality in the Weyl semimetal TaP. *Nature communications* **7**, 1–7 (2016).

[31] Shekhar, C. *et al.* Extremely large magnetoresistance and ultrahigh mobility in the topological Weyl semimetal candidate NbP. *Nature Physics* **11**, 645–649 (2015).

[32] Phelan, W. *et al.* On the chemistry and physical properties of flux and floating zone grown SmB_6 single crystals. *Scientific reports* **6**, 20860 (2016).

[33] Canfield, P. C. & Fisk, Z. Growth of single crystals from metallic fluxes. *Philosophical magazine B* **65**, 1117–1123 (1992).

[34] Cahill, J. T. & Graeve, O. A. Hexaborides: a review of structure, synthesis and processing. *Journal of Materials Research and Technology* **8**, 6321–6335 (2019).

[35] Guy, C., Von Molnar, S., Etourneau, J. & Fisk, Z. Charge transport and pressure dependence of tc of single crystal, ferromagnetic EuB_6. *Solid State Communications* **33**, 1055–1058 (1980).

[36] Griffiths, D. J. Introduction to electrodynamics (2005).

[37] Stöhr, J. & Siegmann, H. C. Magnetism. *Solid-State Sciences. Springer, Berlin, Heidelberg* **5** (2006).

[38] Ashcroft, N. W. & Mermin, N. D. Solid state physics,. *Pacific Grove: Brooks/Cole* 29–55 (1976).

[39] Süllow, S. *et al.* Metallization and magnetic order in EuB_6. *Physical Review B* **62**, 11626 (2000).

[40] Callister, W. D. & Rethwisch, D. G. *Materials science and engineering: an introduction*, vol. 9 (Wiley New York, 2018).

[41] Calderón, M., Wegener, L. & Littlewood, P. Evaluation of evidence for magnetic polarons in EuB_6. *Physical Review B* **70**, 092408 (2004).

[42] von Molnár, S. & Stampe, P. Magnetic polarons handbook of magnetism and advanced magnetic materials, spintronics and magnetoelectronics vol 5, ed H kronmüller and S Parkin (2007).

[43] Wigger, G., Monnier, R., Ott, H., Young, D. & Fisk, Z. Electronic transport in EuB_6. *Physical Review B* **69**, 125118 (2004).

[44] Zhang, X., von Molnár, S., Fisk, Z. & Xiong, P. Spin-dependent electronic states of the ferromagnetic semimetal EuB_6. *Physical review letters* **100**, 167001 (2008).

[45] Zhang, X., Yu, L., von Molnár, S., Fisk, Z. & Xiong, P. Nonlinear Hall Effect as a Signature of Electronic Phase Separation in the Semimetallic Ferromagnet EuB_6. *Physical review letters* **103**, 106602 (2009).

[46] Hikami, S., Larkin, A. I. & Nagaoka, Y. Spin-orbit interaction and magnetoresistance in the two dimensional random system. *Progress of Theoretical Physics* **63**, 707–710 (1980).

[47] Goodrich, R. *et al.* Fermi surface of ferromagnetic EuB_6. *Physical Review B* **58**, 14896 (1998).

[48] Urbano, R. *et al.* Magnetic polaron and Fermi surface effects in the spin-flip scattering of EuB_6. *Physical Review B* **70**, 140401 (2004).

[49] De Groot, F. X-ray absorption and dichroism of transition metals and their compounds. *Journal of Electron Spectroscopy and Related Phenomena* **67**, 529–622 (1994).

[50] Poldi, E. H. T. *et al.* A versatile X-ray phase retarder for lock-in XMCD measurements. *Journal of Synchrotron Radiation* **27** (2020).

[51] Cezar, J., Vicentin, F. & Tolentino, H. Aplicação de técnicas de absorção de raios x no estudo de materiais magnéticos. *Revista Brasileira de Ensino de Física* **22** (2000).

[52] Grandjean, F. & Long, G. J. Mössbauer spectroscopy of europium-containing compounds. In *Mössbauer Spectroscopy Applied to Inorganic Chemistry*, 513–597 (Springer, 1989).

[53] Bauminger, E., Kalvius, G. & Nowik, I. Mössbauer isomer shifts. *North-Holland, Amsterdam* **661** (1978).

[54] Greenwood, N. N. *Mössbauer spectroscopy* (Springer Science & Business Media, 2012).

[55] Kunii, S., Kaneda, T., Kasuya, T. & Fujioka, M. Mossbauer effect studies of EuB_6 in an applied magnetic field. *CYRIC annual report* 64–69 (1986).

[56] Hastings, J., Siddons, D., Van Bürck, U., Hollatz, R. & Bergmann, U. Mössbauer spectroscopy using synchrotron radiation. *Physical review letters* **66**, 770 (1991).

[57] Strohm, C., Van der Linden, P. & Rüffer, R. Nuclear forward scattering of synchrotron radiation in pulsed high magnetic fields. *Physical review letters* **104**, 087601 (2010).

[58] Siddons, D. *et al.* Experimental techniques for the study of nuclear Bragg scattering in systems containing ^{57}fe. *Review of Scientific Instruments* **60**, 1649–1654 (1989).

[59] Leupold, O. Hyperfine spectroscopy with nuclear resonant scattering of synchrotron radiation. In *Mössbauer Spectroscopy*, 21–32 (Springer, 2003).

[60] Nasu, S. High-pressure mössbauer spectroscopy with nuclear forward scattering of synchrotron radiation. *International Journal of High Pressure Research* **14**, 405–412 (1996).

[61] NobelPrize.org. The nobel prize in physics 1946. *Nobel Media AB 2020. Tue. 15 Sep 2020 https://www.nobelprize.org/prizes/physics/1946/summary* (2020).

[62] Bridgman, P. W. General survey of certain results in the field of high-pressure physics. *Nobel Lecture, Dec* **11** (1946).

[63] Bassett, W. A. Diamond anvil cell, 50th birthday. *High Pressure Research* **29**, 163–186 (2009).

[64] Banerjee, A. *et al.* Ultralarge elastic deformation of nanoscale diamond. *Science* **360**, 300–302 (2018).

[65] Nicklas, M. Pressure probes. In *Strongly Correlated Systems*, 173–204 (Springer, 2015).

[66] Syassen, K. Ruby under pressure. *High Pressure Research* **28**, 75–126 (2008).

[67] Chijioke, A. D., Nellis, W., Soldatov, A. & Silvera, I. F. The ruby pressure standard to 150 gpa. *Journal of Applied Physics* **98**, 114905 (2005).

[68] Gluskin, E. *et al.* An electromagnetic helical undulator for polarized x-rays. In *AIP Conference Proceedings*, vol. 521, 344–347 (American Institute of Physics, 2000).

[69] Gluskin, E. Aps insertion devices: Recent developments and results. *Journal of synchrotron radiation* **5**, 189–195 (1998).

[70] Freeland, J. *et al.* A unique polarized x-ray facility at the advanced photon source. *Review of scientific instruments* **73**, 1408–1410 (2002).

[71] Bi, W. *et al.* Nuclear resonant inelastic x-ray scattering at high pressure and low temperature. *Journal of Synchrotron Radiation* **22**, 760–765 (2015).

[72] Toellner, T. *et al.* A cryogenically stabilized meV-monochromator for hard X-rays. *Journal of synchrotron radiation* **13**, 211–215 (2006).

[73] Mooney, T., Toellner, T., Sturhahn, W., Alp, E. & Shastri, S. High-resolution, large-angular-acceptance monochromator for hard x rays. *Nuclear Instruments and Methods in Physics Research Section A: Accelerators, Spectrometers, Detectors and Associated Equipment* **347**, 348–351 (1994).

[74] Rivers, M. *et al.* The compres/gsecars gas-loading system for diamond anvil cells at the advanced photon source. *High Pressure Research* **28**, 273–292 (2008).

[75] Klotz, S., Chervin, J., Munsch, P. & Le Marchand, G. Hydrostatic limits of 11 pressure transmitting media. *Journal of Physics D: Applied Physics* **42**, 075413 (2009).

[76] Fujita, T., Suzuki, M. & Ishikawa, Y. Specific heat of EuB_6. *Solid State Communications* **33**, 947–950 (1980).

[77] Souza-Neto, N. *et al.* Reentrant valence transition in EuO at high pressures: beyond the bond-valence model. *Physical review letters* **109**, 026403 (2012).

[78] Menushenkov, A. *et al.* Driving the europium valence state in $EuCo_2As_2$ by external and internal impact. *Journal of Superconductivity and Novel Magnetism* **30**, 75–78 (2017).

[79] Sarkar, S., Subbarao, U., Joseph, B. & Peter, S. C. Mixed valence and metamagnetism in a metal flux grown compound $Eu_2Pt_3Si_5$. *Journal of Solid State Chemistry* **225**, 181–186 (2015).

[80] Bunău, O. & Joly, Y. Self-consistent aspects of x-ray absorption calculations. *Journal of Physics: Condensed Matter* **21**, 345501 (2009).

[81] Borland, M. *et al.* APS storage ring parameters. *Advanced Photon Source* (2010).

[82] Farias, R. *et al.* Commissioning of the LNLS 500-MeV booster synchrotron. In *PACS2001. Proceedings of the 2001 Particle Accelerator Conference (Cat. No. 01CH37268)*, vol. 4, 2701–2703 (IEEE, 2001).

[83] Liu, L., Milas, N., Mukai, A. H., Resende, X. R. & de Sá, F. H. The Sirius project. *Journal of synchrotron radiation* **21**, 904–911 (2014).

[84] Touschek, B. The physics of electron storage rings. *Proceedings of the International School of physics Enrico Fermi, Course No. 46 ed.* **1**, 257–411 (1971).

[85] Jackson, J. D. *Classical electrodynamics* (John Wiley & Sons, 2007).

[86] Dronsfield, A. & Adetunji, J. The beginnings of mössbauer spectroscopy. *Website: Royal Society of Chemistry* (2002).

[87] NobelPrize.org. The nobel prize in physics 1961. *Nobel Media AB 2020. Tue. 15 Sep 2020 https://www.nobelprize.org/prizes/physics/1961/summary/* (2020).

[88] May, L. *An introduction to Mössbauer spectroscopy* (Springer Science & Business Media, 2012).

[89] Mössbauer, R. The discovery of the Mössbauer effect. *Hyperfine Interactions* **126** (2000).

[90] Herber, R. Introduction to mossbauer spectroscopy. *Journal of Chemical Education* **42**, 180 (1965).

[91] Dickson, D. P. & Berry, F. J. *Mössbauer spectroscopy* (Cambridge University Press, 2005).

[92] Jie, D. *et al.* Elastic properties and electronic structures of lanthanide hexaborides. *Chinese Physics B* **24**, 096201 (2015).

Appendix I

Synchrotron Light

In this appendix we briefly explain the functioning and few concepts behind synchrotrons, the radiation they create, few applications and advantages which were relevant for this work.

Most synchrotron facilities utilize electrons as charged particles because of its low mass and relatively easy attainment. There are three main apparatus that create and handle these electrons in a synchrotron: a linear accelerator (LINAC), a booster and the storage ring. Firstly at the LINAC, electrons are usually obtained via thermo-ionic process by heating a tungsten resistance and subsequently accelerated in a linear vacuum-tube path via several radio-frequency cavities which apply electric field to the charges in a resonant manner, enhancing performance and saving energy. After this initial acceleration, when electrons already have built up a decent amount of speed they are inserted into the second stage which is the booster. At this point electrons are trapped in a closed loop of vacuum tubes where electric fields accelerate them, boosting their speed, while strategically spaced electromagnets bend their trajectories into the path. It is evident that basic physics for most processes described until now are simply explained by the Lorentz force:

$$\vec{F} = q\left(\vec{E} + \vec{v} \times \vec{B}\right) \tag{6.1}$$

where $\vec{F}$ is the force acting in a charge q with velocity $\vec{v}$ submitted to an electric field $\vec{E}$ and a magnetic field $\vec{B}$. But since energy acquired by electrons during the acceleration phase are quite high, their speed comes close to the speed of light c, so one must be aware of relativistic effects and use

$$\frac{d\vec{p}}{dt} = q\left(\vec{E} + \vec{v} \times \vec{B}\right) \tag{6.2}$$

where $\vec{p} = \gamma m_o \vec{v}$ is the relativistic momentum, with m_o being the particle (electron in our case) rest mass and

$$\gamma = \frac{1}{\sqrt{1 - \frac{v^2}{c^2}}} = \frac{1}{\sqrt{1 - \beta^2}} \tag{6.3}$$

is the Lorentz factor. In fact, electrons come out the booster with speed comparable to that of the light, meaning that $v \approx c$ and $\beta \to 1$. Given that, instead of stating electron's final speed machines are specified by their final kinetic energy

$$K_E = mc^2 - m_o c^2 \text{ where } m = \gamma m_o \tag{6.4}$$

Some examples of energy together with calculated γ for few synchrotrons are given at Table 6.1.

Synchrotron	Energy (GeV)	γ
UVX	1.37	2681.726
APS	7.0	13698.139
SIRIUS	3.0	5870.854

Table 6.1: Few synchrotrons with their respective energies and gamma factors retrieved from [81] [82] [83]

Before going forward in explaining the third and final stage: the storage ring and produced radiation, it is necessary to mention that electrons inserted from the booster form packed electron clouds inside the storage ring, which are called bunches. These entities have a finite dimensions and fluctuate in shape and energy around an idealized point charge rotating in a perfect orbit, which notably effects optical properties in the generated radiation, if one electron in the bunch drifts away enough from this orbit he will most likely be scattered away and be lost in a optical element or vacuum tube barrier. For simplicity we neglect these effects and assume that bunches act as perfect point charges while proposing an example where a perfectly circular storage ring support six equally radially spaced bunch ”slots” as picture in Figure 6.2. The manner that these slots are occupied; the operation mode, affects how radiation will be seen in the experimental stations, which ranges from a quasi-continuum flux of light when every bunch is filled to periodically spaced peaks when electrons are in a single bunch. This is important because some spectroscopy techniques such as

XANES and XMCD, which are explained later, benefit from a continuum flux configuration, while others, like synchrotron Mössbauer spectroscopy requires spaced peaks of radiation to be performed. Some bunch-bunch interactions, which we also neglect, may give rise to important phenomena like coherent synchrotron radiation. More details on basics of electron bunches and storage rings can be found in [84].

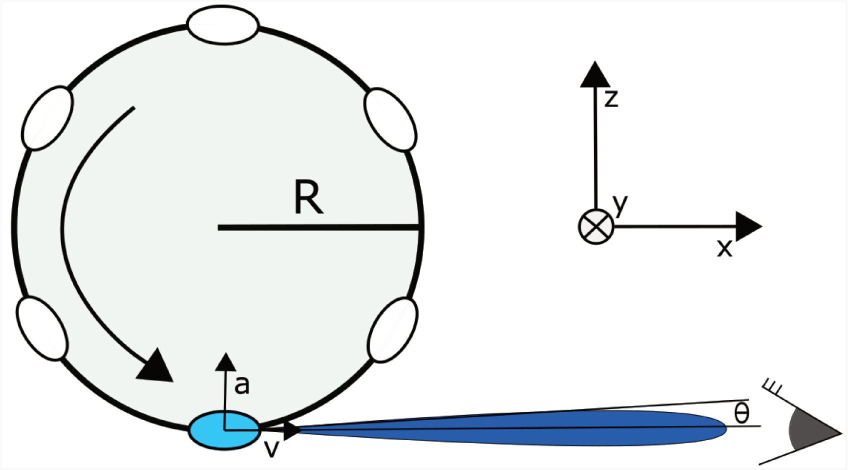

Figure 6.2: *Simplified storage ring emitting synchrotron light scheme, the coordinated axis is a reference for the text. The circle of radius R is a perfect orbit for the electron bunch slots represented as small ellipses. In this example only the blue colored bunch slot is filled and emitting radiation represented as the dark blue elongated globule. The observer detects radiation with this small angular distribution* $\theta \propto \gamma$ *in a vast range of frequencies as explained in the text.*

Similar to the booster, a storage ring is composed from vacuum tubes where electrons orbit around, but now optical elements such as magnetic dipoles, quadrupoles or octupoles, together with RF cavities are present to focus and accelerate electrons. It is well established by the electrodynamics theory that an accelerated charge emits radiation, the Power emitted by an point charge may be given by the famous Larmor's formula

$$P = \frac{\mu_0 q^2 a^2}{6\pi c} \tag{6.5}$$

which is valid for non-relativistic motion. But as we saw, electrons inside the storage ring orbit with velocities near that of the light, so we may use the Liénard's equation for generalized radiation power for relativistic motion of charged particles

$$P = \frac{\mu_0 q^2 \gamma^6}{6\pi c} \left(a^2 - \left| \frac{\vec{v} \times \vec{a}}{c} \right| \right) \tag{6.6}$$

When the electrons passes trough a magnetic dipole field inside the storage rings it suffers an acceleration perpendicular to its velocity (as expected for a circular orbit), we can arbitraly choose the acceleration to be pointing positively to the z axis while velocity points positively to the x axis, in this case the total power irradiated is given by [36]

$$P = \frac{\mu_0 q^2 \gamma^4}{6\pi c} \tag{6.7}$$

Not only the radiation is extremely powerful if compared to non-relativistic moving charges due to the γ^4 factor but it has also directional concentration in a narrow beam that resembles an elongated water droplet escaping tangentially from the electrons orbit as can be seen in Figure 6.3 where we also draw a relevant coordinate axis. It can be shown by calculating the power distribution via Poynting's vector that this angular Power distribution has the form [85]:

$$\frac{dP}{d\Omega} \approx \frac{2e^2\gamma^6a^2}{\pi c^3\left(1+\gamma^2\theta^2\right)^3}\left[1-\frac{4\gamma^2\theta^2\cos^2\phi}{\left(1+\gamma^2\theta^2\right)^2}\right] \tag{6.8}$$

where Ω is the solid angle (θ and ϕ come from the usual radial coordinated system) and approximations for $\theta \ll 1$ were used, which is acceptable for $\gamma \gg 1$. Also, an easily understandable result comes from taking the root mean square for the distribution of θ:

$$\langle\theta^2\rangle^{1/2} = \frac{1}{\gamma} \tag{6.9}$$

meaning that the higher gamma factor (or electron's energy) is, the smaller angular distribution will be. Furthermore the light is strongly linearly polarized horizontally in the electron's orbital plane, which is important for experiments that depend on light polarization such as XMCD. Since this radiation is coming out electrons changing direction due to magnetic dipole field it is sometimes refereed as "dipole radiation" and it comes by the price of electron's kinetic energy, therefore RF cavities in the storage rings are used to maintain electrons at nearly constant speed.

Another important feature of the outgoing radiation coming from the synchrotron is irradiated power in function of frequency. Suppose we have a fixed observer at one tangent line from the circular electron's storage ring of radius R orbit, inside an experimental station. The angular frequency for a point charge inside this ring will be

$$\omega_o = \frac{c}{R} \tag{6.10}$$

where we assumed the electrons velocity $v \approx c$. The observer will see a burst of synchrotron light once per period during the charge's passage through a small arc d of the orbit where electron's velocity points towards him. Neglecting the curvature ($d \ll R$), and assuming burst width of γ^{-1} we have

$$d = \frac{R}{\gamma} \tag{6.11}$$

which the electron travels in

$$\Delta t = \frac{R}{\gamma v} \approx \frac{R}{\gamma c} \tag{6.12}$$

the radiation burst length is then calculated to be

$$B_L = \frac{R}{2\gamma^3} \tag{6.13}$$

a qualitative argument guides us in a direction that a compressed wave train in real space would have a large distribution in the frequency space if a Fourier transform were to be made. In fact, such Fourier analysis was performed in detail by Jackson [85] and qualitative results may be resumed as follow: there is a critical frequency (as calcualted for for $\theta = 0$, but it works for the small angular radiation distribution mentioned above)

$$\omega_c = \frac{3}{2}\gamma^3\frac{c}{R} \tag{6.14}$$

for which emitted light starts to decay and become negligible. Additionally it is obtained, for limiting cases, how radiation intensity behaves in function of angular frequency, if $\omega \ll \omega_c$ we have

$$\frac{dI}{d\omega} \propto \frac{e^2}{c}\left(\frac{\omega R}{c}\right)^{1/3} \tag{6.15}$$

and for $\omega \gg \omega_c$

$$\frac{dI}{d\omega} \approx \sqrt{3\pi/2}\frac{e^2}{c}\gamma\left(\frac{\omega}{\omega_c}\right)^{1/2} e^{-\omega/\omega_c} \tag{6.16}$$

this gives us an idea that for low frequencies the light intensity grows with $\omega^{1/3}$ until it nears the neighborhoods of ω_c and then decays exponentially. A more accurate result for all frequencies is given by

$$\frac{dI}{d\omega} = \sqrt{3}\frac{e^2}{c}\gamma\frac{\omega}{\omega_c}\int_{\omega/\omega_c}^{\infty} K_{5/3}(x)dx \tag{6.17}$$

where $K_\alpha(x)$ is the modified Bessel function of second kind. Graphics for this equation and previous approximations can be seen in Figure 6.3 where Sirius parameters were utilized in calculations. Even though the deviation from approximations is quite noticeable near ω_c the curves are qualitatively acceptable. We see appreciable radiation up to keV X-rays, which is expected for this electron energy range. Nevertheless, this simple picture completely underestimate the radiation range production in this specific case since it does not take into account special magnet placement along Sirius storage ring. This alone pushes critical frequency up to $\approx$ 12 keV and special insertion devices can further increase X-ray intensity as we will see next.

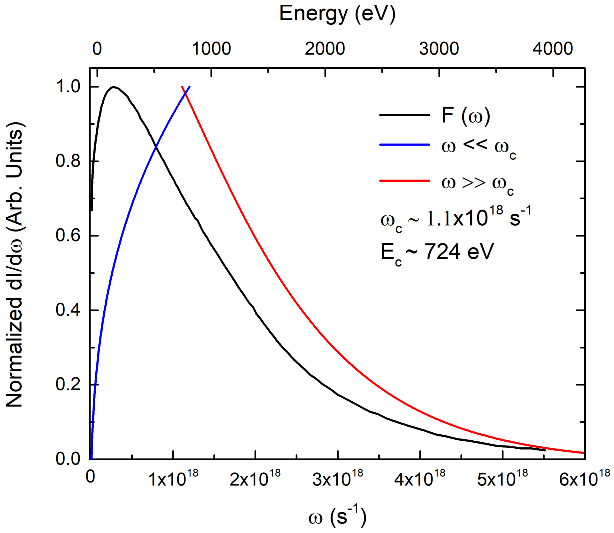

Figure 6.3: *Figure showing normalized synchrotron light spectra for two approximations from Equations 6.15, 6.16 in blue and red, respectively, and proper integration of Equation 6.17 in black. The approximate curves do not quantitatively agree with the spectra near ω_c but provide good qualitative agreement in other regions. The critical frequency was obtained through Equation 6.14 utilizing Sirius synchrotron parameters from [83]. In the top X axis we see an photon energy scale ($E = \hbar\omega$) for better insight on intensity distribution. The critical frequency, and consequently frequency distribution range, is severely underestimated in this case for reasons presented in the text.*

As we saw dipole radiation is a powerful tool and have significant intensities for wavelengths in keV X-ray range. This intensity (or photon flux, equivalently) may be further amplified by utilizing electron optical elements such as wigglers or undulators. These insertion devices consist in magnets separated by few centimeters that create periodic displacement in electrons transversely to their orbital plane (y direction, in our example), which may be given by

$$y \approx a \sin(2\pi x/\lambda_o) \tag{6.18}$$

with λ_o being the magnet period and a a constant dependent on magnetic field strength. An important parameter is the maximum angular deviation

$$\psi_0 = \left(\frac{dy}{dx}\right)_{x=0} = \frac{2\pi a}{\lambda_o} \tag{6.19}$$

and is used to define the difference between wigglers and undulators. As we saw the angular distribution for synchrotron dipole radiation is in the order of γ^{-1}, if $\psi_0 \gg \gamma^{-1}$ the insertion device is called a wiggler, if $\psi_0 \ll \gamma^{-1}$ we have an undulator. This transversal to the orbit acceleration also causes electrons to irradiate, enhancing the flux of photons coming out the storage ring. For a wiggler the route deviation from the orbit is much higher than the beam-light size, which is seen by an observer as several re-emissions with frequency

$$f = c/\lambda_o \tag{6.20}$$

this enhances dipole radiation emission in a smooth manner, increasing intensity proportionally to numbers of magnet periods in the wiggler acting as ”mini-synchrotron” with fundamental frequency

$$\Omega_o = \frac{2\pi c \psi_0}{\lambda_o} \tag{6.21}$$

and critical frequency

$$\Omega_c \propto \gamma^3 \frac{2\pi c}{\lambda_o \psi_o} \tag{6.22}$$

resulting in an observed shift for the storage ring critical frequency as well. For undulators the vertical electron shift is much smaller than the beam size, and the observer detects an coherent superposition from the oscillations coming from the magnets. This creates a sharp peak of radiation in a frequency proportional to the separation between magnets, which considering the relativistic Doppler effect, is calculated to be

$$\omega = \frac{2\gamma^2}{1+\gamma^2\theta^2}\left(\frac{2\pi c}{\lambda_o}\right) \tag{6.23}$$

with θ being the same as for the angular radiation distribution. Experimentally there is a range of frequencies around ω created by an undulator, since this theoretical value would only be attainable if the number of magnetic periods in the device was infinite. As an example, detailed calculations for the Sirius storage ring which take into account several factors neglected in our previous explanation, as bunch size and energy spread, special magnet placement among others[83] results in a spectral distribution as showed in Figure 6.4. We clearly see the difference between plain storage ring radiation in the bottom curve to wiggler and undulators generated light in the curves above. In conclusion these devices can be used to obtain relevant amount of photons even in high energy X-ray range for synchrotron with lower gamma factors, or enhance values even further for the most energetic storage rings.

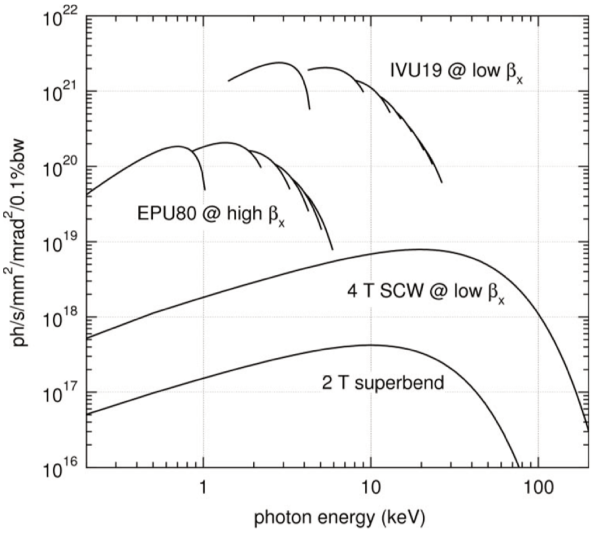

Figure 6.4: *Photon flux per energy as calculated for Sirius storage ring. The lowest curve represents the "dipole radiation" for the special configuration with a 2 Tesla superbend magnet. The following curve represents the theoretical flux for a 4 Tesla magnet wiggler, which is very similar to the first curve but with more photon flux at all energies and shifted* ω_c. *The uppermost segments represent radiation coming from Undulators with two different magnet periods, we see great amount of flux for a limited energy range as explained in the text. Figure reproduced from [83] from where more details on calculations can be found.*

Finally we briefly discuss the usual optical device encountered by photons outside a storage ring: the monochromator. As we saw synchrotron light is poly-chromatic and ranges from visible light to highly energetic X-rays. If one desires to have a monochromatic X-ray beam it needs to select and separate it from the remaining emitted synchrotron radiation which can be achieved by single crystal diffraction. In a simplified picture we can use the Bragg's diffraction law which states that light reflected from two crystallographic planes separated by a distance d will suffer constructive interference when

$$n\lambda = 2d \sin\theta \tag{6.24}$$

where n is a natural number, λ is the wavelength and θ is the angle between incident light and reflection planes. So, for a fixed d on can select λ of a polychromatic X-Ray by tuning the angle θ, which is very handy for spectroscopy measurements where tuning photon energy ($E = hc/\lambda$) is necessary. One problem that arises immediately comes from the fact that a crystal can also reflect higher harmonics of the desired wavelength, which may affect counts further ahead in the detectors. To reduce such problems or enhance photon energy precision, several apparatus are employed such as slits, harmonic filters or nested monochromatic crystal mirrors.

Appendix II

Mössbauer Spectroscopy

Mössbauer Spectroscopy named after Rudolf Ludwig Mössbauer who, in 1953, continued and expanded work on radiation emission and absorption previously developed by Philip Moon and Karl Malmfors [86]. The technique bears his name due to groundbreaking observations that ultimately awarded him the Physics Nobel Prize of 1961 [87]. It is important to note that his work was dealing with radiation emitted by atomic nuclei which is denominated as gamma-rays (γ-rays). Such radiation is composed of photons that may have same energy as X-ray mentioned earlier, but the change in nomenclature is solely due to the light source. Many elements in the periodic table present naturally occurring radioactive isotopes which population decay by 50% (by emitting α β or γ radiation) in periods denominated half-life (λ-life). In similar fashion to electronic states, these radioactive atomic nuclei also present excited states which tend to decay to their ground sates by emitting the previously mentioned γ-rays (photons). Such excited states are due to spatial distribution of sub-atomic particles.

The way how this radiation is emitted is of the utter importance for Mössbauer physics.

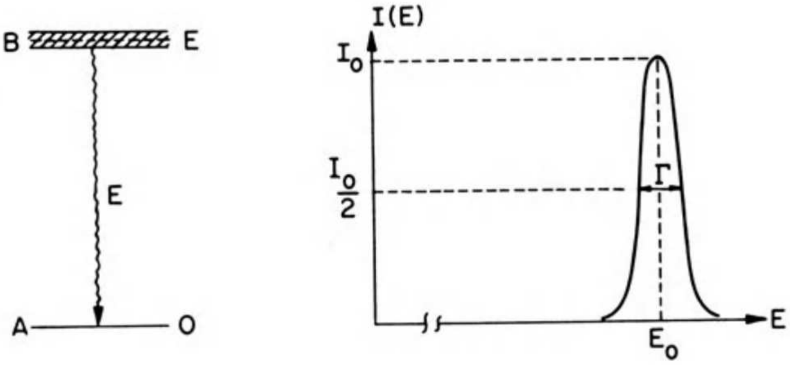

Figure 6.5: *Image representing the decay from an excited state B to a ground state A via γ ray photo emission. The graph in the right shows energy distribution width in the excited state with half-height Γ, which will generate a Lorentzian energy distribution for the emitted photon. Image reproduced from [88].*

There are two features for nucleic emitted radiation that underlay Mössbauer physics: well defined energy, (sharp spectroscopy line) and emitting atom recoil due to high energetic photon propulsion. Suppose that a excited state has a mean life time τ, utilizing the fact derived from the well known uncertainty principle:

$$\Delta E \Delta t \geq \hbar \tag{6.25}$$

if Γ is the excited state energy distribution half-weight we can write from 6.25 that

$$\Gamma = \frac{\hbar}{\tau} \tag{6.26}$$

and it can be shown [88] that photon energy emission associated to the decay from excited to ground state has a Lorentzian energy intensity distribution such as

$$I(E) = C\frac{\Gamma}{2\pi}\frac{1}{(E-E_0)^2+(\Gamma/2)^2} \tag{6.27}$$

where C is a constant. Equivalently for angular frequency we have

$$I(\omega) \propto |\psi_0|^2\frac{1}{2\pi}\frac{1}{(\omega_0-\omega)^2+(\Gamma/2\hbar)^2} \tag{6.28}$$

Figure 6.5 show a graphical representation for such distribution. As an example excited states with mean life time τ =10^{-8} seconds will have a half-height Γ = 6.58$\times$ 10^{-8} eV. Taking in consideration the photon energy for this decay processes which are in the order of tens of keV (e.g Eu-153 isotopes has a decay with 21.54 keV) nuclei recoil energy will be significant, specially when compared to the spectral energy distribution. It is also shown in [88] that the recoil energy is approximately given by

$$E_{Recoil} = \frac{E_0^2}{2Mc^2} \tag{6.29}$$

with E_0 being the decay energy and M is the nuclear mass. This energy is in the range of 10^{-3} to 10^{-2} eV, and is 5 order of magnitude greater than the natural line width. The major implications for that occur in resonant radiation between two atoms. Supposing two atoms in a gas (free atoms) one being the emitter and the other a resonant absorbent, when emission occur the first atom will be driven back due to recoil, and emitted photon will have energy $E_1 = E_0 - E_R$.

Subsequently for the second atom to absorb this photon the recoil energy needs to be compensated, therefore the absorbing energy is $E_2 = E_0 + E_R$. Such situation is represented in the Figure 6.6. In this simplistic case there would be no absorption in the second atom since the energy gap $2R \gg \Gamma$ and there is no overlap of in emission and absorption energy distribution.

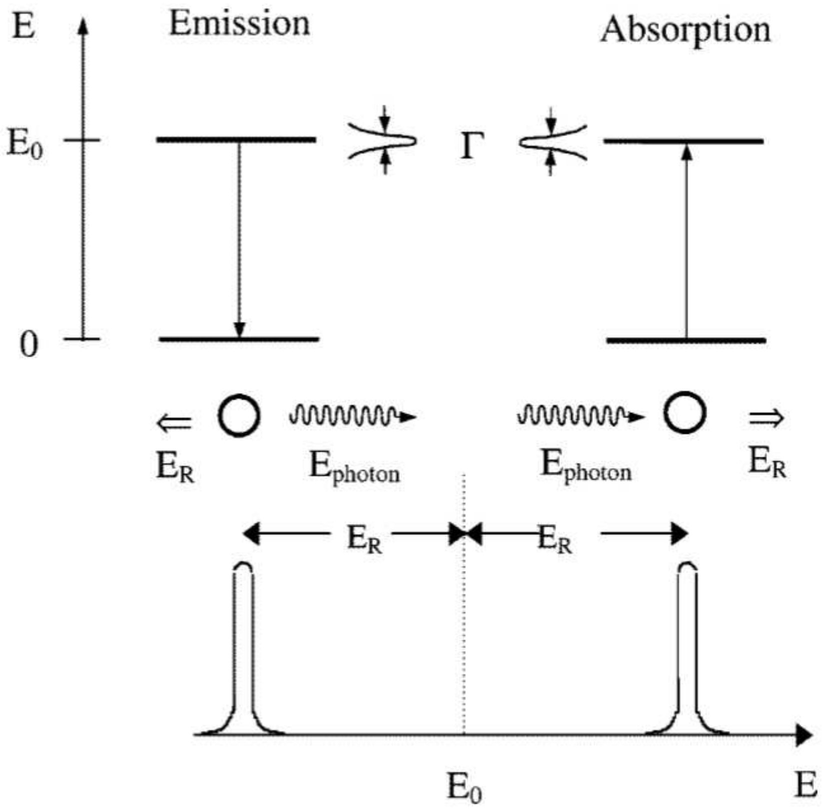

Figure 6.6: *Energies for emitted and absorbed photon in free atoms taking into account recoil energy loss. Image reproduced from [89].*

To circumvent this separation between emission and absorption lines, which prevents resonant absorption, it is possible to utilize thermal excitation or, preferably, recoiless photon emission. When thermally exciting both atoms in the previously presented picture the half height Γ will suffer the so called Doppler broadening, and there will be a overlap between emission and absorption peaks as pictured in Figure 6.7. The origin of such effect is that for moving sources there is a energy line shift:

$$\Delta E = \frac{v_r}{c} E_0 \tag{6.30}$$

where v_r is the velocity along emission direction. In a free atom (in a gas) there will be a Boltzmann distribution for such velocities ranging from $-v_r$ up to v_r, generating the broadened curve shape. The overlap generates resonant absorption, but with very dim intensities. It is important to mention that after a period of time (for which a half-life can be attributed) the excited absorbent atom will re-emit a photon of same energy in random direction, but there is also the probability for this energy to excite and eject an electron from the atom (β radiation, which we neglect here). In the context for an excited radioactive atom inside a crystalline matrix one must consider the recoil effect into the lattice, making possible recoiless emissions to occur, which is key for the Mössbauer Effect. If we assume a simple Einstein solid where we have quantified levels equally separated by energy gaps given by the Einstein energy:

$$E_E = \frac{\pi \hbar v}{a} \tag{6.31}$$

where v is the crystal sound velocity and a is the lattice parameter. Simplifying we can take into account two cases: when recoil energy is much greater than

Einstein energy $E_r \gg E_E$ or when it is much smaller $E_r \ll E_g$. For the first case, the emitting atom will be able to transition from a ground energy level E_G to a continuum well above the lowest Einstein levels, this way recoil occurs and has an effect in the entire lattice. In the second case recoil energy is not enough to promote the emitting atom up to the next upper Einstein level, leaving the atom stranded and causing recoil-less radiation emission. Of course that quantum mechanically speaking even when E_R is smaller than E_E there is still a chance for transition to occur given by [88].

$$f = e^{-E_r/E_E} \tag{6.32}$$

Another remark is that for the emitting atom to be at ground state, crystal lattice must be in low temperature compared to Einstein temperature $T \ll E_E/k$ where k is the Boltzmann constant. Lowering the temperature of the emitting source was the first major Mössbauer's contribution which made measurements with the technique bearing his name possible to be developed. In addition more accurate theoretical results are obtained using Debye's model and quantum picture for the radioactive atom embedded into the lattice and can be found in [88].

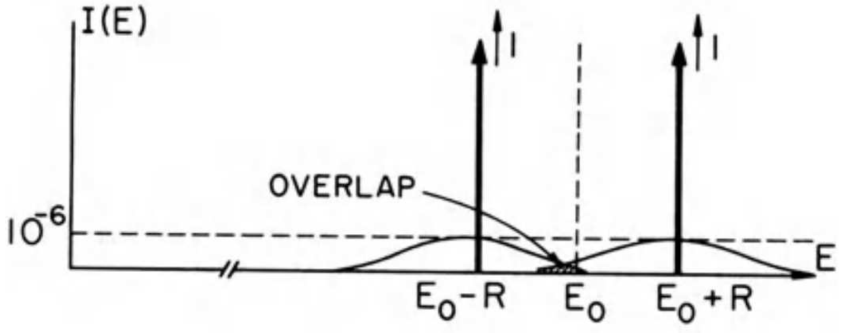

Figure 6.7: *Doppler broadening for the emission and absorption spectral lines generating a overlap at* E_0 *responsible for low intensity resonant absorption. Image reproduced from [88].*

With the simplified concepts of recoilless emission and Doppler energy shift via source velocity we have the necessary components to setup a Mössbauer technique recipe. As we saw when lowering source temperature we have a higher chance to get gamma ray emission without any losses to recoil, combining that with Doppler shift it is possible to probe the entirety of a absorption line as depicted in Figure 6.8. To shift the energy emission it is enough to translate the source with velocity v_r as described in equation 6.30, but now there won't be a broadening as saw in thermal excitation, but instead the sharp line will be displaced by ΔE, making possible to probe the absorption line width and consequently its half-life and even eventual expected energy E_0 caused by phenomena that will be explained below. Mössbauer spectra using this technique are often depicted by showing the count rate in the transmission geometry in function of the source velocity, which is proportional to the energy displacement. This makes the Mössbauer technique powerful to probe many physical and chemical material properties, with the only downside being the necessity for them to contain adequate isotopes, restraining it few element of the periodic table, with iron being the most popular one, but as we will see europium is also suitable for our interests.

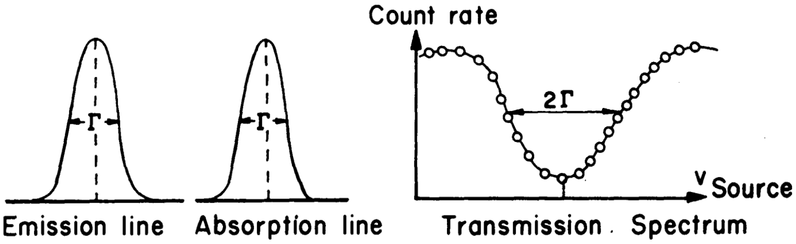

Figure 6.8: *On the left we see the emission and absorption lines for recoilles gamma ray radiation. by shifting the source with velocity v_r the emission line suffer Doppler displacement in the energy and will probe the totality of the absorption line by generating a decrease in count rate of width 2γ. Image reproduced from [88].*

The way that atomic electronic shell potentials interfere with the nucleic positive charge changes resonant Mössbauer absorption spectra, there are mainly three effects of interest that we will discuss: the isomer shift, quadrupole splitting and hyper-fine splitting (the last one being associated to magnetic fields). The first thing to note is the spatial distribution of nuclear charges, which we can approximate to be as in a uniformly charged sphere of radius R, giving electric potentials as:

$$V(r < R) = \frac{Ze^2}{R}\left(-\frac{3}{2} + \frac{r^2}{2R^2}\right) \tag{6.33}$$

and

$$V(r > R) = \frac{-Ze^2}{r} \tag{6.34}$$

In addition to that, another relevant fact is the radius difference in between excited and stable radioactive atomic nuclei [90] [91], which will generate a perturbation in energy such as [88]

$$\Delta E = \frac{2}{5} Ze^2 R^2 |\psi_s(0)|^2 \tag{6.35}$$

where $|\psi_s(0)|^2$ is the electronic density at the nucleus, mostly from s electrons, and can be considered a constant, relativistic corrections are relevant for heavy nuclei, but for simplicity we neglect it (actually this energy comes from the difference between a point charge distribution and uniformly spherical distribution). Accordingly, in an emitter-absorber pair it is possible to have two different transition energies depending on the environment in which the radioactive atom is inserted, mainly due to differences in the electronic densities. This difference in energy is known as isomer shift (IS), since it shifts the absorption peak in the intensity versus source velocity spectra, and is given by:

$$\delta = \frac{4\pi c Ze^2}{5E_0} \left(\frac{\Delta R}{R} \right) \left(\sum_A \psi^2(0) - \sum_S \psi^2(0) \right) \tag{6.36}$$

where $\Delta R = R_{ex} - R_{gnd}$ and the summation with A and S are for the electronic densities in the absorbent and source, respectively. Such parameter is relative for each source-absorbent pair, therefore isomer shifts are often reported as a relative value in respect to a well known isotope's source. This effect is useful to determine many chemical effects in the sample, being the most prominent one the differentiation between isotopes valence, which may severely changes the spatial distribution for 's' electrons, consequently changing the isomer shift value by appreciable amounts.

For nuclei with spin momenta I $>$ 1/2 the distribution of charge is not quite spherical, giving rise to a quadrupolar electric moment eQ. Associated to a field gradient along the nucleus coming from the electronic $|\psi_s(0)|$ asymmetrical charge distribution, (which can arise from chemical bounds or lattice effects for example) there will be a degeneracy lift, giving rise to (I +1/2) split levels. The energy separation from this levels can be calculated as showed in [88] [90], by setting up the Hamiltonian

$$H_Q = \frac{eQq}{4I(2I-I)}\left[3\hat{I}_Z^2 - I(I+1) + \frac{\eta}{2}(I_+^2 + I_-^2)\right] \tag{6.37}$$

where $q = V_{zz} = \delta^2 V/\delta^2 z^2$ is the gradient of the electric field along the arbitrary principal axis z, $\eta = (V_{xx} - V_{yy})/V_{zz}$ is an asymmetry parameter, I is the nuclear spin momentum and $\hat{I}$, $\hat{I}_z$, $\hat{I}_+$, $\hat{I}_-$ are spin momentum, z projection, rising and lowering operators. The difference eigenvalues for this Hamiltonian provide the energy separation for the lifted degeneracy for the general case:

$$\Delta E = \frac{eqQ}{4I(2I-1)}[3m^2 - II(I+1)](1+\eta^2/3)^{1/2} \tag{6.38}$$

Therefore, there will be several split levels from which decays can happen, (following the previously discussed dipole selection rules as well, which are also valid for nuclear decay) and these will cause several peaks to be seen in the Mössbauer absorption spectra. Depending on the energy separation and experimental resolution one may only see a broadening in the main absorption peak, but in the right conditions peaks from individual transition will be resolved. In similar fashion to what occurs with isomer shifts, Mössbauer spectroscopy is not sufficient to provide absolute values on Q, but instead it gives a ratio $Q*/Q$, between the momentum in ground state and excited state (example $Q^*_{5/2}/Q_{7/2}$). To determine absolute values it is necessary to use complementary experimental techniques such as nuclear magnetic resonance (NMR) which can measure the difference in energy for degenerate levels in manners outside the scopes of this work. Nevertheless, quadrupole splitting still valuable by itself to obtain information on symmetry of electric fields generate by a crystal lattice or how it is affected by chemical bounds.

Another factor that also lifts degeneracy in nuclear spin levels are magnetic fields, either internal or externally applied, and they give rise to the hyper-fine splitting phenomena. In similar fashion to the quadrupolar splitting it is possible to obtain each level energy by setting up a Hamiltonian [88]:

$$H_M = -g\mu_n I \cdot H \tag{6.39}$$

where g is the nuclear gyro-magnetic, μ_n is the nuclear magneton and H the magnetic field at the nucleus. This Hamiltonian will provide energy eigenvalues as

$$E_M = -g\mu_N H m_i \tag{6.40}$$

where m_i ranges from $-I$ to I in unitary complements. This is in fact a regular occurrence of the Zeeman effect but in the nuclear context. The main difference from degeneracy lift caused by quadruploar split is that now the $\pm m$ levels will be further split into m and $-m$, therefore each nuclear energy level will be split into a total of $(2|m_I + 1|)$ levels. In similar fashion as for quadrupolar splitting, NMR measurements are able to measure energies levels difference $g\mu_n H$, whereof Mössbauer transition lines can provide the ratio between gyromagnetic ratios between excited and ground state g^*/g, given that energy difference between levels i and j can be equated as:

$$\Delta E_{ij} = E_0 - g\mu_N H \left(m_j - \frac{g^*}{g} m_i^* \right) \tag{6.41}$$

where E_0 is the difference due to eventual isomer shift. As usual transitions are subjected to the dipole (or higher order depending on photon participation) transition rules as mentioned before. This effect is useful to determine if an compound has magnetic order or not, since line splitting is easily resolved experimentally, specially for high magnetic field values. Hence this is a powerful technique to combine with XMCD, since Mössbauer can distinguish between paramagnetic and ordered behavior, which is not possible using circular dichroic signal arising from electronic levels. This is of great interest for our EuB_6 since one can expect a FM to AFM transition to occur.

Appendix III

FDMNES

Finite difference method near edge structure (FDMNES) utilizes ab-initio calculation to firstly obtain electronic potentials of initial and final states of the absorbing atoms. This is done by inserting the relevant crystallographic parameters which are to solve a Poisson equation to get the Coulomb potential which is subsequently used to solve Schroedinger-like (SL) equations. These equations can be solved either using the full potentials or a muffin-tin approximation. Equation 3.4 is used to calculate the cross section, or the absorption intensity in function of energy. Additionally a convolution is performed to account the peak's Lorentzian broadening due to core hole (Gamma hole) decay and final states energy width:

$$\sigma^{conv}\left(\omega\right) = \int_{E_F}^{\infty} dE \sigma\left(E\right) \frac{1}{\pi} \frac{\Gamma_f(\omega)}{\Gamma_f\left(\omega\right)^2 + \left(\hbar\omega - E\right)^2} \tag{6.42}$$

where

$$\Gamma_f(\omega) = \Gamma_{hole} + \gamma\left(\omega\right) \tag{6.43}$$

with Γ_{hole} being a constant broadening due to core hole lifetime, and $\gamma\left(\omega\right)$ the width for final states modeled by an arc-tangent function:

$$\gamma\left(E-E_F\right)=\Gamma_{max}\times\left(\frac{1}{2}+\frac{1}{\pi}\arctan\left(\frac{\pi}{3}\frac{\Gamma_{max}}{E_l}\left(e-\frac{1}{e^2}\right)\right)\right) \tag{6.44}$$

where

$$e=\frac{E-E_f}{E_{ctr}} \tag{6.45}$$

with E_F being the Fermi Energy, Γ_{max} the total height, $E_{ctr}-E_f$ the inflection point and E_l the inclination of the arc-tangent. Finally, to simulate the experimental resolution an additional convolution utilizing a Gaussian may be performed over the Lorentzian for a better fit with obtained data. More details on these calculation and software used for the simulations can be found in [80].

For our analysis the standard arc-tangent parameters were used, being them $\Gamma_{max}=15$ eV, $E_{ctr}-E=30$ eV and $E_l=30$ eV. Additionally the Gamma hole (Γ_{hole}) and Gaussian width were adjusted through trial and error to fit experimental data on the lowest measured pressure of 2.5 GPa at 6K, with best values found to be 2.4 and 4.5 respectively. Lattice parameters used in simulations were obtained via Birch-Murnaghan equation of state 6.46: which graph was shown in Figure 6.9, the simulated pressure-lattice points coordinates are printed near the curve.

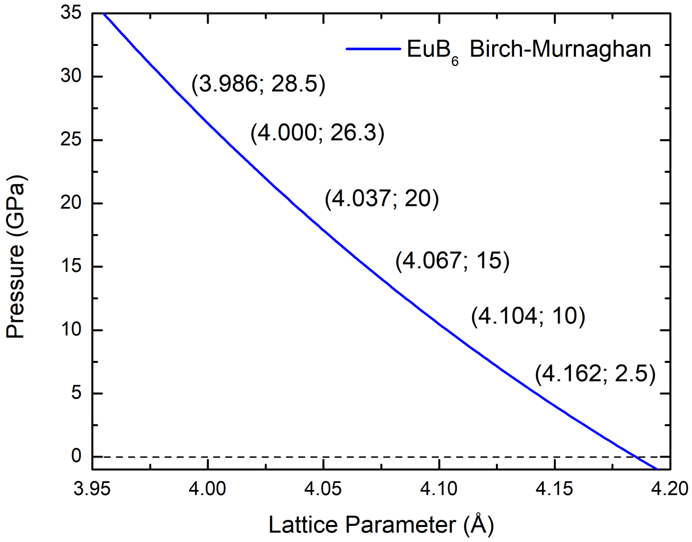

Figure 6.9: *Birch-Murnaghan equation of state 6.46 for EuB*$_6$ *in the relevant pressure span for our simulated XANES spectra. The printed coordinates pairs near the curve represent used lattice parameters in our FDMNES simulations.*

The Birch Murnagham equation of state which relates volume-pressure relationship satisfactorily for LnB$_6$ compounds:

$$P(V) = \frac{3B_o}{2}\left[\left(\frac{V_o}{V}\right)^{\frac{7}{3}} - \left(\frac{V_o}{V}\right)^{\frac{5}{3}}\right] \times \left\{1 + \frac{3}{4}(B_o^{'} - 4)\left[\left(\frac{V_o}{V}\right)^{\frac{2}{3}} - 1\right]\right\} \tag{6.46}$$

where experimental initial parameter $V_o = 4.185^3$ [11] and theoretical $B_o = 152.4$, $B_o^{'} = 3.59$ [92] where used to simulate pressure evolution in function of lattice parameter for EuB$_6$, which will be used later for computational simulations since X-Ray diffraction data for this compound in high pressures is not available in the literature. A curve for such equation can be seen in Figure 6.9 where point coordinates printed near the curve are relevant in the context of our realized experiments.